MEASUREMENTS OF COMPTON SCATTERING ON THE PROTON AT $2 - 6\ GeV$

BY

AREG DANAGOULIAN

B.S., Massachusetts Institute of Technology, 1999
M.S., University of Illinois at Urbana-Champaign, 2001

DISSERTATION

Submitted in partial fulfillment of the requirements
for the degree of Doctor of Philosophy in Physics
in the Graduate College of the
University of Illinois at Urbana-Champaign, 2006

Urbana, Illinois

MEASUREMENTS OF COMPTON SCATTERING ON THE PROTON
AT $2-6\ GeV$

Areg Danagoulian, Ph.D.
Department of Physics
University of Illinois at Urbana-Champaign, 2006
Prof. Alan Nathan, Advisor

Similar to elastic electron scattering, Compton Scattering on the proton at high momentum transfers(and high $p_\perp$) can be an effective method to study its short-distance structure. An experiment has been carried out to measure the cross sections for Real Compton Scattering (RCS) on the proton for 2.3-5.7 GeV electron beam energies and a wide distribution of large scattering angles. The 25 kinematic settings sampled a domain of $s = 5-11(GeV/c)^2$, $-t = 2-7(GeV/c)^2$ and $-u = 0.5-6.5(GeV/c)^2$. In addition, a measurement of longitudinal and transverse polarization transfer asymmetries was made at a 3.48 GeV beam energy and a scattering angle of $\theta_{cm} = 120^o$. These measurements were performed to test the existing theoretical mechanisms for this process as well as to determine RCS form factors. At the heart of the scientific motivation is the desire to understand the manner in which a nucleon interacts with external excitations at the above listed energies, by comparing and contrasting the two existing models – Leading Twist Mechanism and Soft Overlap "Handbag" Mechanism – and identify the dominant mechanism. Furthermore, the Handbag Mechanism allows one to calculate reaction observables in the framework of Generalized Parton Distributions (GPD), which have the function of bridging the wide gap between the exclusive(form factors) and inclusive(parton distribution functions) description of the proton. The experiment was conducted in Hall A of Thomas Jefferson National Accelerator Facility(Jefferson Lab). It used a polarized and unpolarized electron beam, a 6% copper

radiator with the thickness of 6.1% radiation lengths (to produce a bremsstrahlung photon beam), the Hall A liquid hydrogen target, a high resolution spectrometer with a focal plane polarimeter, and a photon hodoscope calorimeter. Results of the differential cross sections are presented, and discussed in the general context of the scientific motivation.

Table of Contents

List of Tables . . . . . **xiii**

List of Figures . . . . . **xiv**

Chapter 1 Introduction: Proton Structure and Generalized Parton Distributions **1**
1.1 The Proton 1
1.2 Exclusive Physics and Form Factors 5
1.3 Inclusive Physics and Parton Distribution Functions 9
1.4 Generalized Parton Distributions (GPD) 15

Chapter 2 Compton Scattering on Proton at Medium Energies **21**
2.1 Introduction 21
2.2 Compton Scattering on Point Particle 22
2.3 Compton Scattering on Proton: perturbative QCD 24
2.3.1 Predictions for Compton Scattering 27
2.4 Soft Overlap "Handbag" Mechanism 32
2.4.1 Compton Scattering Form Factors through Generalized Parton Distributions 34
2.4.2 Compton Scattering Polarization Transfer Asymmetry through GPD's 40
2.5 Summary 41

Chapter 3 Experimental Apparatus **43**
3.1 The Thomas Jefferson National Accelerator Facility 45
3.2 Experimental Hall A of Jefferson Lab 47
3.2.1 Beamline setup 47
3.2.2 Cryogenic Target and 6% Cu Radiator 50
3.2.3 High Resolution Spectrometer 53
3.2.4 HRS Detector Package and Vertical Drift Chambers 55
3.3 Photon Spectrometer 59
3.3.1 Electromagnetic Calorimeter 60
3.3.2 Electron "veto" Detector and Dipole Magnet 65
3.4 Hall A Focal Plane Polarimeter 68
3.4.1 Proton Polarimetry 69
3.5 Data Acquisition and RCS Trigger 71

3.5.1 Trigger Configuration . . . 72
3.5.2 Data Acquisition System . . . 75

Chapter 4 Data Analysis: Data Reduction, and Preliminary Analysis . . . 78
4.1 The General Flow of Analysis . . . 78
4.2 Proton Data . . . 80
4.2.1 HRS Vertical Drift Chambers . . . 80
4.2.2 Spectrometer's Magnetic Optics . . . 82
4.3 Photon Data . . . 88
4.3.1 Energy and Position Calibration . . . 89
4.4 Coincidence Data . . . 94
4.4.1 Event Structure and Separation . . . 94
4.4.2 Preliminary Polynomial Fitting . . . 96
4.4.3 Shortcoming of Preliminary Analysis . . . 103

Chapter 5 Monte Carlo Simulation . . . 106
5.1 Introduction . . . 106
5.2 Monte Carlo Method . . . 107
5.2.1 Rejection method . . . 107
5.2.2 Inverse Transform Method . . . 109
5.3 Monte Carlo Simulation of Experimental Apparatus . . . 110
5.3.1 General Structure . . . 112
5.3.2 Input Parameters . . . 115
5.3.3 Bremsstrahlung Calculation . . . 118
5.3.4 Cross Section and Normalization of Yield to Accumulated Charge . . . 119
5.3.5 Event Generator . . . 123
5.3.6 External Bremsstrahlung in Air and Target material . . . 125
5.3.7 Radiative Corrections at Reaction Vertex . . . 126
5.3.8 π^0 decay . . . 129
5.3.9 High Resolution Spectrometer . . . 130
5.4 Data Analysis: Elastic Electron Scattering . . . 132

Chapter 6 Data Analysis with Monte Carlo Simulations . . . 138
6.1 Production Data . . . 138
6.1.1 Kinematic point 3C: Event Separation and Extraction of Yields . . . 139
6.2 Subtraction of Virtual Compton Scattering Events . . . 153

Chapter 7 Physics Analysis and Discussion of Results . . . 162
7.1 Final Results of RCS Cross Section and Systematic Uncertainties . . . 162
7.2 Systematic Uncertainties . . . 163
7.2.1 Differential cross section comparisons . . . 169
7.2.2 s-dependence of $d\sigma/d\sigma_{KN}$ ratio, and vector form factor R_V . . . 173
7.2.3 $s^{-n(\theta_{cm})}$ scaling in $d\sigma_{rcs}/dt$ . . . 178
7.3 Conclusions . . . 182

7.3.1 Leading Twist Mechanism 182
7.3.2 Soft Overlap Handbag Mechanism 188
7.3.3 Overall Conclusions 192
7.4 Future Plans 193
7.4.1 Theoretical Improvements for Soft Overlap Mechanism 193
7.4.2 12 GeV upgrade at Jefferson Laboratory 194
7.4.3 RCS-II 194

Appendix A Mandelstam variables 196

References 198

Author's Biography 203

List of Tables

3.1 Performance characteristics of Hall A's left HRS. 54
3.2 Electromagnetic and optic characteristics of TF-1 lead glass. 62

5.1 Ratio of observed and measured (e,p) cross sections 137

6.1 Table of numerical values used in the analysis process. The primed variables are those produced by the simulation for an accumulated beam charge of $1mC$. 150
6.2 The proportion of Virtual Compton Scattering events, VCS/(VCS+RCS), calculated using Monte Carlo simulations, for different kinematic points. . . 158
6.3 Final results of Real Compton Scattering differential cross sections, corrected for VCS contributions (as presented in Table 6.2). 159
6.4 Kinematic values of the calorimeter and spectrometer settings 160

7.1 Table of final cross section results. 164
7.2 Final results for vector form factor $R_V(t)$, determined using Scenarios one, two and three for target mass corrections. Number two has been considered to be the preferred scenario. 177

List of Figures

1.1 First order Feynman diagrams for elastic electron-proton scattering (a) and Deep Inelastic Scattering (b). 7
1.2 Plot of $\mathcal{F}_2(x_B)$ vs. Q^2 for different values of $x_B = Q^2/2m\nu$. Data is from [1] 12
1.3 Plots of $\mathcal{F}_1(x) = 2mW_1(x)$ vs. $\omega \equiv 1/x$ and $\mathcal{F}_2(x) = \nu W_2(x)$ vs. $\omega \equiv 1/x$ for different values of $x_B = Q^2/2m\nu$. Data is from one of the original experiments which took place at Stanford Linear Accelerator [2] 14
1.4 Feynman diagram for Real Compton Scattering (RCS) on a nucleon. A simple example of a model for Generalized Parton Distribution $F(x,t)$ can be found in Ref. [3] 16
1.5 Feynman diagram for the analogous elastic electron scattering on a nucleon. 16
1.6 Impact parameter $\mathbf{b}_\perp = (b_x, b_y)$ distributions in the transverse $x-y$ plane for a proton, for different values of active quark's fractional momentum x [4]. . 19
1.7 Distribution of impact parameter amplitude $b_\perp$ and fractional momentum x. [5]. 19

2.1 Leading Feynman Diagram for Leading Twist Mechanism. x_i stand for the fractional momentum of the quarks. The diagram enclosed by the doted box corresponds to T_{hard} from Eq. 2.4, and its amplitude can be determined using calculations based on pQCD. 26
2.2 Plots of data from Ref. [6], and pQCD predictions using different DA's: CZ [7] (dashed), KS [8](full),COZ [9](point-dashed), and asymptotic (doted). . . . 30
2.3 Plots of Skewed DA's: KS(top) [8] and COZ(bottom) [9]. 30
2.4 Leading order Feynman diagrams for Real Compton Scattering in the framework of Soft Overlap "Handbag" Mechanism. 32
2.5 Two-body contribution to RCS form factor. 36
2.6 Two-body contribution to elastic form factor. 36
2.7 Currently available predictions for polarization transfer asymmetry K_{LL}: Leading Twist (green), Soft Overlap Handbag (blue), LFCBM and Regge exchange. 39

3.1 Experimental Setup of Hall A for E99-114 experiment 44
3.2 Schematic view of CEBAF. The electron beam is produced in the injector, after which it is accelerated in each of the two superconducting linacs. The beam can be circulated up to five times, resulting in an energy of apprx. $5.75GeV$ 46

3.3 Schematic layout of Hall A beam setup and relative positioning of the two High Resolution Spectrometers. 49
3.4 Bremsstrahlung spectrum (red) and corresponding electron spectrum(blue) for a radiator of thickness of 6.84% radiation lengths. The shaded region corresponds to the part of the spectrum observed by the experimental acceptance. 52
3.5 Schematic drawing of Hall A High Resolution Spectrometer's magnetic structure. 55
3.6 Schematic layout of Hall A beam setup and relative positioning of the two High Resolution Spectrometers. 57
3.7 The Vertical Drift Chambers of High Resolution Spectrometer, and their relative positioning. 58
3.8 Feynman diagrams for a) Electron Bremsstrahlung b) pair production. During an electromagnetic shower the radiated photon of (a) becomes the pair-producing photon of (b). 60
3.9 Drawing of RCS electromagnetic calorimeter, showing its internal structure. 63
3.10 A numerical calculation of the component of the magnetic field perpendicular to particle's trajectory as a function of lateral(x_{magnet}, the abscissa) and longitudinal(z_{magnet}, the ordinate) coordinates. x_{magnet} is increasing toward decreasing scattering angles. 66
3.11 A plot of $\int \mathbf{B} \cdot \mathbf{dl}$ versus scattering angle. The two sets of data, as fitted with two different lines, correspond to the current settings of 600 A (red line) and 500 A (blue line) 68
3.12 The dual analyzer configuration of Hall A Focal Plane Polarimeter (FPP). . 69
3.13 The photon trigger consists of the OR of the overlapping sum_{32} arrays, a configuration which makes sure that a given electromagnetic shower is entirely contained by at least one summing unit. 73
3.14 The drawing of electronic setup for the RCS trigger logic. 76

4.1 Left: Sieve-slit collimator pattern. Right: plot of event coordinates as projected on the sieve slit plane, clearly showing the position of the holes (compare with the picture on the left). The intersection of the lines correspond to the actual measured position of the holes. 86
4.2 Left: the nine foils of the carbon target. Right: vertex position plotted against scattering angle. The lack of any correlation points to a good calibration and a stable optic transformation tensor. In both plots the lines correspond to the measured target foil positions. 89
4.3 Top: plots of calorimeter energy E and $(E - E(p))/E(p))$, where $E(p)$is the expected energy, calculated from proton kinematics. The second plot is fitted, showing a calorimeter resolution of 5.4%. Bottom: Reconstructed calorimeter hit position coordinates. From Ref. [10]. 92
4.4 In plane (left) and co-planarity(right) correlations, calculated by subtracting measured calorimeter position from the predicted position as calculated from proton's kinematic variables. The Gaussian fits reveal the combined vertical and horizontal coordinate resolution of the experiment: 4.8 cm and 4.5 cm at the distance of 1200 cm. 92

4.5 Calibration Coefficients C_i for every block of the calorimeter. From Ref. [10]. 93
4.6 Left: time difference("coincidence time") between the hits in the two arms for coincidence events. Right: coincidence time vs. calorimeter energy for the events which registered coincidence hits between the two arms. The doted square denotes the cut used for data analysis.Both plots are done for kinematic point 5A. 97
4.7 A schematic illustration of data and background structures. 105
4.8 Top: plots of δy and δx, revealing RCS peak at $\delta y \approx \delta x \approx 0$, the electron peak at $\delta x \approx -40\ cm$ and the π^0 decay background continuum underneath the peaks. The fit consists of a combination of two Gaussian functions (to account for RCS and ep events) and a polynomial functions to account for pion background.
Bottom: calorimeter energy distribution, fitted using a combination of a Gaussian and a $1/E$ function which has been "smeared" by calorimeter resolution. 105

5.1 Left: Illustration of the rejection method – random point are sampled in the bounding box, and rejected if the ordinate is larger than $f(x)$. Right: Inverse Transform Method for continuous (a) and discrete (b) distributions 108
5.2 The structure of RCS Monte Carlo Simulation. The shaded region corresponds to the Monte Carlo loop itself. 116
5.3 The Feynman diagram for external bremsstrahlung. 126
5.4 The Feynman diagram for internal bremsstrahlung. 127
5.5 The angular distributions of radiated photons, for different values of Q^2. The abscissa is the cosine of the angle between photon's and emitting electron's direction 127
5.6 The momentum vs. angle distribution for the data set from acceptance scan runs. 134
5.7 Comparison of data and Monte Carlo for run 1635. Monte Carlo corresponds to red circles, data corresponds to blue circles. 134
5.8 $2a$ **scans, momentum(from top to bottom)** $-$ $1.788 Gev/c$**,** $1.762 Gev/c$**,** $1.711 Gev/c$**,** $1.661 Gev/c$**,** $1.637 Gev/c$**.** 135

6.1 Uncorrected (left) and corrected (right) coincidence time distributions,after extensive cuts on calorimeter energy and other kinematic variables. The red lines denote the timing cut used in the analysis. 139
6.2 Left: δx distribution with $\mathbf{abs}(\delta \mathbf{y} - \mathbf{3.}) < \mathbf{15}$. Right: same, with $\mathbf{abs}(\delta \mathbf{y} - \mathbf{3.}) > \mathbf{15}$, showing the pion distribution. 140
6.3 a) general event distribution. Blue circle marks the electron distribution, and red circle marks the RCS event distribution. b) events extracted as a result of the cuts used in Eq. 6.2, and later used for determining the pion background normalization 143
6.4 Events from Fig. 6.3(b) projected on δx and δy axes. Simulation is denoted by red line, while the blue circles represent data. 143

6.5 In all following plots the simulation is denoted by a red line: a) The energy of π^0 decay photon, as calculated from proton's kinematics and photon calorimeter coordinate, using Eq. 5.24; b) The energy of π^0 decay photon, as measured in the calorimeter; c) the difference of the previous two quantities. 144
6.6 Left: δy distribution with $\mathbf{abs}(\delta\mathbf{x} - \mathbf{2}.) < \mathbf{8}$. 145
6.7 Energy dependences of neutral pion photoproduction for 3C(left) and 5E(left) kinematic points. Blue circles denote the data, full lines denote simulation with a non-constant cross section, and doted lines denote simulation with a constant cross section. 147
6.8 E_{calo} distribution with $\mathbf{abs}(\delta\mathbf{x} - \mathbf{2}.) < \mathbf{8}$. The punctured line denotes the cut used to isolate the $ep\gamma$ background. 148
6.9 Dependence of absolute cross section on calorimeter cuts. The ordinate is presented as the ratio of cross section to a constant cross section supplied to the Monte Carlo simulation. The line and the gray error band represent our final result. 151
6.10 a) Electron data count distribution, with π^0 background subtracted. Red line is the simulation. b) A full data to simulation comparison, with a simulation of electron background added to the other event types. 152
6.11 Calorimeter energy distribution. Red lines correspond to simulation with two assumptions: pointed line – that background drops linearly; full line – that background follows the simulated shape of bremsstrahlung radiation. The difference between the resulting cross sections is 7% 154
6.12 Virtual Compton Scattering(VCS). Due to very low virtuality ($-q^2 < 0.01 GeV^2$) of the incoming photon, the part of the diagram enclosed in the blue square is essentially identical to Real Compton Scattering(RCS), in terms of amplitude and kinematic dependences. The only difference between this process and RCS is the incoming photon(γ^*) flux. 155
6.13 Top: δx distributions for RCS (blue) and VCS(red) events. Bottom: Q^2 distribution for virtual photons. The full circles correspond to data with cuts on δx and δy. The open circles are for the data with no cuts. 161

7.1 The ratio of the results as determined by Polynomial Fitting method and Monte Carlo method. 165
7.2 RCS cross section $d\sigma/dt$ in units of nB/GeV^2. Solid points represent data from this experiment (E99-114), while open points marks correspond to previous data [6]. The lines with error bands correspond to calculations of RCS form factors using GPD formalism, see Ref. [11] [12] 171
7.3 Same results as in Fig. 7.2, however with the condition of $-u > 2.5 GeV^2$ . . 172
7.4 RCS vector form factor $R_V(t)$ determined by utilizing different scenarios for target mass corrections. The data points correspond to kinematic settings where $-u, > 2.4\ GeV^2$. The theoretical line correspond to calculations of $R_V(t)$ based on GPD formalism, see Ref. [11] 175

7.5 Fits to the cross section for given values of θ_{cm}. On log-log scale the fitting function reduces to a simple linear fit of the following form: $\log(d\sigma/dt) = c + n \cdot \log s$ 179
7.6 Extraction of exponent n from the data for the Constituent Quark Counting Rule prediction of $d\sigma/dt = f(\theta_{CM})/s^n$. Red data points correspond to this experiment(E99-114), blue squares correspond to previously available data [6]. The red curve is determined based on Soft Overlap Handbag Mechanism. 180
7.7 Leading Feynman Diagram for Leading Twist Mechanism. x_i stand for the fractional momentum of the quarks. The diagram enclosed by the doted box corresponds to T_{hard} from Eq. 2.4, and its amplitude can be determined using calculations based on pQCD. 183
7.8 Polarization Transfer Asymmetry results for Real Compton Scattering on proton, revealing close agreement of the experimental results (from E99-114 col.) with the Soft Overlap "Handbag" prediction (marked as "GDP"). The experimental result is from Ref. [13]. The curves marked as "COZ" and "ASY" correspond to Leading Twist calculations, based on humped and non-humped DA's, respectively. The curve marked as "KN" corresponds to Compton scattering on a structureless and massless proton. 187
7.9 Leading order Feynman diagrams for Real Compton Scattering in the framework of Soft Overlap "Handbag" Mechanism. 188

A.1 Scattering diagram, with incoming and outcoming particle four-momentums p,k,p' and k' 197

Chapter 1

Introduction: Proton Structure and Generalized Parton Distributions

1.1 The Proton

The first evidence of the existence of an elementary (as it was thought of at the time) particle with the characteristics of proton came as early as in 1918, when Ernest Rutherford, while studying the effect of alpha particles on nitrogen gas, noticed features in the data which are characteristic to hydrogen nuclei. Rutherford then concluded that the nitrogen nucleus must consist of hydrogen nuclei, and hence suggested that the hydrogen nucleus, which was known to be the element with the lowest atomic weight, is an elementary particle, and named it the proton. For some period of time the proton was indeed believed to be an elementary structure-less particle, or in terms of Quantum Electrodynamics, a Dirac particle. The invalidity of this belief became clear in 1933, when Otto Stern determined proton's

gyromagnetic ratio's g-factor by measuring the magnetic moment, and found it to be $g_p = 5.59$ instead of $g_{Dirak} \approx 2$ as expected for a truly structureless particle. This circumstance ignited a major interest in the proton, and spurred global attempts to understand proton's internal structure.

The first experiments used elastic electron scattering – in an analogy to Rutherford's elastic alpha-particle scattering experiments on gold atoms – to glean an insight on the proton. In analogy with the classical example, where the observables of scattering on an extended charge-current distribution can be expressed as a product of the "point" observable and the Fourier transforms of charge and current distributions, the cross section of elastic electron distribution was expressed as a product of Mott cross section for scattering on point proton, and a combination of electric and magnetic form factors:

$$\frac{d\sigma}{d\Omega} = \frac{d\sigma_{Mott}}{d\Omega} \left[\frac{G_E^2 + \frac{Q^2}{4M^2} G_M^2}{1 + \frac{Q^2}{4M^2}} + 2\frac{Q^2}{4M^2} G_M^2 \tan^2 \theta/2 \right] \tag{1.1}$$

where $-Q^2$ is the four-momentum transfer squared, while G_M and G_E are the magnetic and electric form factors. This separation of the scattering cross section into electric and magnetic parts was performed by Marshall Rosenbluth, and nowadays is referred to as "Rosenbluth formula" [14].

Later on in the history of nuclear physics, in the sixties, Murray Gell-Mann proposed a model of proton, consisting of three partons – truly point-like structure-less particles, which are confined in the proton by the strong interaction. The strong interaction is also referred to as the color force, and is mediated by the exchange of particles known as gluons. The quantum theory describing these processes is called Quantum Chromodynamics (QCD), and is constructed in a direct analogy to Quantum Electrodynamics (QED). Once

the model was proposed, it was immediately inferred that a strong enough excitation could break the proton into its constituent parts. This gave rise to a series of Deeply Inelastic Scattering(DIS) experiments. The results of the early DIS experiments from Stanford Linear Accelerator (SLAC) seemed to indicate that when scattered on the proton, the electron experiences scattering on multiple discrete scattering centers, as if the proton consisted of smaller particles. Specifically, it was found that at fixed Bjorken x_B the ratio of observed cross section and the cross section of scattering on a point particle (as calculated in QED) – $\sigma_{DIS}/\sigma_{point}$ – is almost independent of the four-momentum transfer q, as would be the case for a truly point-like particle. Furthermore, with increasing beam energies and momentum transfers this dependence becomes even weaker. Based on these findings, it was concluded that the proton consists of point-like particles – partons – and as the energies increase the scattering occurs on these partons rather than on the proton itself [15]. The logic behind the experimental technique is remarkably similar to that of the early Rutherford experiments, albeit at a much higher energy scale.

After the discovery of a nucleon's parton structure, a flurry of activity followed in nuclear physics, both in experiment and in theory . A number of DIS experiments investigated the spin structure of the proton, and discovered that the quark spin doesn't entirely account for the proton's magnetic moment. Meanwhile, the theorists tried to address the issue of quark confinement as well as that of applicability of perturbation theory to QCD. The complexity of the problem consist of the fact that unlike the electromagnetic interactions, the color force increases with increasing distances. This means that as the energy transfers decrease the probe "sees" interactions at larger distances, with a stronger potential. As the potential

of the interaction increases, it becomes impossible to treat it as a mere perturbation to the total energy of the ensemble. It has been however very unclear as to at which values of s, t and u Mandelstam variables(see Appendix A for the definition) does perturbative QCD (pQCD) become applicable. An extensive calculation by S. Brodsky and G. Farrar [16] performed in the perturbative framework resulted in the so called Constituent Quark Counting Rule, which predicted that for the exclusive processes the applicability of pQCD would entail scattering cross section's s-dependence of the following form:

$$\frac{d\sigma}{dt} = f(\theta_{cm})\ s^{2-n}$$

where n is the total number of photon, lepton and quark elementary field constituents in the initial and final states of the diagram. This is one of the most mathematically rigorous results of perturbative QCD, and can be experimentally tested with high accuracy. Indeed, results from an experiment in late 1970's, which measured Compton scattering on proton at medium energies, did observe what at the time seemed to be a $1/s^6$ dependence in cross section. It was however puzzling to find out that experimental results showed values of $f(\theta_{cm})$ which were almost two orders of magnitude larger than the theoretical predictions. Furthermore, it quickly became clear that a number of nonperturbative phenomenological models would also predict $1/s^n$ dependences which would agree with the data, at least within experimental uncertainties.

This gave rise to doubts about the original assertion on pQCD's applicability at medium energies. A number of theoretical papers [17], influenced by experimental results which deviated strongly from perturbative calculations, asserted that pQCD can be applied only at much higher energies and momentum transfers. This became a reason for a search of a

mechanism which would treat the quark-quark interactions in a non-perturbative framework. After a long period of standstill, in 1997 a new mechanism of real Compton scattering was proposed by X. Ji [18], which argued that the gluon exchanges in the leading twist pQCD diagram could not be treated perturbatively but needed to be included in the part of the diagram which accounted for the low-momentum "soft" interactions. This gave rise to the so called Soft Overlap Mechanism, where only one quark absorbs and re-emits the photon, while the rest remain as spectators. Due to a lesser number of hard vertexes, this diagram resulted in a much larger amplitude. Subsequent efforts by A. Radyushkin, M. Diehl, P. Kroll and others [3] [19] [20] yielded values for cross section comparable to those provided by the existing data. The new approach was also made original by the use of Generalized Parton Distribution (GPD) formalism, which in essence is a combination of the ideas behind Form Factors, extracted from exclusive measurements, and parton distribution functions, as measured by inclusive measurements.

1.2 Exclusive Physics and Form Factors

Since the advent of nuclear physics electron scattering has been one of the most effective methods to study the internal structure of nuclei and nucleons. Elastic electron scattering on a proton is a good example of exploitation of electromagnetic probes to study proton's electric and magnetic structure. Here the term elastic implies conservation of total kinetic energy, and no change in the internal energy of the particles. Meanwhile, the *exclusive* nature of the experiment comes from the circumstance that the kinematic quantities for all the incoming and outgoing particles are known. The electron couples electromagneticaly to the charge

and current distributions inside the proton. Since the carriers of those distributions are the quarks themselves, elastic electron scattering can be a very effective method to study the internal partonic structure of the nucleon. Elastic scattering of electron on a point charge-current distribution is very well understood in the framework of QED and can be precisely calculated. Any deviations of the experimental observables from calculations based on point-like structure will immediately point to and reveal the complex structure of the proton. Very similar to X-ray crystallography, where scattering cross section can be expressed to be proportional to the Fourier transform of lattice structure, the cross section of elastic electron scattering can be expressed into a product of point-like "Mott" cross section and a combination of electric and magnetic form factors, as seen earlier in Eq. 1.1. Furthermore, in this formalism the proton only "sees" the virtual photon which it exchanges with the electron. Hence the resolution of this kind of probe can only depend on the wavelength of the photon and correspondingly on the four-momentum transfer. The Feynman diagram for elastic electron scattering can be seen in Fig. 1.1 (a).

The description of elastic electron scattering on an extended charge and current distribution is based on a number of fundamental assumptions:

- To describe the nucleon's deviations from point-like behavior so called form factors are introduced, which are included in the scattering amplitude as vector and tensor transition current matrix elements between nucleon states.

- The form factors have to include at least two independent terms, to separately describe proton's electric and magnetic structure.

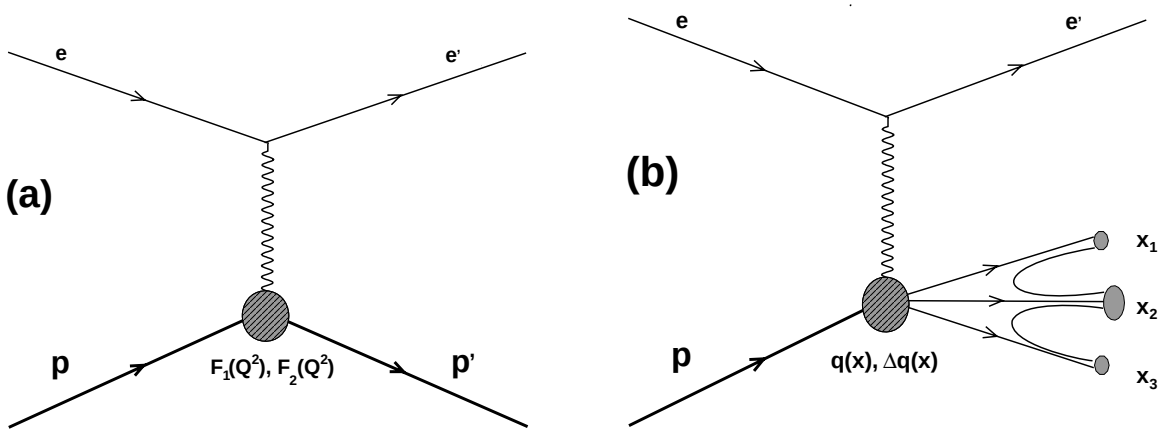

Figure 1.1: First order Feynman diagrams for elastic electron-proton scattering (a) and Deep Inelastic Scattering (b).

- Since the spacial resolution of a probe is directly related to its wavelength, which, in its turn is related to the momentum transfer, the form factors need to depend only on the momentum transfer to the nucleon.

At lower energies, when the wavelength of the exchanged virtual photon is larger than the size of the nucleon, the later is essentially seen as a point particle, and the scattering amplitude is described by so called Mott cross section:

$$\left[\frac{d\sigma}{d\Omega}\right]_{Mott} = \alpha^2 \frac{E'}{4E^3} \frac{\cos^2\theta/2}{\sin^4\theta/2} \tag{1.2}$$

where α is the fine splitting constant, θ is electron scattering angle, and E and E' are electron's incoming and outgoing energies.

However, as the energy of the incoming electron increases, the wavelength of the virtual photon decreases and it becomes sensitive to the internal structure of the proton, that is, it sees only small portion of the charge-current distribution. This causes a strong drop in the cross section from its Mott value. This drop in cross section is conditioned by the proton's

extended current-charge distribution, and the new cross section has the following form:

$$\frac{d\sigma}{d\Omega} = \left[\frac{d\sigma}{d\Omega}\right]_{Mott} \left\{F_1^2(Q^2) + \tau[F_2^2(Q^2) + 2(F_1(Q^2) + F_2(Q^2))^2 \tan^2\theta/2]\right\} \tag{1.3}$$

where

$$\tau = \frac{Q^2}{4M^2} \quad \text{, and} \quad Q^2 = 4EE' \sin^2\theta/2$$

$-Q^2$ here is the squared four momentum transfer to the proton, and corresponds to the invariant mass of the virtual photon. $F_1(Q^2)$ and $F_2(Q^2)$ are the Dirac and Pauli form factors, corresponding to transitions between nucleon states. The physical meaning of these form factors becomes more understandable when we combine them linearly into so called electric and magnetic form factors:

$$\begin{aligned} G_E(Q^2) &\equiv F_1(Q^2) - \tau F_2(Q^2) \\ G_M(Q^2) &\equiv F_1(Q^2) + F_2(Q^2) \end{aligned} \tag{1.4}$$

In the center-of-mass frame of the reaction, and in non-relativistic low energy regime, these can be related to the Fourier transforms of charge and current distributions. The strong dependence of the nucleon form factors on Q^2 at medium energies is a direct indication of the proton's extended shape. By fitting to elastic data, the form factors have been found to be[1]

$$G_E(Q^2) \approx (1 + \frac{Q^2}{0.71\text{GeV}^2})^{-2} \quad \text{and} \quad G_M(Q^2) \approx 2.75 \cdot G_E(Q^2) \tag{1.5}$$

Besides allowing for one to determine the electron scattering cross sections, the form factors can be directly used to provide detailed information about the proton. For example, for

[1]It should be noted that this relation is no longer believed to be exact. Recent experiments have shown that the G_E/G_M ratio decreases with increasing Q^2 [21–23]. For the sole purpose of determining the cross section, however, this is still a valid expression.

small values of Q^2 the mean square radius of the proton can be found to be [24]

$$< r^2 >= 6 \left(\frac{dG_E(Q^2)}{dQ^2} \right)_{Q^2 \to 0} = (0.81 fm)^2 \tag{1.6}$$

Furthermore, using Fourier analysis, we can show that in order for a form factor to have the form of Eq. 1.5, the charge distribution needs to have a form of

$$\rho(r) \propto e^{-r/r_0}$$

1.3 Inclusive Physics and Parton Distribution Functions

Having observed the proton at lower momentum transfers, where the interaction is sensitive to the proton's internal structure only as a strongly-interacting ensemble, it becomes interesting to decrease the wavelength of the exchanged photon, in order to attempt to resolve individual constituents, or as we call them now – partons. There is however a crucial difference: as the energy transfer increases, with some probability the proton starts to break up into its constituents, since the energy binding those is smaller than the energy absorbed by the proton. The scattering is not elastic anymore, and the process is described as Deeply Inelastic Scattering (DIS). The diagram of Fig. 1.1(a) has to be replaced with that of Fig. 1.1(b). In this case, unlike exclusive measurements, the kinematic knowledge of the electron vertex is not enough to predefine the kinematic quantities in the final state. The experiment only observes the scattered electron, hence all possible outcomes of the final state are summed over, which is what makes this an *inclusive* measurement. Due to this lack

of information, the elastic form factors cannot anymore describe the process, and new, more generalized *structure functions* need to be introduced in analogy with the form factors. The main difference is that the structure functions need to depend both on Q^2 and ν, the energy transfer to the proton. In analogy to Eq. 1.1 we write

$$\frac{d\sigma_{DIS}}{d\Omega} = \frac{d\sigma_{Mott}}{d\Omega}\left\{W_2(Q^2,\nu) + 2W_1(Q^2,\nu)\tan^2\theta/2\right\} \tag{1.7}$$

where the Mott point cross section is defined in Eq. 1.2.

The expression of Eq. 1.7 provides a generic mathematical framework for describing DIS. It however doesn't provide any explicit clues about the internal structure of the nucleon and only allows us to denote our ignorance of proton's structure. However, if we assume that the proton in fact constitutes an ensemble of quarks(partons), then we can at least use this picture of proton structure to model W_2 and W_1.

Let's assume that the proton is made of spin-$\frac{1}{2}$ point-like partons. Then, for a very large Q^2 the scattering should occur on these particles. If this is then the case, we should be able to develop a quantitative model for the structure functions based on the analogy between point cross section and DIS cross section:

$$\left[\frac{d\sigma}{d\Omega}\right]_{Mott} = \alpha^2\frac{E'}{4E^3}\frac{\cos^2\theta/2}{\sin^4\theta/2}\quad\left[\delta(\nu - \frac{Q^2}{2m}) + \frac{Q^2}{2m^2}\delta(\nu - \frac{Q^2}{2m})\tan^2\theta/2\right]$$

$$\left[\frac{d\sigma}{d\Omega}\right]_{DIS} = \alpha^2\frac{E'}{4E^3}\frac{\cos^2\theta/2}{\sin^4\theta/2}\quad\left[W_2(Q^2,\nu) + 2W_1(Q^2,\nu)\tan^2\theta/2\right]$$

Notice that unlike Eq. 1.2, here we used the full form of point cross section, with the delta function introduced to ascertain that the energy-momentum conservation $\nu = Q^2/2m$ is upheld at the electron vertex. Based on this comparison one can conclude that for an

individual parton the DIS structure functions are

$$2W_1^{point}(Q^2,\nu) = \frac{Q^2}{2m^2}\delta(\nu - \frac{Q^2}{2m})$$
$$W_2^{point}(Q^2,\nu) = \delta(\nu - \frac{Q^2}{2m})$$

Simplifying the delta functions, and replacing $\mathcal{F}_1 \equiv mW_1$ and $\mathcal{F}_2 \equiv \nu W_2$ we receive

$$2\mathcal{F}_1 = \frac{Q^2}{2m\nu}\delta(1 - \frac{Q^2}{2m\nu}) \quad \Rightarrow \quad 2\mathcal{F}_1(x_B) = x_B\delta(1-x_B)$$
$$\mathcal{F}_2 = \delta(1 - \frac{Q^2}{2m\nu}) \quad \Rightarrow \quad \mathcal{F}_2(x_B) = \delta(1-x_B)$$

where we substituted $x_B = Q^2/2m\nu$. This is a very important result: it implies that *if* the proton is in fact made of weakly interacting point particles, then at high values of Q^2 and at a fixed value of x_B the cross section starts following the shape of point cross section, and the structure functions depend *only* on x_B and not on Q^2 and ν. First time this conjecture was tested at Stanford Linear Accelerator (SLAC) in 1971, when DIS data was used to determine the Q^2 dependence of $\mathcal{F}_2 = \nu W_2$. Plots of $\mathcal{F}_2(x_B)$ vs. Q^2 for different values of x_B can be seen in Fig. 1.2, showing an almost total independence of Q^2, and hence validating the assumption that the proton consists of point-like particles.

If a parton carries x-th of the total longitudinal momentum of the proton, i.e. if it has a momentum of xp_L, then it can be shown that the structure functions for that parton should be

$$\mathcal{F}_1(x_B) = \frac{x_B}{2x^2}\delta(1 - \frac{x_B}{x})$$
$$\mathcal{F}_2(x_B) = \delta(1 - \frac{x_B}{x})$$

However, the probability that the i-th parton carries a momentum fraction x is limited. Here we have to introduce the *Parton Distribution Functions*(PDF), which are the differential

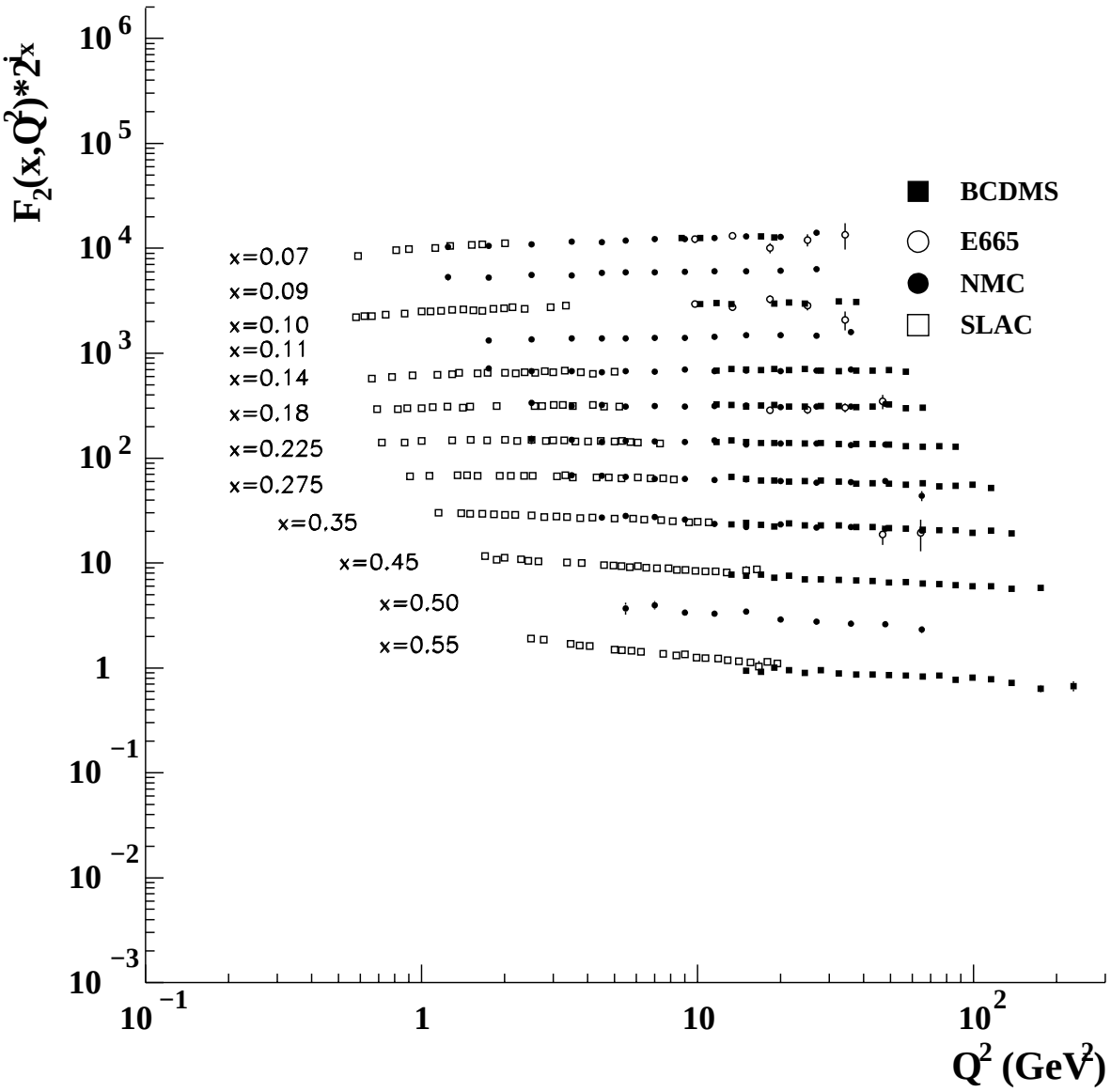

Figure 1.2: Plot of $\mathcal{F}_2(x_B)$ vs. Q^2 for different values of $x_B = Q^2/2m\nu$. Data is from [1]

probabilities of a given parton carrying a momentum xp_L. Summing our results over the partons, and including the probability that that parton carries a momentum x, we get the following expressions for the structure functions:

$$\mathcal{F}_2(x_B) = \sum_i \int_0^1 dx e_i^2 f_i(x) x \delta(x - x_B) \tag{1.8}$$

$$\Rightarrow \quad x = x_B = Q^2/2m\nu \quad \text{and} \quad \mathcal{F}_2(x) = x \sum_i e_i^2 f_i(x)$$

$$\mathcal{F}_1(x) = \frac{1}{2x}\mathcal{F}_2(x) \tag{1.9}$$

The $x = x_B$ relation is a remarkable result: it allows one to use known experimental kinematic settings (such as four-momentum and energy transfer to the target) to determine the momentum of an individual active parton. This in its turn allows one to map the dependence of structure functions on quark's fractional momentum x. Experimental measurements of $\mathcal{F}_1$ and $\mathcal{F}_2$ can be seen in Fig. 1.3. The next step, after measuring the structure functions is to try and decompose them into their PDF components, by using an experimental semi-inclusive technique called flavor tagging (to determine the flavor of the hadronized quark) to separate the statistic events by the flavor of the active parton.

It is important to note here, that the simplistic linear sum over all the partons in Eq. 1.9 implies that we neglect all parton-parton interactions. When we wrote the simple sum we essentially ignored all the couplings between the quarks. This is an approximation which is somewhat analogous to the so called *impulse approximation* in nuclear scattering, and assumes that if the energies are high enough then the relativistic time dilation in the rest frame slows down the rate at which the partons interact with each other to the point where the external coupling has a characteristic time scale which is much smaller then the time

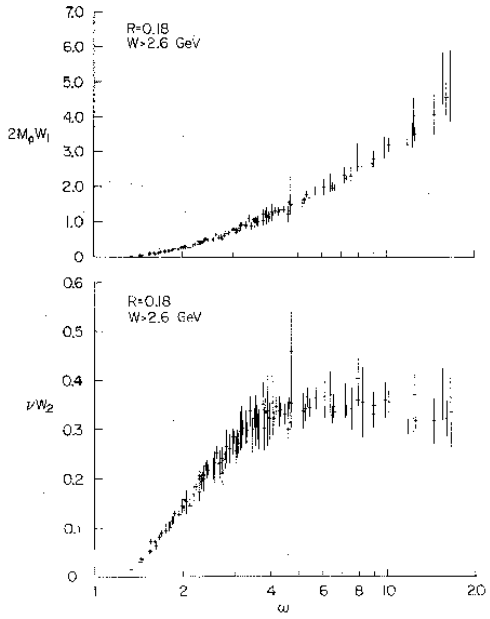

Figure 1.3: Plots of $\mathcal{F}_1(x) = 2mW_1(x)$ vs. $\omega \equiv 1/x$ and $\mathcal{F}_2(x) = \nu W_2(x)$ vs. $\omega \equiv 1/x$ for different values of $x_B = Q^2/2m\nu$. Data is from one of the original experiments which took place at Stanford Linear Accelerator [2]

scale of parton-parton interaction. The parton in this case is essentially a free particle. Another way to see is the following: as the Q^2 increases, the wavelength of the virtual photon decreases, and the photon "sees" only very short distance interactions. At short distances the color force is almost non-existent, allowing the particles to behave as if free.

Above we used the analogy with impulse approximation. There is however a major difference. After the struck nucleon escapes the potential of the nucleus, it can exist as a completely free particle. The quark however is subjected to color confinement: it has to interact with the spectator partons to form a colorless hadron which then becomes one of the fragments of the original proton. Due to the size of the proton this process of hadronization requires a time scale which is much larger (again, assuming $Q^2 \gg m^2$) than the time scale at which the quark is hit by the virtual photon. As a result, we can argue that for large values of Q^2 the interaction with the parton happens as if it were free, and that any final state interactions responsible for hadronization do not affect the calculated cross section.

1.4 Generalized Parton Distributions (GPD)

Deep Inelastic Scattering and Elastic Electron Scattering are the two very different methods of investigating the nucleonic structure, and deal with two different phases of the proton. These approaches imply very different experimental techniques, and involve the extremes of momentum transfer spectrum. The mathematical formalism used is also very diverse: in the first case, x-dependent structure functions and parton distribution functions are used, while in the second case Q^2-dependent Dirac and Pauli form factors are employed. It seems rather intuitively natural, then, to expect that since at issue is the same particle – proton – it should be possible to construct a common "unified" formalism, which would describe both inclusive and exclusive processes. In the recent eight or so years a major effort has taken place in the scientific community to develop such a formalism, to reconcile these disjoint approaches to the nucleon structure. *Generalized Parton Distributions* (GPD in short) can be seen as generalizations to the parton distribution functions from DIS. These are hybrid objects which are meant to intrinsically describe the proton, independent of the particular reaction to which the proton participates. Given the GPD, one can describe essentially any inclusive or exclusive process involving the proton. Thorough reviews and descriptions of GPD's can be found in Ref. [18], [25] and [4]. A simple leading order model for Real Compton Scattering on proton has been developed by A.V. Radyushkin [3], based on GPD calculations.

Mathematically, for Real Compton scattering (which is the reaction of interest in this thesis) the GPD's depend on two main variables: x parton momentum fraction, as in DIS, and

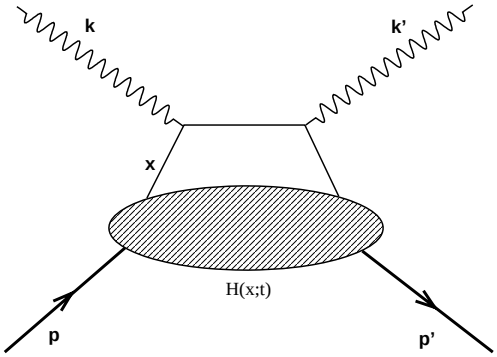

Figure 1.4: Feynman diagram for Real Compton Scattering (RCS) on a nucleon. A simple example of a model for Generalized Parton Distribution $F(x,t)$ can be found in Ref. [3]

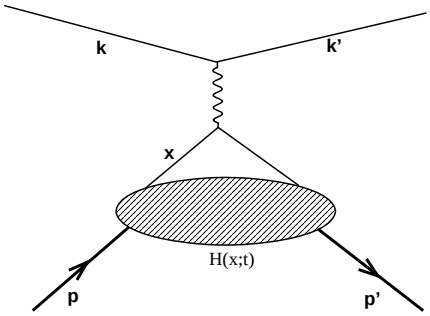

Figure 1.5: Feynman diagram for the analogous elastic electron scattering on a nucleon.

$t = -Q^2$ as in elastic electron scattering[2]. In physics terms, the GPD denotes the probability that a parton interacting with an external electromagnetic probe (the real photon, as in the case of RCS) has the momentum fraction x at a squared momentum transfer of t. For an exclusive process, such as Real Compton Scattering, the GPD represents the amplitude for a quark of momentum fraction x to be emitted by the proton, absorb a four-momentum transfer t, and then recombine with the spectator quarks to reform the proton. After having absorbed the initial photon the active quark goes into a state with a virtuality whose measure is related to s. Notice that the parton distribution functions in DIS only depend on x: the outgoing parton is real and hence has the virtuality of zero.

[2]Here it is important to note that in elastic electron scattering Q^2 denotes the virtuality of the incoming photon. In RCS however, the incoming photon is real, so Q^2 and t here denote the squared four-momentum transfer to the proton, which can be alternatively calculated by $-Q^2 = t = (k - k')^2$, where k and k' are the four momentums of the incoming and outgoing real photons

The Feynman diagram for Real Compton Scattering on proton can be seen in Fig. 1.4. The purpose of the GPD's, as already mentioned, is to form a link between inclusive and exclusive descriptions of the proton. The Optical Theorem is used to relate the DIS structure functions to the forward(i.e. $t = 0$) scattering amplitude. This allows for a crucial comparison between the two reactions (doubly Virtual Compton Scattering and DIS), and a subsequent relation between their amplitudes. This can be used to reduce the GPD's to simple Parton Distribution Functions at the limit of $t = 0$. This is a very important relation which allows us to fit the x-dependence of the GPD models to DIS data.

The next important feature of the GPD's is in the reduction relations and model independent sum rules which relate these to the electromagnetic form factors. So, for example, to receive the Dirac, Pauli and other elastic scattering form factors, we have the following relations:

$$\begin{aligned} F_1(t) &= \sum_i e_i \int_0^1 H_i(x,t)dx \\ F_2(t) &= \sum_i e_i \int_0^1 E_i(x,t)dx \\ g_A(t) &= \sum_i e_i \int_0^1 \tilde{H}_i(x,t)dx \\ h_A(t) &= \sum_i e_i \int_0^1 \tilde{E}_i(x,t)dx \end{aligned} \tag{1.10}$$

The summation is performed over all the quarks inside the nucleon, and e_i is the charge of the given quark.

For Real Compton Scattering the situation is analogous, with the only difference of the horizontal quark propagator and the extra electromagnetic vertex, which contribute a e_i/x

term in the integral:

$$R_V(t) = \sum_i e_i^2 \int_0^1 H_i(x,t)\frac{dx}{x}$$
$$R_T(t) = \sum_i e_i^2 \int_0^1 E_i(x,t)\frac{dx}{x}$$
$$R_A(t) = \sum_i e_i^2 \int_0^1 \tilde{H}_i(x,t)\frac{dx}{x} \tag{1.11}$$

Finally, as mentioned earlier, at the forward limit ($t = 0$) the GPD's need to converge with simple parton distributions (similar to $f(x)$ in Eq. 1.9):

$$H_i(x, t = 0) = q_i(x)$$
$$\tilde{H}_i(x, t = 0) = \Delta q_i(x) \tag{1.12}$$

where $q(x)$ and $\Delta q(x)$ are helicity independent and helicity dependent parton distributions.

Besides being mathematical tools for describing electromagnetic reactions on the nucleon, the GPD's have a real physical meaning. This becomes clear when one performs Fourier transformation to switch from transfered four-momentum t space to "impact parameter" space. The "impact parameter" in this case is the transverse distance between the active quark and the center of mass of the proton. Plots of detailed calculations by M. Burkardt [5] and M. Diehl [4] can be seen in Fig. 1.6 and Fig. 1.7. These plots reflect an interesting feature of the proton: as x momentum fraction decreases, the size of the proton itself increases. This can be understood simply by considering Heisenberg uncertainty principle $\Delta x\ \Delta p \sim \hbar$: when the quark momentum decreases, it's coordinate uncertainty needs to increase.

The function of the GPD's as a bridge between different types of already existing inclusive and exclusive descriptions of the nucleon is rather clear from the Eq.'s 1.10, 1.11 and

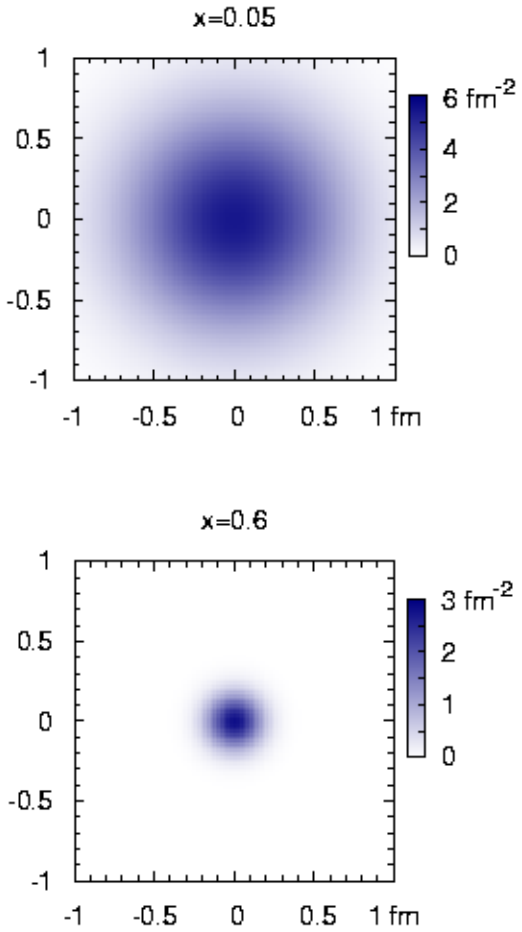

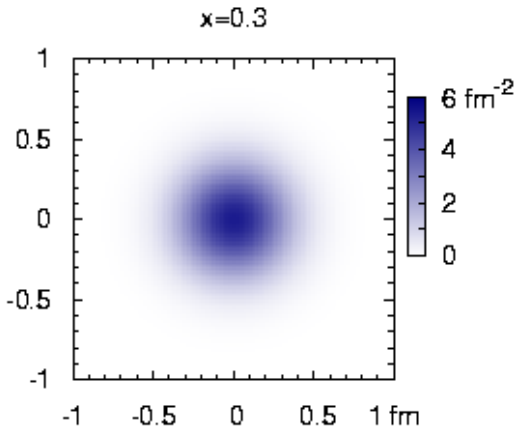

Figure 1.6: Impact parameter $\mathbf{b}_\perp = (b_x, b_y)$ distributions in the transverse $x-y$ plane for a proton, for different values of active quark's fractional momentum x [4].

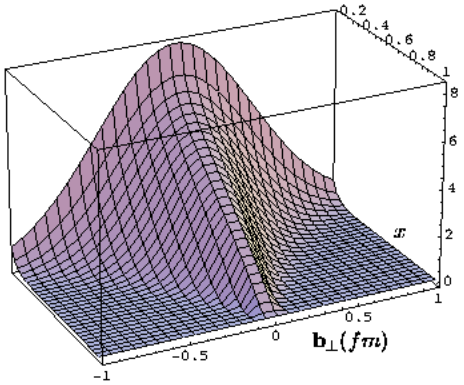

Figure 1.7: Distribution of impact parameter amplitude $b_\perp$ and fractional momentum x. [5].

2.8. Furthermore, besides describing elastic electron, Real Compton, and Deep Inelastic Scattering, the GPD's can also be used to describe other processes, such as Deeply Virtual Compton Scattering. In order to test the particular parameterizations and mechanisms used to model the GPD's, we as experimentalist use the following circumstance – the existing GPD models are based on DIS (Eq. 2.8) and elastic (Eq. 1.10)data: to be considered a robust description of the proton the GPD's must be able to *independently*(i.e. without any further adjustments) reproduce Real Compton Scattering data, as presented later in this thesis. This question will be answered later, towards the end of the thesis, and will be one of the ultimate tests for their acceptance as a universal formalism describing nucleonic structure.

Chapter 2

Compton Scattering on Proton at Medium Energies

2.1 Introduction

In the previous chapter we discussed the two major methodologies in the field of electromagnetic interactions: exclusive (elastic electron scattering) and inclusive(DIS) experiments. Furthermore, we introduced the concept of the Generalized Parton Distributions(GPD's). In this chapter we will see how GPD's can be used to determine the reaction observables for Real Compton Scattering on proton at medium energies ($4 \leq s \leq 11$, $2 \leq -t \leq 6$, in units of GeV^2)[1]. However, before we dive into discussions about nucleonic structure we need to understand Compton Scattering on a structureless Dirac particle. At the lower energies, when the proton is seen as a point particle, the simple QED calculations have yielded excel-

[1]Throughout this thesis we use Mandelstam variables s, t and u to define kinematic states. For complete definitions refer to Appendix A

lent agreements with data. At higher energies however, which is the region of interest here, the data is rather sparse.

2.2 Compton Scattering on Point Particle

Scattering of a particle of light on a charged particle has first been observed by Arthur Compton at the beginning of 20th century. Using energy-momentum conservation he correctly predicted the kinematic relations between the scattered light's wavelength, incoming light's wavelength, and scattering angle. Later on, with the advent of Quantum Mechanics, theorists O. Klein and Y. Nishina performed calculations of the scattering amplitude [26].

The two leading order Feynman Diagrams for Compton Scattering on a point particle with charge e are the following:

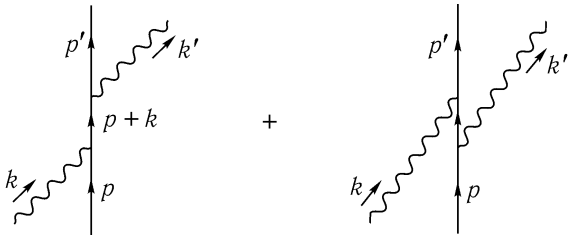

Before we start writing the scattering matrix element for this process, it is useful to look at the diagrams themselves. The fermion propagators, which determine the kinematic dependence of the scattering amplitude, are the following: $\not{s}\frac{1}{s^2}$ and $\not{u}\frac{1}{u^2}$, where s and u are the standard Mandelstam variables, and $\not{a} \equiv a_\mu \gamma^\mu$. s depends only on incoming photon beam energy and particle mass (for a fixed target). Furthermore, $-u \approx s(1-\cos\theta)/2$

decreases with scattering angle, from which it follows that unlike elastic electron scattering, where the cross section drops sharply with increasing scattering angle, the cross section for Compton scattering *increases* with scattering angle.

To determine the scattering amplitude, we use Feynman rules for fermion and boson lines, and for fermion propagators:

$$i\mathcal{M} = \bar{u}(p')(-ie\gamma^{\mu})\epsilon^{\star}_{\mu}(k')\frac{i(\not{s}+m)}{s^2-m^2}(-ie\gamma^{\mu})\epsilon_{\nu}(k)u(p) \quad + \\ \bar{u}(p')(-ie\gamma^{\mu})\epsilon_{\nu}(k)\frac{i(\not{u}+m)}{u^2-m^2}(-ie\gamma^{\mu})\epsilon^{\star}_{\mu}(k')u(p)$$

After summing over all fermion spin and photon polarization states, and after an extensive calculations of traces, which is described in detail in Ref. [27], the expression for scattering amplitude is

$$\frac{1}{4}\sum_{allspins}|\mathcal{M}|^2 \;=\; 2e^4\left[\frac{p\cdot k'}{p\cdot k}+\frac{p\cdot k'}{p\cdot k}\right]. \tag{2.1}$$

Here we have only kept the leading order terms. The variable p is the four-momentum of the fermion, k is the four-momentum of the incoming photon and k' is that of the outgoing photon. After including the phase space integral we get

$$\frac{d\sigma}{dt} \;=\; \frac{1}{2\pi}\frac{2e^4}{32(m^2+E\sqrt{E^2+m^2}+E^2)}\left[\frac{p\cdot k'}{p\cdot k}+\frac{p\cdot k'}{p\cdot k}\right]. \tag{2.2}$$

Since $p\cdot k = s-m^2 \equiv \tilde{s}$ and $p\cdot k' = u-m^2 \equiv \tilde{u}$, and since $s^2 = (m^2+E\sqrt{E^2+m^2}+E^2)$ we finally get the following simple expression for Compton scattering on a point particle:

$$\frac{d\sigma}{dt} = \frac{2\pi\alpha^2\hbar^2}{s^2}\left(\frac{\tilde{s}}{\tilde{u}}+\frac{\tilde{u}}{\tilde{s}}\right) \tag{2.3}$$

where $\tilde{s} = s-m^2$ and $\tilde{u} = u-m^2$. This result is important for two main reasons. First and foremost, this is the expression which describes Compton scattering on proton at such

low energies as 30 MeV, when the large wavelength of the photon causes it to be insensitive to proton's structure[2]. And second, this expression describes the interaction at the parton vertex in Fig. 2.4's diagram. As we will see in later discussions, the description of RCS on proton can be described through a cross section which is, in analogy with Rosenbluth formula of Eq. 1.1, a product of point Klein-Nishina cross section (i.e. Eq. 2.3) and a linear combination of form factors.

2.3 Compton Scattering on Proton: perturbative QCD

The DIS experiments showed that at such low momentum transfers as $Q^2 \sim 2\ GeV^2$ the proton's constituents already behave as an ensemble of free non-interacting particles. This lead to the intuitive conclusion that in inclusive processes and similar energies a similar pattern of behavior could be expected. According to a number of theorists [29] this implied that perturbative methods could be used to treat interaction inside the proton at these energies. A number of calculations were performed [29], which assumed the applicability of perturbative QCD (pQCD) when calculating reaction observables. These predictions were compared with the existing data of the time [6], and revealed what was perceived as good case of scaling behavior in the experimental data. Differential cross section results, however, showed dramatic disagreements with data, sometimes by orders of magnitude.

[2]It should be added that even at low energies this is only a leading order term. Such higher order QED processes as loop corrections contribute considerably to this otherwise simple picture. See Ref. [28, pp.19-20] for the full expression.

pQCD Leading Twist Mechanism

The Leading Twist Mechanism is based on the validity of the following assumptions:

- To the leading order, only the valence quarks participate in the interaction. The contribution of the sea quarks is negligible.
- The incoming photon is absorbed by one of the valence quarks, which shares the exchanged momentum with the other valence quarks though the exchange of virtual gluons. The final photon is emitted by one of the three valence quarks.
- The exchanged gluons are highly virtual: this, and the previous feature determine the "hard" scale of the interaction.
- High energy scale. The mass and transverse momentum of the partons are neglected.
- According to Brodsky-LePage hypothesis [29], scattering amplitude can be factorized into *soft* and *hard* parts, where the "hard part" denotes one that can be computed using Feynman rules for pQCD. The "soft part" denotes the parts of the process which demand a phenomenological approach.

The later statement can be schematically written as the following convolution:

$$T \;=\; \phi_{init} \otimes T_{hard} \otimes \phi_{final} \tag{2.4}$$

where ϕ are the initial and final state soft Distribution Amplitudes(DA) of the proton, while T_{hard} corresponds to the hard interaction in between. The Feynman diagram for the Leading Twist Mechanism can be seen in Fig. 2.1. The Distribution Amplitudes $\phi(x_1, x_2, x_3)$ are

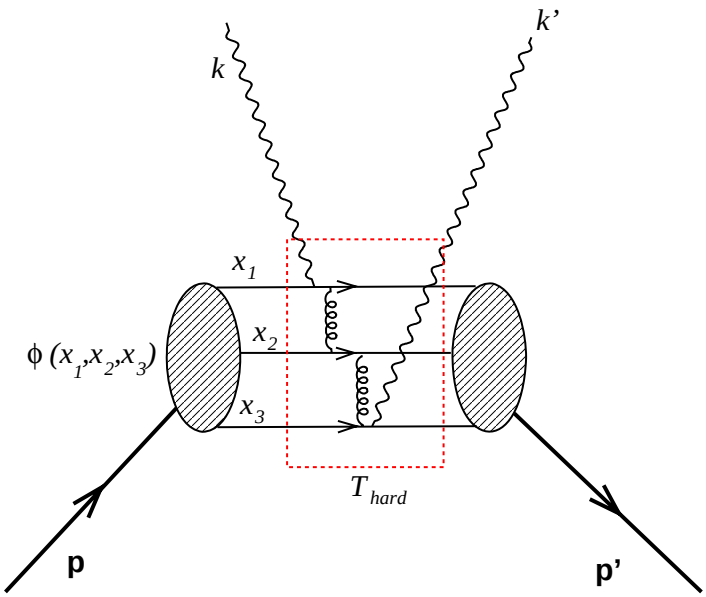

Figure 2.1: Leading Feynman Diagram for Leading Twist Mechanism. x_i stand for the fractional momentum of the quarks. The diagram enclosed by the doted box corresponds to T_{hard} from Eq. 2.4, and its amplitude can be determined using calculations based on pQCD.

somewhat similar to Parton Distributions (PDF), in that they represent the joint probability that the three valence quarks inside the proton carry fractional momentums of x_1, x_2 and $x_3 = 1-(x_1+x_2)$. The main distinction between the PDF's and DA's, however, is that PDF's are a single-body probability, representing the amplitude of a single quark of momentum x_1(i.e. all dependence on x_2 is integrated out), while the DA's represent the joint probability dependence on both x_1 and x_2. The relation between these is

$q(x_1) = \int_0^{1-x_1} \phi(x_1, x_2, x_3)\ \delta(x_1 + x_2 + x_3 - 1)\ dx_2 dx_3$.

The perturbative framework leads to one of the most rigorous scaling predictions which can be tested experimentally. When the momentum transfer to the system is very large, it is expected to start behaving like a system of free particles, in analogy with what we saw for DIS. This leads to constituent scaling rules [16], which predict the following dependence for

differential cross section:

$$\frac{d\sigma}{dt} = \frac{f(\theta_{CM})}{s^{n-2}} \tag{2.5}$$

where $f(\theta_{CM})$ is a function which only depends on the center-of-mass scattering angle, and n is the number of elementary fields in initial and final states. For Compton Scattering diagram $n = 8$.

2.3.1 Predictions for Compton Scattering

In the last twenty years there have been a number of calculations performed in the perturbative framework of Leading Twist Mechanism, with the purpose of attempting to reproduce the existing data [6]. A calculation by M. Vanderhaeghen, P. Guichon and J. Van de Wiele [30] demonstrated the technical complexity of the calculations, which involved extensive summations over 336 diagrams, representing different couplings of photons to quarks as well as different orderings of the gluon exchanges relative to the photon vertices. For the diagram of Fig. 2.1, the factorized expression of Eq. 2.4 can be written as the following helicity-dependent scattering amplitude:

$$\mathcal{M}^{hh'}_{\lambda\lambda'} = < p', h'|T_{hard}(k', \lambda'; k, \lambda)|p, h >= \tag{2.6}$$

$$= \int dx_i \; dy_i \; \phi^{\star}_N(x_i) T_{hard}(h, \lambda, x_i; h', \lambda', y_i; s, t) \phi_N(y_i)$$

Here x_i and y_i stand for the fractional momentum of the quarks in initial and final states, respectively, h and λ are the proton and photon helicity states, and s and t are the usual Mandelstam variables[3]. Notice that the Distribution Amplitudes only depend on the longitudinal momentum of the quarks: to achieve this, all dependence on transverse momentum

[3]See Appendix A for complete definitions

has been integrated over. Furthermore, the expressions for the DI's are not obvious at all – these are subject to extensive calculations and phenomenological modeling.

A number of models have been developed over time for the proton's Distribution Amplitudes. The original – and the most robust – model is the so called Asymptotic DA, which assumes that at high enough energies the quarks are essentially free non-interacting particles, and share the longitudinal momentum equally. Thus, $< x_1 >=< x_2 >=< x_3 >= 1/3$. This model however leads to predictions which underestimate the existing data by several orders of magnitude. Other models of so called Skewed Distribution Amplitudes have also been considered – labeled as CZ[7], KS[8] and COZ[9] – which involve a hadronic state with strongly asymmetric distribution of momentum, where one of the quark is assumed to carry almost all of the longitudinal momentum. This leads to higher values of cross sections, however, this approach also has a number of intrinsic self-contradictions, as will be discussed later. Plots of $\phi(x_1, x_2)$ DA's for KS and COZ models can be seen in Fig. 2.3.

Determination of the $T_{hard}(h, \lambda, x_i; h', \lambda', y_i; s, t)$ factor in Eq. 2.7 is subject to perturbative QCD calculations, and is, from a physics point of view, the most straightforward aspect of the equation. But even here, however, there are a number of complexities. First, as many as 336 independent diagrams have to be determined and summed into a final amplitude. The internal gluon lines in the box of Fig. 2.1 correspond to propagators of the form $1/q^2$ where q^2 is the virtuality of the gluon. If the gluon goes on mass shell, i.e. when $q^2 = 0$, this causes singularities in the integrals which make part of T_{hard}. Different approaches to these singularities, even for a given DA, lead to very different predictions.

Comparisons with Previously Available Data

The primary criteria of interest in data-to-theory comparisons has been the predicted s^{-6} dependence in cross section, as determined in Eq. 2.5. The plot in Fig. 2.2 presents previously available cross section measurements [6]. The data is plotted in $f(\theta_{CM}) = s^6 \cdot d\sigma/dt$ vs. θ_{CM} (see Eq. 2.5) to reveal what seems to be a considerable case of s^{-6} dependence in the cross section. It should be noted that, due to uncertainties in theoretical approaches to the DI's, the scaling predictions are by far the most robust features of the pQCD framework. It is then understandable that the observation of the scaling at the time resulted in a belief that the Leading Twist Mechanism was overall valid, and that it was only a matter of choosing the correct DA's in order to completely explain the data.

The first attempt to describe the data was done by using asymptotic DA's with a maximum at $x_1 = x_2 = x_3 = 1/3$. However, as can be seen in Fig. 2.2, with asymptotic DA the Leading Twist contribution underestimates measurements by approximately two orders of magnitude, and completely fails to describe the data. Furthermore, Leading Twist calculations have been used to determine the elastic form factors for the proton and neutron. It has been found that the calculated value for proton's magnetic form factor G_M (see Eq. 1.1) is zero; the prediction for neutron magnetic form factor has a wrong sign, with the absolute magnitude being two orders of magnitude below the data [31].

It was then argued that the proton DI's must be asymmetric to reflect the fact that the u quarks carry a relatively larger fraction of proton's momentum than the d quarks. Different model for humpy nucleon DI's have been presented, by V.L Chernyak, A.A. Ogloblin, I.R. Zhitnitsky (labeled as CZ and COZ [7] [9]), I.D. King and C.T. Sachrajda (labeled as KS

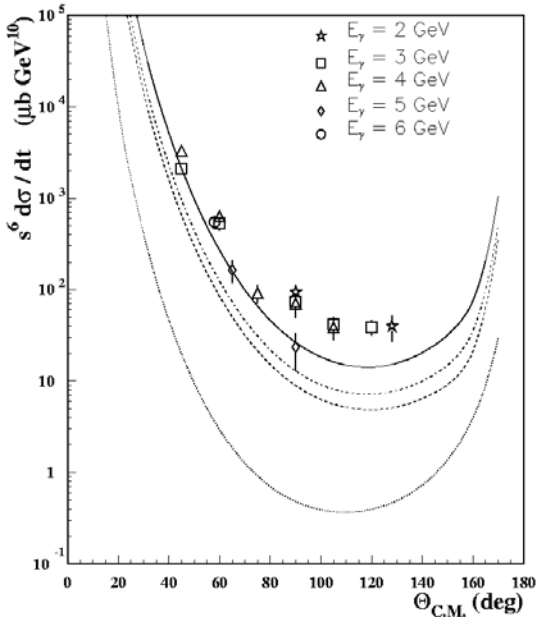

Figure 2.2: Plots of data from Ref. [6], and pQCD predictions using different DA's: CZ [7] (dashed), KS [8](full),COZ [9](point-dashed), and asymptotic (doted).

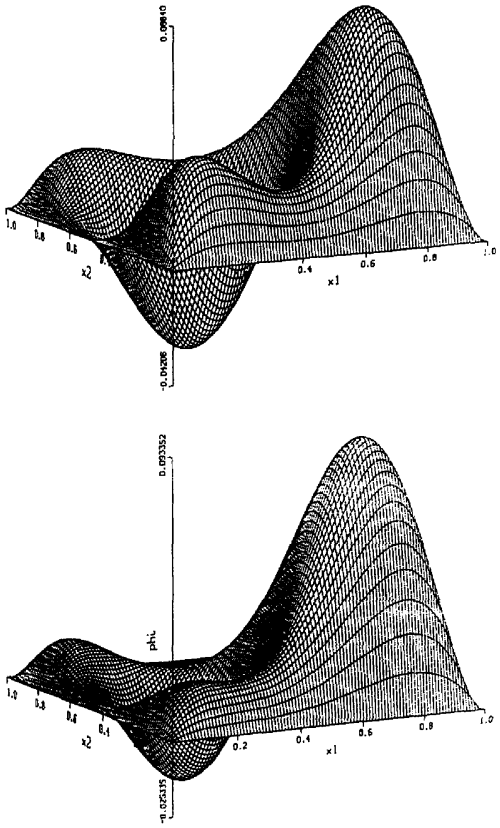

Figure 2.3: Plots of Skewed DA's: KS(top) [8] and COZ(bottom) [9].

[8]), where the fractional momentum was strongly concentrated in one quark, leaving the other quarks with $x_2 \sim 0,\ x_3 \sim 0$:

$$\phi^{CZ}(x_1, x_2, x_3) \ = \ \phi^{as} \cdot (1.69 - 9.26x_1 - 10.94x_3 + 22.7x_1^2 + 13.45x_3^2 + 9.26x_1x_3)$$

where ϕ^{as} is the asymptotic DA.

The main assumption behind the humped(or skewed) distribution amplitudes, as thoroughly criticized in Ref. [17] and Ref. [3, p. 114008-6], is based on the assumption that it is valid to use the perturbative expressions of $\not{k}/k^2$ and $1/k^2$ for quark and gluon propagators even for such low virtualities as $k^2 \approx (0.3\ GeV)^2$. It is safe to say that this is

somewhat contradicting the requirement that the interaction take place on the hard scale. Furthermore, it then becomes clear why the CZ-like distribution amplitudes (similar to the expression above) cause a major amplification of the scattering amplitude. For a humpy DA, the average x for the active quark is almost 1, while that of the others passive quarks is close to zero. This is the configuration that contributes greatly to the amplitude, since small values of $k^2 \sim 0$ result in very large values of the $1/k^2$ and $\not{k}/k^2$ propagators, which in their turn cause a major enhancement of the cross section. From this it follows that in order to achieve Leading Twist contributions which are larger than those provided by the asymptotic DA, the perturbative expressions $1/k^2$ and $\not{k}/k^2$ for the propagators have to be valid down to very low virtualities. This, as already mentioned, is a rather unclear. Low virtualities for gluons imply low energies and hence very strong couplings (which produce large scattering amplitudes), which makes this approach inherently inconsistent: perturbative assumptions are used to treat a process which is clearly nonperturbative.

It has to be added that besides the above discussed issues, evidence against humpy DA's has been also provided by lattice calculations [32]. It has been shown that very moderate shifts from the maximum point of $x_1 = x_2 = 1/3$ are sufficient to account for the observation that u quarks carry relatively larger proportion of the longitudinal momentum [33]. Such a small shift however will not produce the drastic enhancements needed to amplify the predictions to the point of agreeing with the existing data.

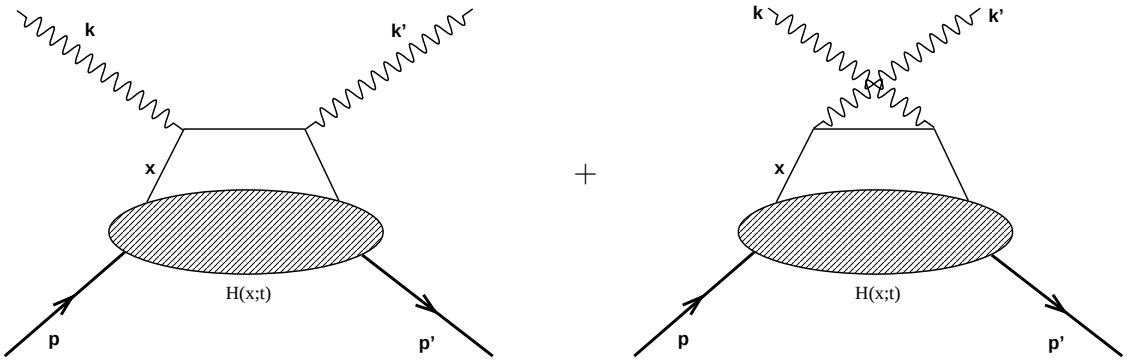

Figure 2.4: Leading order Feynman diagrams for Real Compton Scattering in the framework of Soft Overlap "Handbag" Mechanism.

2.4 Soft Overlap "Handbag" Mechanism

As already discussed in the previous section, major discrepancies have been observed between the existing measurements and the predictions of Leading Twist Mechanism. This has motivated a different approach to the problem of understanding nucleon structure at the energies and momentum transfers typical to medium energy regime. An alternative mechanism developed over the recent ten years involves only one active quark in the interaction, leaving the remaining quarks as spectators. This approach argues that the active quark absorbs the momentum transfer from the photon, and re-emits a final photon without exchanging any hard gluons with the rest of the proton. The energies of the gluons in Fig. 2.1 do not correspond to the hard scale, and hence these soft gluons cannot be represented in the hard perturbative section of the diagram.

Similar to Leading Twist mechanism, the Handbag mechanism is based on a set of key assumptions:

- Both valence and sea quarks participate to the interaction.

- All the momentum transfer is absorbed by the active quark, no hard gluons are exchanged with the spectator quarks, and the momentum is shared with the rest of the proton through overlaps of non-perturbative "soft" proton wave-function.

- Scattering amplitude can be factorized into the hard part, describing the active quark's interaction with the external photons (and determined in the perturbative QCD framework), and the soft non-perturbative part, describing its interaction with the rest of the proton.

- The mass and transverse momentum of the quarks are not neglected, but rather play an important role in linking the active quark with the other constituents of the proton.

- A symmetric reference frame is chosen in such a manner as to make the skewedness vanish:

$$\xi = \frac{(p - p')^+}{(p + p')^+} = 0$$

(see Ref. [3] for definitions of skewedness and light-cone frame of reference)

The leading order Feynman diagrams for the Handbag Mechanism can be seen in Fig. 2.4. As can be seen from comparing Fig. 2.4 to Fig. 2.1, the main difference between Leading Twist Mechanism and Handbag Mechanism is condensed in the second point of the above list of assumptions: if Leading Twist treats the gluons of the diagram of Fig. 2.1 perturbatively, the Handbag Mechanism assumes that pQCD is not a valid framework for treating the gluons and hence isolates the soft gluonic exchanges into the soft overlap wave-function of the proton. It has to be added that the Soft Overlap and Leading Twist Mechanisms are in no way mutually exclusive formalisms: as just described, the Soft Overlap Mechanism is

really a power correction to the Leading Twist. Furthermore, at issue here is the *dominance* of a particular mechanism. It is commonly agreed upon that at very high energies the Leading Twist is the asymptotically dominating mechanism. It is however not clear as to what is the appropriate energy scale. This is the topic of interest of this thesis, and this is the question that we will try to answer.

2.4.1 Compton Scattering Form Factors through Generalized Parton Distributions

In the previous chapter we already discussed the nature of the Generalized Parton Distributions. Here we will describe the methodology of applying the GPD formalism to the Soft Overlap Mechanism, with the purpose of a schematic description of how GPD's can be extracted from the overlap of the soft wavefunctions for the initial and final states of the proton. The Double Distributions (DD), which were the predecessors of the GPD's in that besides x they also depend on the quark's fractional momentum y in the final state, were first used by A.V. Radyushkin [3] do determine the GPD's. His work was closely followed by M. Diehl, P. Kroll *et al.* who instead used a Fock state expansion for the wave function parameterization [19; 20; 34]. In this section however we will follow the formalism adopted by A. Radyushkin, due to its relative simplicity (in that it doesn't include any next to leading order corrections) and rather intuitive approach. Furthermore, since we are dealing with Real Compton Scattering, in all discussions we assume skewedness a ξ equal to zero (see Ref. [3, pp.2-3]).

By definition, the GPD's specify the probability of obtaining a quark with the fractional

momentum xp for a given momentum transfer of $t = (p-p')^2$, where p and p' denote proton's initial and final momentums. In order to describe a physical proton, the GPD's need to obey a number of reduction relations, such as

$$\sum_i e_i \int_0^1 H_i(x,t)dx = F_1(t)$$
$$\sum_i e_i \int_0^1 E_i(x,t)dx = F_2(t) \tag{2.7}$$

which reduce them to the known elastic electromagnetic form factors. Furthermore, a very useful relation can be extracted from comparing *doubly virtual* Compton Scattering (i.e. both photons are virtual) to Deeply Inelastic Scattering. Using the optical theorem, the imaginary part of the forward (i.e. $t = 0$) virtual Compton amplitude will give us the DIS structure functions(see, e.g., Ref. [35]). From here it can be shown that:

$$H_i(x, t = 0) = q_i(x)$$
$$E_i(x, t = 0) = \Delta q_i(x) \tag{2.8}$$

where $q(x)$ and $\Delta q(x)$ and the helicity independent and helicity dependent parton distributions. Since both $q(x)$ and $\Delta q(x)$ are very well known and measured functions, this relation reduces considerably the complexity of the modeling. Furthermore, Eq. 2.7 and Eq. 2.8 show the hybrid nature of the GPD's – they are related both to the regular parton distributions and to the form factors, serving as a connection between the inclusive and exclusive formalism of nucleon structure.

To the lowest Fock state the initial and final states of the proton can be described by a light cone wave function $\Psi(x, k_\perp)$, where $k_\perp$ is the transverse momentum of the quark. The elastic electron scattering Feynman diagram for this representation can be seen in Fig. 2.6.

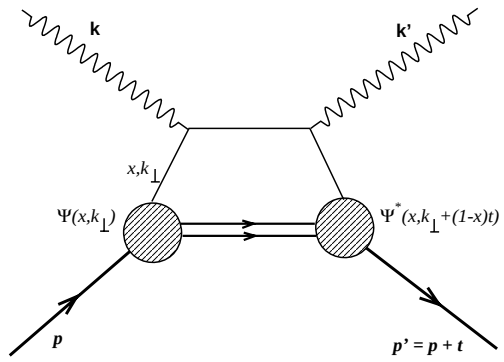

Figure 2.5: Two-body contribution to RCS form factor.

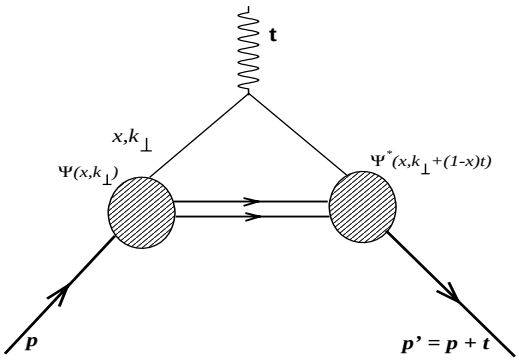

Figure 2.6: Two-body contribution to elastic form factor.

By choosing a frame of reference where the momentum transfer t is entirely transverse, the two-body contribution into the form factor can be expressed as [36]

$$F_1^{tb}(t) = \int_0^1 dx \int \Psi^*(x, k_\perp + \bar{x}t) \cdot \Psi(x, k_\perp) \frac{d^2k_\perp}{16\pi^3}. \tag{2.9}$$

where $\bar{x} = 1 - x$ is the fractional longitudinal momentum of the rest of the proton.

This integral, which is the overlap of the initial and final state soft wavefunctions, corresponds to the lower non-perturbative half of the diagram in Fig. 2.5. It includes in itself the probability of emission and re-absorption of a quark with fractional longitudinal momentum x and transverse momentum $k_\perp$, and contains innumerable soft gluon interactions between the active quark and the rest of the proton. Comparing this expression to Eq. 2.7, we can identify

$$H(x,t) = \int \Psi^*(x, k_\perp + (1-x)t) \cdot \Psi(x, k_\perp) \frac{d^2k_\perp}{16\pi^3}. \tag{2.10}$$

The key of the problem then is to choose a reasonable model for the wave function $\Psi(x, k_\perp)$. Assuming a Gaussian dependence on the transverse momentum [36] one can write

$$\Psi(x, k_\perp) = \Phi(x)\ e^{-k_\perp^2/2x\bar{x}\lambda^2} \tag{2.11}$$

Here λ is a measure of the transverse size of the proton in momentum space. The meaning of $\Phi(x)$ becomes more clear when one computes the overlap integral to determine GPD $H(x,t)$:

$$H(x,t) = q(x)\ e^{\bar{x}t/4x\lambda^2} \quad \text{where} \quad q(x) = \frac{x\bar{x}\lambda^2}{16\pi^2}\Phi^2(x) = H(x,t=0)$$

where, as before, $q(x)$ is the two-body part of the parton distribution. To be precise, this is only the simplified model for the GPD, which only includes the two-body contribution. For the total result the higher Fock components need to be added as well. These contributions are by far not small, however the purpose here is to provide the basic idea behind the GPD formalism [3].

It is now important to understand the role of different variables and functions which make part of $H(x,t)$. Variable λ, as mentioned, specifies the average transverse momentum carried by the quarks, and it can be shown that $< k_\perp^2 >= \lambda^2 \int_0^1 x\bar{x}f(x)dx$ for the down quark. It is determined by using Eq. 2.7 to relate $H(x,t)$ to $F_1(t)$ form factor, and then by fitting it to the available form factor data, using λ as a free parameter, to achieve $\lambda^2 = (0.84GeV)^2$ [3].

Once the GPD's are modeled, it is then possible as well to compute the Real Compton Scattering axial and vector form factors, in an analogy with the already discussed elastic form factors [3]:

$$\begin{aligned} \sum_i e_i^2 \int_0^1 H_i(x,t)\frac{dx}{x} &= R_V(t) \\ \sum_i e_i^2 \int_0^1 \tilde{H}_i(x,t)\frac{dx}{x} &= R_A(t) \end{aligned} \tag{2.12}$$

Notice the main differences between the expressions for elastic form factors(Eq. 2.7) and RCS form factors above: the charge in the later case is squared, and an extra $1/x$ term is present in the integral. These features reflect the presence of an extra electromagnetic coupling

vertex and an extra quark propagator (compare the diagrams in Fig. 2.5 and Fig. 2.6).

Real Compton Scattering Cross Section

To the leading order, the expression of RCS cross section is very similar to elastic electron scattering Rosenbluth cross section, in that it consist of a product of the point cross section and a combination of electromagnetic RCS form factors:

$$\frac{d\sigma}{dt} = \frac{d\sigma_{KN}}{dt}\left\{f_V R_V^2(t) + (1 - f_V)R_A^2(t)\right\} \tag{2.13}$$

where in place of Mott cross section we have Klein-Nishina point Compton scattering cross section

$$\frac{d\sigma_{KN}}{dt} = \frac{2\pi\alpha^2}{s^2}(\frac{\tilde{s}}{\tilde{u}} + \frac{\tilde{u}}{\tilde{s}}) \tag{2.14}$$

and the kinematic factor f_V is $f_V = (\tilde{s} - \tilde{u})^2/2(\tilde{s}^2 + \tilde{u}^2)$. Due to our kinematic settings, $f_V \approx 1$. This then allows for a very interesting approach to the problem of relating the data to the theoretical prediction: instead of comparing $d\sigma/dt$, we can use another criteria as an experimental test of the theory –

$$\frac{d\sigma/dt}{d\sigma_{KN}/dt} = R_V^2(t) \tag{2.15}$$

This is a remarkable result, in that it depends only on the Mandelstam variable t, but not on s. It is of course possible to compare the predictions of cross section to those extracted from the data. However, a particular model for a GPD employs a specific parameterization, and the final result for the form factors is vulnerable to model-dependent uncertainties. However, if the Soft Overlap Mechanism is *overall* correct, then the ratio of Eq. 2.15 may deviate from

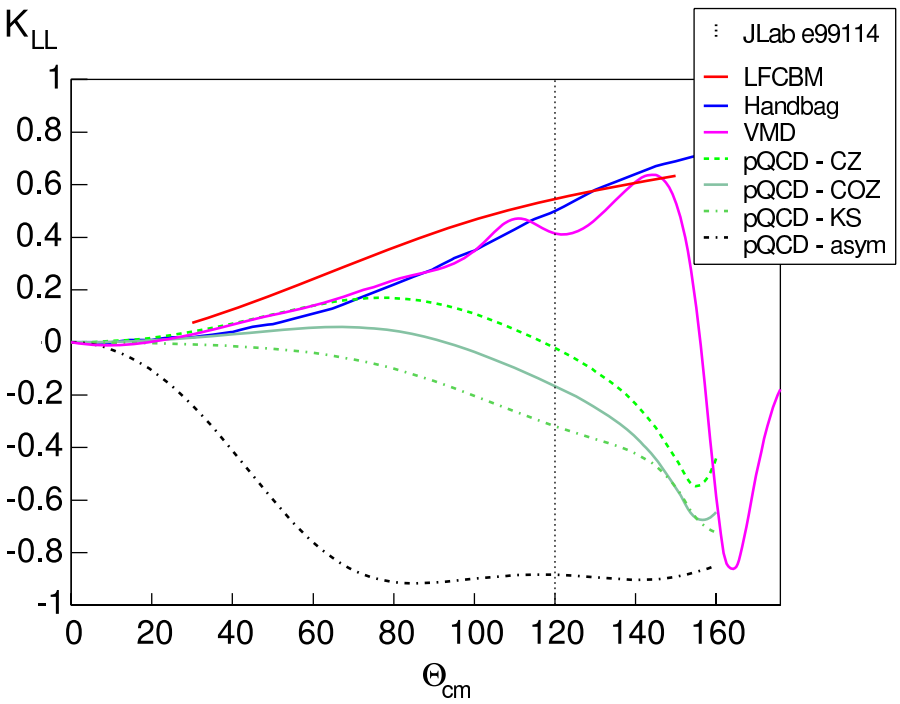

Figure 2.7: Currently available predictions for polarization transfer asymmetry K_{LL}: Leading Twist (green), Soft Overlap Handbag (blue), LFCBM and Regge exchange.

the theoretical prediction for the form factor, but it should be only dependent on t, and not on any other variables.

This is a very powerful test, since it allows us to isolate any "low order" model dependencies, and test the overall applicability of GPD formalism. With this goal in mind, the kinematic settings in the experiment have been chosen such as to allow measurements at different values of s with same t, to test whether $d\sigma/d\sigma_{KN}$ is independent of s.

2.4.2 Compton Scattering Polarization Transfer Asymmetry through GPD's

Up to now the discussion of the reaction observables has been centered around the RCS cross sections, as a primary observable of the interaction. However, the helicity amplitudes of Eq. 2.7 can also be used to determine various spin observables for Compton scattering on the proton. The asymmetry measurements of the polarization transfer in the $\vec{\gamma}p \to \gamma\vec{p}$ reaction (where the vector denotes a polarized state) involve a two-spin correlations between the initial polarized photon and the recoil proton, which carries the transfered polarization. The longitudinal polarization transfer is defined as follows:

$$K_{LL} = \frac{d\sigma(+,\uparrow) - d\sigma(-,\uparrow)}{d\sigma(+,\uparrow) + d\sigma(-,\uparrow)} \tag{2.16}$$

where the first entry in the cross section refers to the photon beam helicity, and the second entry refers to the *recoiled* proton polarization. The polarization transfer asymmetry calculation for Handbag Mechanism results in the following expression [19]:

$$K_{LL} = \frac{d\sigma_{KN}}{d\sigma} K_{LL}^{KN} R_V(t) R_A(t) \tag{2.17}$$

where $K_{LL}^{KN} = (\tilde{s}^2 - \tilde{u}^2)/(\tilde{s}^2 + \tilde{u}^2)$ is the longitudinal asymmetry for a Klein-Nishina scattering on a point particle. Using the earlier result from Eq. 2.15 for vector form factor we receive

$$K_{LL} = K_{LL}^{KN} \frac{R_A(t)}{R_V(t)} \tag{2.18}$$

The GPD calculations for the R_A/R_V ratio predict a number which is rather close to one. Meanwhile, the Leading Twist predictions for the K_{LL} produce results which are negative in value. A full comparison of different theoretical predictions can be seen in Fig. 2.7, with the

doted vertical line denoting the center-of-mass angle of the measurement. The scientific value of the polarization transfer measurement then becomes clear in light of the wide contrast between the predictions of the Handbag and Leading Twist Mechanism. Furthermore, unlike cross section measurements, where uncertainties due to humpy DA's are rather large, for the polarization transfer asymmetry calculations with even the most extreme DA's produce results that are still very far from the Handbag predictions.

Another aspect of the polarized measurements, which can be of a great use for determining the RCS form factors, is that the measurement of K_{LL}/K_{LL}^{KN} can be used to determine the ratio of R_A/R_V. This can be utilized to refine our previous rather approximative approach of Eq. 2.15 when determining the vector form factor $R_V(t)$:

$$R_V(t) = \left(\frac{d\sigma}{d\sigma_{KN}}\right)^{1/2} \quad [f_V + \alpha(1 - f_V)]^{-1/2} \tag{2.19}$$

where $\alpha \equiv R_A(t)/R_V(t) = K_{LL}/K_{LL}^{KN}$ is determined from the polarized results.

2.5 Summary

In this chapter we discussed the theoretical background and physics motivation behind the experiment. The main purpose of the experiment is

a) Test the scaling predictions of Leading Twist Mechanism, by determining the value of n in Eq. 2.5 to a high precision. To this end, data has been taken at to allow grouping of different data sets with same θ_{CM} but different s, which will allow us to perform a fit of cross section values to determine n.

b) Test the predictions of Soft Overlap "Handbag" Mechanism, by

1. comparing differential cross section measurements with theoretical calculations

2. testing the ratio $d\sigma/d\sigma_{KN}$ (see Eq. 2.15) for s independence

c) From the above comparisons, determine and identify the dominant mechanism at medium energies.

Chapter 3

Experimental Apparatus

The E99-114 "Real Compton Scattering" experiment (RCS) was performed in the Hall A of Thomas Jefferson National Accelerator Facility. The purpose of the experiment was to perform measurements of two observables for the $p(\gamma, \gamma' p)$ reaction: the differential cross sections for Compton scattering on proton over a wide range of scattering angles and incident energies; and asymmetries of polarization transfer to the proton [37]. The kinematic coverage of the experiment is quite extensive: Mandelstam variable s varied between $4.82 GeV^2$ and $10.92 GeV^2$, and $-t$ varied between $1.64 GeV^2$ and $6.46 GeV^2$. For a full listing of kinematic and experimental settings refer to Table 6.4. Throughout the experimental run the beam current varied in between $5\mu A$ and $60\mu A$, and a copper radiator with the thickness of 6% of copper's radiation length was employed to produce a bremsstrahlung photon flux. The resulting mixed beam of electrons and photons impinged on a $15cm$ liquid hydrogen cryo-target.

During the experimental run the scattered and recoiled particles are detected in coinci-

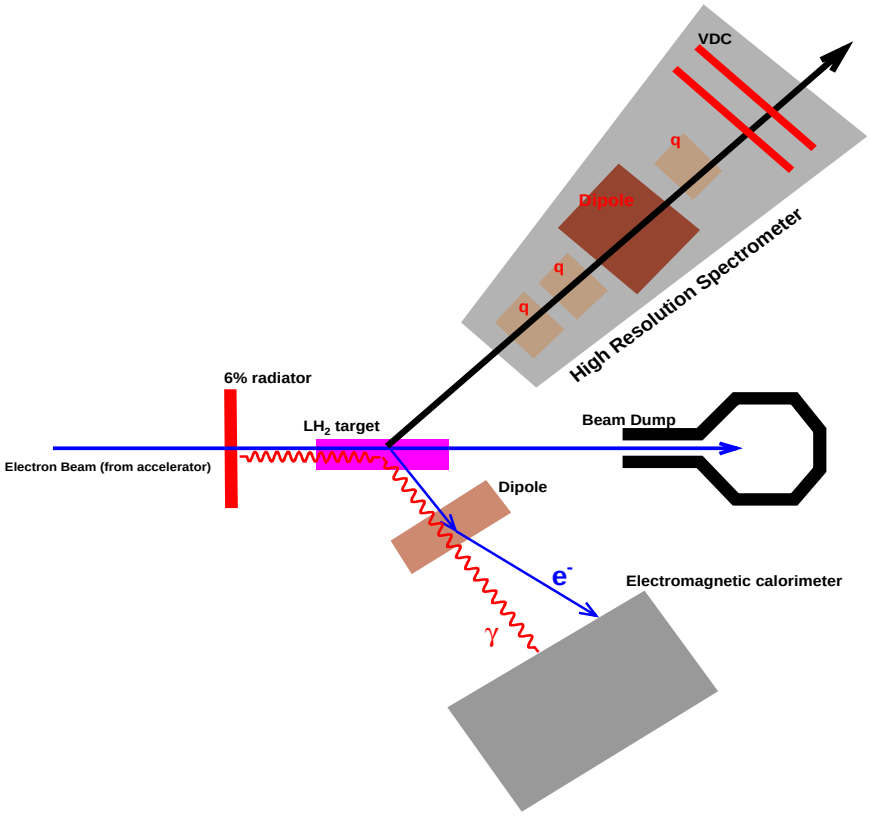

Figure 3.1: Experimental Setup of Hall A for E99-114 experiment

dence by the RCS photon spectrometer and Hall A High Resolution Spectrometer (HRS), respectively. The photon spectrometer is an electromagnetic calorimeter, built as a highly segmented array of lead glass blocks, which fully absorb the energy of the incoming particle. The High Resolution Spectrometer on the other hand consists of a number of magnetic quadrupoles and a dipole which performs momentum separation. It contains a focal plane detector package, which, to a very high resolution, can measure proton's focal plane variables, in order then to reconstruct the vertex variables using known optic transformations. A very high combined resolution is needed in order to distinguish the primary $p(\gamma, \gamma' p)$ reaction from the background of $p(e, e' p)$ and $p(\gamma, \pi^0 p)$ processes. The schematic experimental setup can be seen in Fig 3.1.

3.1 The Thomas Jefferson National Accelerator Facility

The Thomas Jefferson National Accelerator Facility(TJNAF, also referred to as Jefferson Lab or JLab), was commissioned and built in the 1980's as part of general motivation to explore and study the hadronic structure on the GeV scale. The laboratory was designed and developed in collaboration between US Department of Energy and Southern Universities Research Association. The first experimental run with scientific results was performed in 1995. In the last ten years hundreds of experiments have been conducted, providing data of critical value to our understanding of nucleon and nuclear structure at this energy scale [38]. TJNAF research program consists of an accelerator – Continuous Electron Beam Accelerator Facility (CEBAF) – and three experimental halls where the actual experiments are performed, as well as a number of laboratories for testing and preparation of experimental apparati.

CEBAF is one of the few modern accelerators which provide a continuous high duty factor beam of high current (from $1nA$ to $120\mu A$), and use cryogenic accelerating radio-frequency (RF) cavities and cryogenic magnets for deflecting, focusing and accelerating the beam. The general diagram of the accelerator, with the three halls, can be seen in Fig. 3.2. The electrons are produced by a strained gallium arsenide photocathode under vacuum, which is subjected to radiation from three $499MHz$ gain switch diode lasers. By controlling the phase shift between the lasers, one can produce three mixed electron beams, spaced by $2\pi/3$, after which each can be accelerated separately and be simultaneously delivered to each of

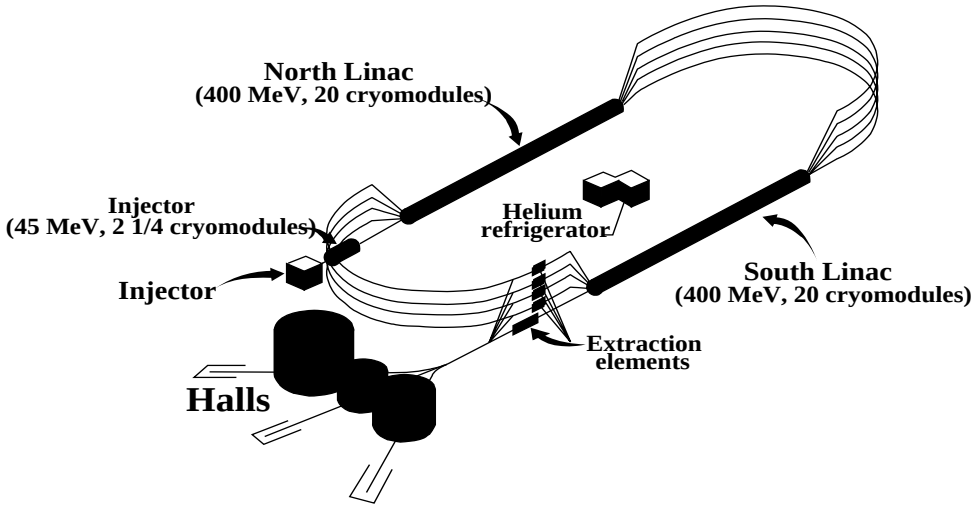

Figure 3.2: Schematic view of CEBAF. The electron beam is produced in the injector, after which it is accelerated in each of the two superconducting linacs. The beam can be circulated up to five times, resulting in an energy of apprx. $5.75GeV$.

the experimental halls. This methodology essentially triples the statistic productivity of the laboratory. Furthermore, the laser light can be polarized both circularly as well as linearly, producing circularly or linearly polarized electrons.

Once the beam is produced it is sent into the first linear accelerator (linac), which consists of 20 cryomodules, each accelerating the electrons by approximately $30MeV$. The cryomodules are made of Niobium and are made of four consecutive cavities, which need to be cooled by liquid helium at a temperature of $2K$, in order to keep the cavities in the phase of superconductivity. The advantage of using superconductors instead of room temperature conductors is that the skin depth of the metal in room temperature is equal to the wavelength of the RF wave, allowing it to penetrate and heat the metal. This brings about a number of problems – energetic loss being the smallest of those. Specifically, the heating causes the cavity to enlarge, changing its natural frequency and de-synchronizing the accelerator. With superconductors these problems are absent, which allows for the use of very powerful RF

fields for acceleration. The use of an RF field of that power in simple conductor would result in a meltdown of the cavity.

After going through the first linac, the beam goes through the recirculation arc, which sends the beam to the second(identical to first) linac. The two arcs of the accelerator consists of a combination of dipoles (to steer the beam), quadrupoles and sextupoles (to focus the beam) as well as septum elements. Once the beam traverses the second linac it enters the second arc, hence restarting the cycle – with an additional energy of $1.15GeV$. This cycle can be repeated 5 times, resulting in a beam with the energy of $5.7GeV$.

3.2 Experimental Hall A of Jefferson Lab

Hall A is one of the three experimental halls of Jefferson Laboratory. It contains a pair of magnetically identical High Resolution Spectrometers (HRS), which can be rotated around the center of the hall (where the target is positioned) in order to detect the scattered and recoiled particles. Upstream from the target there is a series of apparati which measure the beam parameters – such as energy, current, position and polarization – to a very high precision. The hall has a series of different type of targets, such as waterfall target, cryogenic hydrogen, deuterium and helium targets, as well as an assortment of solid targets [39].

3.2.1 Beamline setup

A detailed measurement of electron beam parameters needs to be performed before that beam can be used for experimental purposes. These measurements are performed by several

devices placed upstream from the target. These measure the exact position of the beam, its polarization and its energy. Furthermore, before reaching the target the beam needs to be rastered in order to prevent overheating of the target, which may result in either target damage, or (for liquid targets) in boiling, which in its turn will cause a dramatic drop in luminosity.

The position of the beam at the vertex is implicitly measured by two Beam Position Monitors (BPM). The first BPM is placed $7m$ upstream from the target, while the second one is only $1m$ away. Each BPM has four antennae. An Eddie current is induced in the antennae as the beam packed passes by, and the relative amplitudes of the currents can be used in order to determine the distance of the beam from each of the four antennae. This allows for a precise determination of beam position relative to the two BPM's. The positions of the BPM's relative to each other and relative to the target have been thoroughly surveyed, which allows for a calculation of beam position at the center of the target using a linear extrapolation.

The Beam Current Monitors (BCM), which measure the accumulated integral charge of the beam, are based on a principle which is similar to that of the BPM's. The BCM's are located $24m$ upstream of target. A BCM consists of a cylindrical resonant cavity, whose natural frequency is equal to that of the beam, and has a coaxial loop antenna. As the beam packet passes it induces a current in the loop of the antenna, which can then be measured and the charge can be calculated. The time derivative of the accumulated charge is used to monitor the beam current.

There are two different methods to measure the energy of the incoming beam. As the

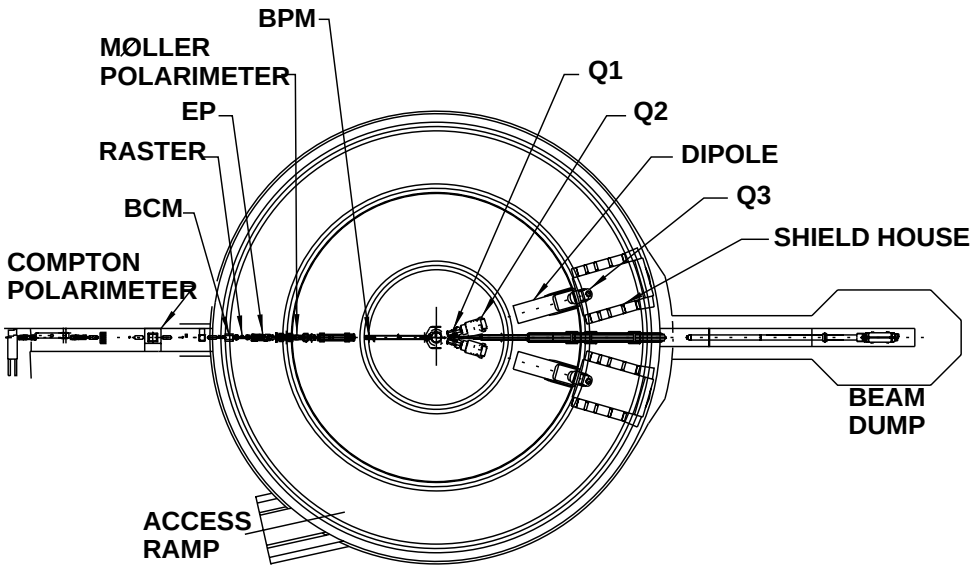

Figure 3.3: Schematic layout of Hall A beam setup and relative positioning of the two High Resolution Spectrometers.

beam traverses the tunnel from the beam switch-yard to the hall, it is being deflected by the dipole magnets by an average angle of 34.4^o. Variations from this value are measured to a high accuracy by a set of wire scanners. Having the precise knowledge of the dipole magnetic fields and deflection angle, one can calculate the energy of the beam. A second method uses the $p(e, e'p)$ elastic process: the beam traverses a thin polyethylene (CH_2) target, and the measurement of the recoiled proton's track by a silicon strip detector is used for a kinematic calculation of incoming electron's energy. The combination of the two methods allows for a determination of energy with a relative accuracy of 2×10^{-4} parts.

The general layout of the beamline can be seen in Fig. 3.3.

3.2.2 Cryogenic Target and 6% Cu Radiator

Hall A employs a number of different liquid targets, each with an independent fluid transfer systems. The E99-114 experiment used a liquid hydrogen target, with a copper bremsstrahlung radiator attached [40].

The different targets are attached to a vertically positioned ladder system, which can be remotely controlled to move up and down, aligning the target cell of choice with the beam. The target ladder itself is placed inside a target vacuum chamber, which is directly connected to the beam pipe, and has two wide aluminum windows of $0.34mm$ thickness. The width of the windows covers the full $\Theta_{HRS} \in (12.5^o, 165^o)$ angular domain of the spectrometers.

The liquid target cells which hold the actual target material are made of aluminum cylinder with a semi-spherical cap, with a length of $15cm$ and a diameter of $63.5mm$. Development of the target cell has been a very complicated challenge, since it is very important to keep the target wall thicknesses to the minimum in order to limit background multiple Coulomb scattering. The target thicknesses are $71\mu m$,$102\mu m$ and $178\mu m$ for the upstream windows, downstream cap and target side walls, respectively. Since the exterior of the cell is at vacuum and the interior is subjected to the pressure of the pumping system, the pressure experienced by the cell is $0.17MPa$.

Boiling of the cryotarget is one of the undesired events during experimental run. The transition from liquid to gaseous phase results in a drop of density, which dramatically reduces the luminosity of the experiment. Given the narrow beam profile this would be inevitable with the high beam currents used in Jefferson Lab. To avoid target boiling, the beam is being rastered at frequencies of $17kHz$ and $24kHz$ in the horizontal and vertical

planes by two dipole magnets, in this manner distributing the deposited heat over a larger volume. Meanwhile, the target fluid is recirculated through a complex system of fins, to insure a uniform heat exchange.

The increasingly high energies of our experiment imply decreasingly low cross sections. Keeping in mind that the combined acceptance of the experimental setup is rather limited, it becomes clear that a very high photon flux is needed in order to achieve acceptable statistic accuracies. One method to produce a photon flux is to use a thick "radiator" – a material whose nuclei's electric field will interact with incident electrons and cause them to produce breaking radiation, or bremsstrahlung. The bremsstrahlung radiator, built to produce a photon beam, is attached to the liquid hydrogen target. It is composed of a set of copper foils, whose total thickness is equal to $0.81 g/cm^2$. This is equal to the 6.2% of copper's radiation length. As described before, the beam incident on the radiator consists of highly monochromatic electrons. The energy loss of the electrons is proportional to Z^2, where Z is the atomic number of the radiator material.

The process of "external" bremsstrahlung is quite well understood, which is what makes it a very useful tool for performing a whole category of experiments, such as Compton scattering, neutral pion photoproduction experiments, deuderon photodisintegration experiments etc. A detailed calculation, describing bremsstrahlung has been performed by J.L. Matthews and R.O. Owens [41] during 1970's. A plot of the bremsstrahlung spectrum and corresponding electron spectrum for radiation from a material with a thickness of 6.84% radiation lengths and an incoming electron energy of $3.474 GeV$ can be seen in Fig. 3.4.

The result of the above described procedures is a mixed electron-photon beam, since

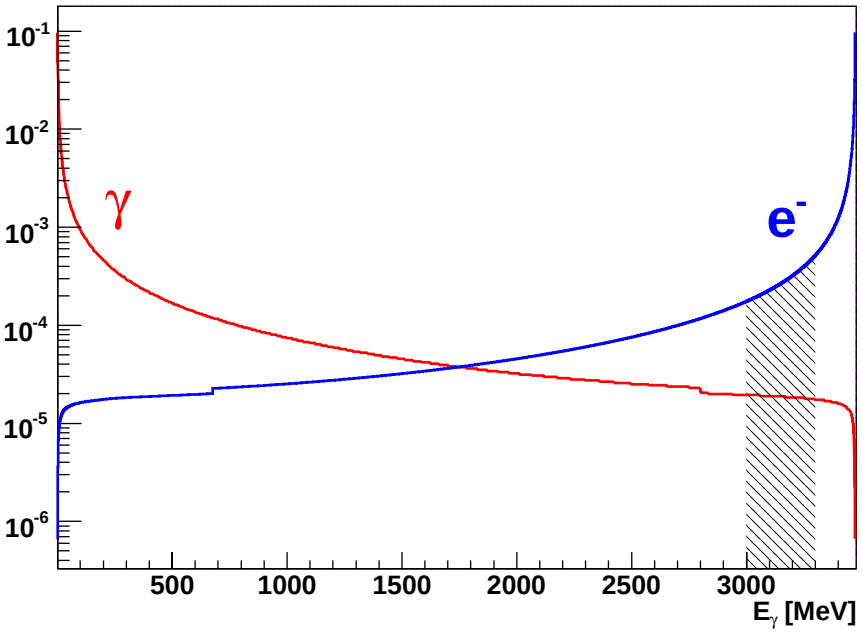

Figure 3.4: Bremsstrahlung spectrum (red) and corresponding electron spectrum(blue) for a radiator of thickness of 6.84% radiation lengths. The shaded region corresponds to the part of the spectrum observed by the experimental acceptance.

hall A has no instrumentation to remove the electrons after they have passed through a radiator. The electrons' incoming energy defines the "endpoint" of the energy regime, and it is clear from Fig. 3.4 that the ratio of photons/electrons is lowest at the endpoint. Since the experiment involves two-body kinematics, a particular combined setting of HRS and photon calorimeter defines a specific incident particle "window" of (E_{min}, E_{max}).The experimental demands, as discussed before, require a rather high photon/electron ratio, since the elastic $p(e, e'p)$ constitute a background and complicate the data analysis. This is the reason why our acceptance "window" has been set to lower energies – $E_\gamma \in (3000, 3300)$ for this particular plot – in order to increase the flux of the photons and reduce the number of background electrons. Obviously, this energy domain could be lowered even more, causing an even further increase of photon/electron ratio, however due to theoretical constraints the experiment needs to perform measurements at as high values of s Mandelstam variable as possible.

3.2.3 High Resolution Spectrometer

The highlight of Hall A standard instrumentation are the twin High Resolution Spectrometers(HRS). These devices are developed to have a moderate acceptance (about $6 \times 10^{-3} sRad$ and 9.5% momentum coverage), while achieving a very high momentum and angular resolutions. A list of HRS' acceptance and resolution parameters can be found in Table 3.1.

High Resolution Spectrometer consists of four magnetic elements: three superconducting quadrupoles, and one superconducting dipole, which performs the momentum selection of the spectrometer. The superconductive phase is accomplished by cooling magnets' niobium coils

Momentum	Range	$0.3 - 4.3 GeV/c$
	Acceptance	$\pm 4.5\%$
	Resolution	2.5×10^{-4}
Out of Plane Angle	Acceptance	$\pm 60 mR$
	Resolution	$2. mR$
In Plane Angle	Acceptance	$\pm 30 mR$
	Resolution	$0.8 mR$
Transverse Projection of Vertex	Acceptance	$\pm 5 cm$
	Resolution	$0.8 mm$

Table 3.1: Performance characteristics of Hall A's left HRS.

with liquid helium at a temperature of $4.5K$.These elements succeed each other in $Q_1 Q_2 D Q_3$ configuration, as can be seen in Fig. 3.5. Most of the focusing is accomplished by the system of the quadrupoles. The first Q_1 quadrupole focuses in the vertical plane and defocuses in horizontal plane, while Q_2 and Q_3 provide focusing in horizontal plane and defocusing in vertical plane. For a given value of central momentum setting, the current in the dipole is chosen based on output from a measurement device which measures nuclear magnetic resonance of a probe placed inside the dipole. The absolute magnetic field is calculated from resonance frequency to an extremely high accuracy. The fields inside the quadrupoles are monitored using Hall probes, which are used only for diagnostic purposed since they do not provide the same precision. Instead, the currents inside the quadrupoles are set based on pre-existing data on current-to-field relations. Due to ferromagnetic hysteresis, however, a given current may correspond to two different field values. In order to avoid this dichotomy,

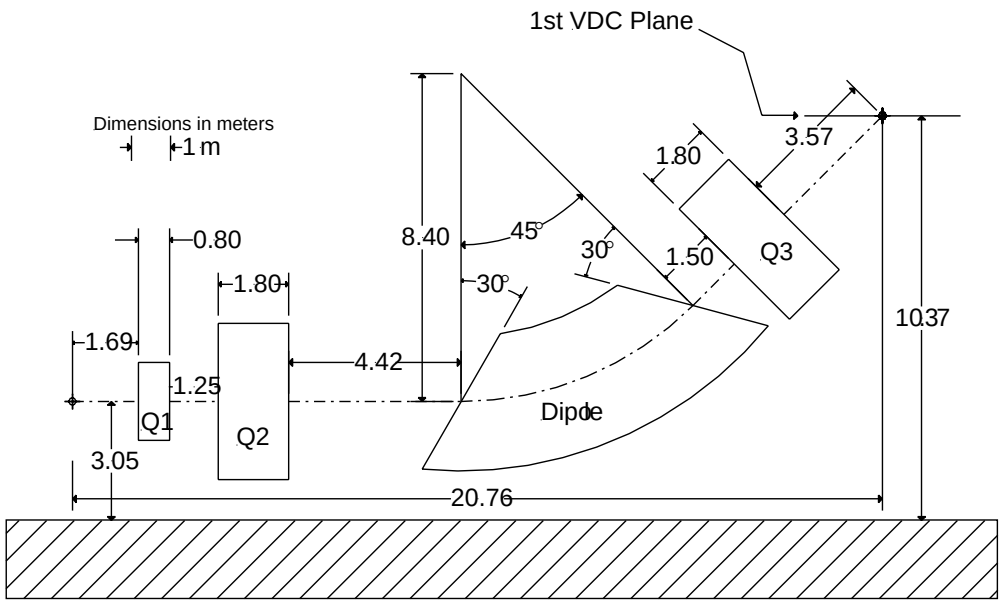

Figure 3.5: Schematic drawing of Hall A High Resolution Spectrometer's magnetic structure.

the magnetic fields inside the quadrupoles can be changed only in one direction, and in case of reversal the full cycle of hysteresis needs to be performed.

3.2.4 HRS Detector Package and Vertical Drift Chambers

The High Resolution Spectrometer's magnetic optics can be understood through an analogy to a photographic camera, with the difference that in addition to measuring the focal plane coordinate the HRS detector package also measures particle's vector of motion. If one were to know the optic properties of the spectrometer, then one could precisely calculate the values of kinematic variables at the reaction vertex. To perform this calculation, we first need to measure the particles coordinates at the focal plane with a very high accuracy. HRS standard detector package includes a pair of Vertical Drift Chambers(VDC), which are positioned after the last Q_3 quadrupole of the spectrometer. Each VDC measures the particles precise

position at its central plane, and from the two values of position one can calculate the particle momentum's angle with respect to the spectrometer's central axis. The detector package is located inside the "detector hut", a large chamber with heavy concrete walls to protect the detectors from large doses of radiation damage, as well as to reduce the rate of accidental coincidences during an experiment which uses other detectors in coincidence with HRS. The detector packages consists of an array of elements, some of which are listed below, in the order of being seen by the particle:

- Two succeeding Vertical Drift Chambers, used to track the particle's (proton, in our case) trajectory.
- A vertical scintillator plane used for event triggering in coincidence mode with the photon arm (see Sec. 3.5.1).
- A pair of "square" scintillator planes used for a "singles" trigger and time-of-flight measurements.
- An aerogel threshold Čerenkov counter, which detects the Čerenkov-Vavilov radiation from the heavier particles, and uses it as a particle type identification.
- A Focal Plane Polarimeter (FPP) for measuring the focal plane polarization of the particle stream. This, along with information on spectrometer's magnetic structure, can then be used to calculate the vertex polarization of the particle. The FPP is made of two sets of straw chambers for particle tracking, as well as two analyzer blocks used to introduce azimuthal asymmetry in particle's trajectory.

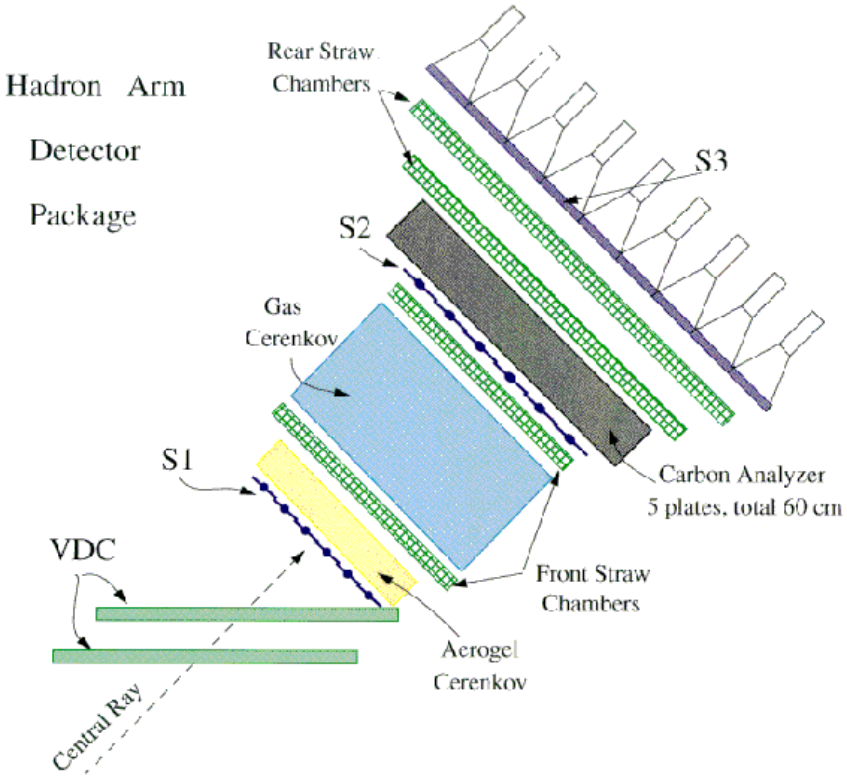

Figure 3.6: Schematic layout of Hall A beam setup and relative positioning of the two High Resolution Spectrometers.

A full view of the HRS detector package can be seen in Fig. 3.6.

As mentioned above, in order to reconstruct the kinematic variables at reaction vertex it's necessary to have a good "image" at the focal plane, in an analogy with photography. The focal plane variables are determined through the Vertical Drift Chambers [42], a function which makes the later probably the most important element of Hall A detector package.

The detectors are located after the third HRS quadrupole, and are oriented parallel to the Hall A floor and at 45^o to spectrometer's central axis. The VDC's are mounted on rails, which allows for their simple extraction from the detector hut for purposes of maintenance and diagnosis, and are aligned by an accuracy of $100\mu m$ with each other. A schematic view

of the detectors and of their alignment can be seen in Fig. 3.7. As can be seen in the lower

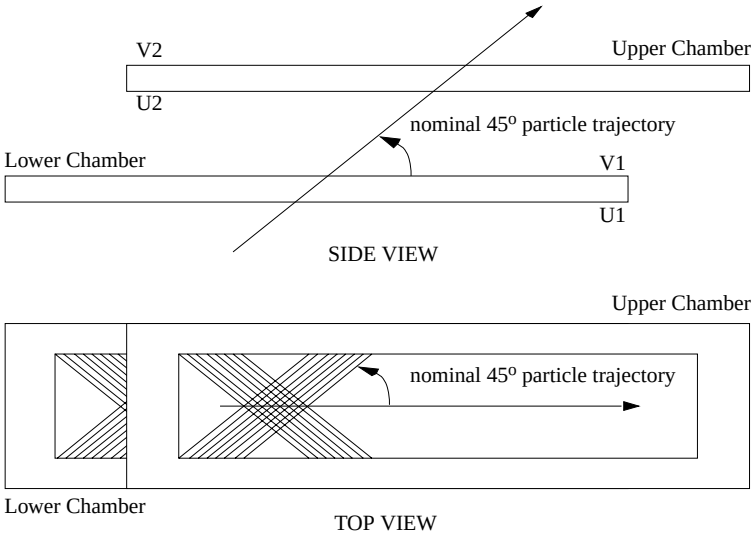

Figure 3.7: The Vertical Drift Chambers of High Resolution Spectrometer, and their relative positioning.

drawing, each chamber contains two planes of gold-plated tungsten wires. The total number of the wires is 368 and the relative angle of the wires to the central axis of the spectrometer is 45^o. The geometry dimensions of the chambers are the following: approximately $240cm$ long, $40cm$ wide and $10cm$ high, and the detection area of each chamber is $211.8 \times 28.8cm^2$. The voltage drop between each wire and the cathode plane is $4000V$. The cathode planes are made of gold-plated mylar, and are located between the wire planes. The gas which fills the area between the wires and the cathode is a mixture of argon and ethane at the ratio of $62 : 38$ [42].

The general principle behind the operation of drift chambers is somewhat similar to that of a Geiger counter. As a charged particle passes through the gas filling the gap between the cathode and the anode (the wire), it causes ionization of the gas atoms. The produced free electrons then experience the strong electric field which causes them to drift towards the

wire. While the distance of the electron to the wire is much greater than the wire radius, it experiences only a constant electric field, and its velocity quickly reaches a constant value. However, when the electron approaches the wire it experiences a strongly non-uniform field. This causes it to accelerate, and as a result the electron ionizes other gas atoms and causes an avalanche. When the avalanche reaches the wire it triggers a strong electric pulse, which is then amplified by the pre-amplifier/discriminator card. The output of the card is then sent to and processed by a LeCroy Fastbus 1877 Time-to-Digital Converter (TDC), which digitizes the signal and sends it to trigger electronics. Using known values of electron drift velocity in the gas, and having the time of drift as a data, one can later calculate the exact position where the ionization occurred. Combining this information from different wires, a hit coordinate can then be calculate with a very high precision. The resulting coordinate and angular resolutions are $100\mu m$ and $0.5mR$.

3.3 Photon Spectrometer

The detection of the photon from Compton scattering on proton is performed by the photon spectrometer. The spectrometer has been developed, designed and built by the E99-114 collaboration specifically for this experiment. The key constraint behind the design of the photon spectrometer was the demand for high coordinate and medium energy resolutions. These characteristics are critical in order to distinguish Compton scattering events from the pion decay background and elastic electron scattering $p(e, e'p)$ events. The high position resolution was achieved by building a highly segmented hodoscope array of lead glass blocks. This segmentation also insured relatively low counting loads on the photo-multiplier tubes.

The spectrometer's structure consisted of the electromagnetic calorimeter, a deflection dipole magnet, and an electron veto detector. The later unit was used only for a very few runs, because its extremely high counting rates caused unacceptably large electronic deadtimes.

3.3.1 Electromagnetic Calorimeter

As mentioned previously, the primary process of electrons' interaction with matter is bremsstrahlung radiation: as the electron is accelerated by the field of a nucleus, it emits a photon. The photon's mechanism of interaction with nuclei is through electron-positron pair production. The diagrams for the two processes can be seen in Fig. 3.8. When a photon enters the matter,

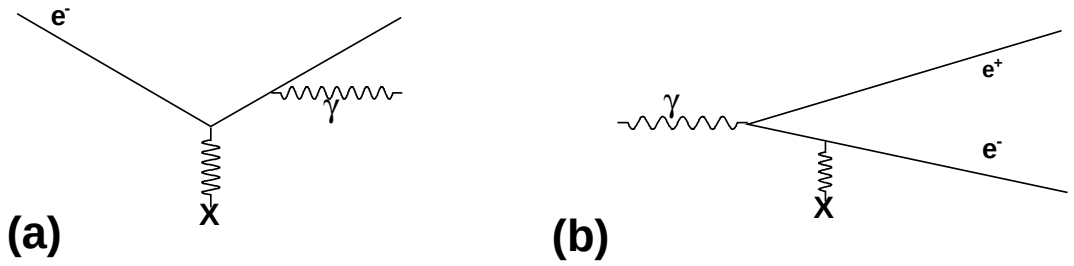

Figure 3.8: Feynman diagrams for a) Electron Bremsstrahlung b) pair production. During an electromagnetic shower the radiated photon of (a) becomes the pair-producing photon of (b).

it causes a pair production, as shown in Fig. 3.8(b). The outcoming electron and positron have energy distributions which are peaked at $E_\gamma/2$. The electron then can interact with the nuclei of the matter, radiating a photon, as in Fig. 3.8(a). The photon of this process then can become the initiator of another pair production. This process can go on repeatedly, similar to an avalanche, generating an electromagnetic shower, until the energy of the particles is below some threshold value, at which point pair production becomes impossible. The

above described process can also be initiated by an incoming electron. The devices which are able to fully absorb the energy of the shower are called, in an analogy with thermodynamics, electromagnetic calorimeters.

The characteristic depth of the electromagnetic shower is determined by two parameters. One is the radiation length, which determines the mean depth of each generation. The other parameter is the energy at which energy loss by ionization becomes predominant. This energy is essentially the threshold at which the shower stops progressing. During pair production the average energy of the produced leptons is half of incoming photon energy, therefore at each generation the energy of every given particle is halved in average. After n generations the mean expected energy of a given particle will be approximately $E_0/2^n$. If the threshold energy is equal to ϵ_0, then the shower will stop when the energy of the particle is equal to ϵ_0, that is, when

$$\frac{E_0}{2^n} = \epsilon_0 \quad \text{and correspondingly} \quad n = \log_2 \frac{E_0}{\epsilon_0} \tag{3.1}$$

If the radiation length of the material is equal to X_0, then the depth of shower will be equal to $d = n \cdot X_0 = X_0 \cdot \log_2(E_0/\epsilon_0)$. Since the radiated photons and pair-produced leptons are emitted mostly parallel to the original particle, the transverse development of the shower is primarily conditioned by multiple Coulomb scattering of the electrons and protons in the material.

The measurement of the shower energy is done by detecting the Čerenkov-Vavilov radiation from the highly energetic electrons. For this, a material needs to be chosen so that its index of refraction implies a speed of light always less than the speed of the electrons with energy ϵ_0. On the other hand, to reduce the depth of the shower d a material with

Density	$3.86 g/cm^3$
Index of Refraction	1.65
Radiation Length X_0	$2.5 cm$
Critical energy ϵ_0	$15 MeV$

Table 3.2: Electromagnetic and optic characteristics of TF-1 lead glass.

a small radiation length X_0 needs to be chosen. The choice of material for the calorimeter needs to be withing these constraints. The calorimeter needs to be built from a very heavy material – preferably lead itself – with a high index of refraction. It however needs to be also transparent, in order for the Čerenkov radiation to reach the photo-cathode of the photo-multiplier tube (PMT). The obvious choice which satisfies these requirements is lead-glass. The physical properties of TF-1 lead glass can be seen in Table. 3.2. Using the values from the table and Eq. 3.1 we can determine the depth of the shower: $d = 20 cm$. The depth of the calorimeter itself is $40 cm$.

The RCS total absorption electromagnetic calorimeter was designed and built by a group of researchers and technicians from Yerevan Physics Institute (YerPhI). The calorimeter consist of 705 lead-glass blocks, with FEU-84/3 photo-multiplier tubes connected to the rear of the blocks. The connection is optically transparent. The lead glass blocks are wrapped in optically-opaque material made of aluminised Mylar film and black Tedlar – in order to allow for identification of the block which was hit by the original particle – and are arranged in an array 32 rows high and 22 columns wide. Each block has a rectangular cross section with a side of $4 cm$, and a length of $40 cm$. The matrix of the lead-glass blocks is shielded

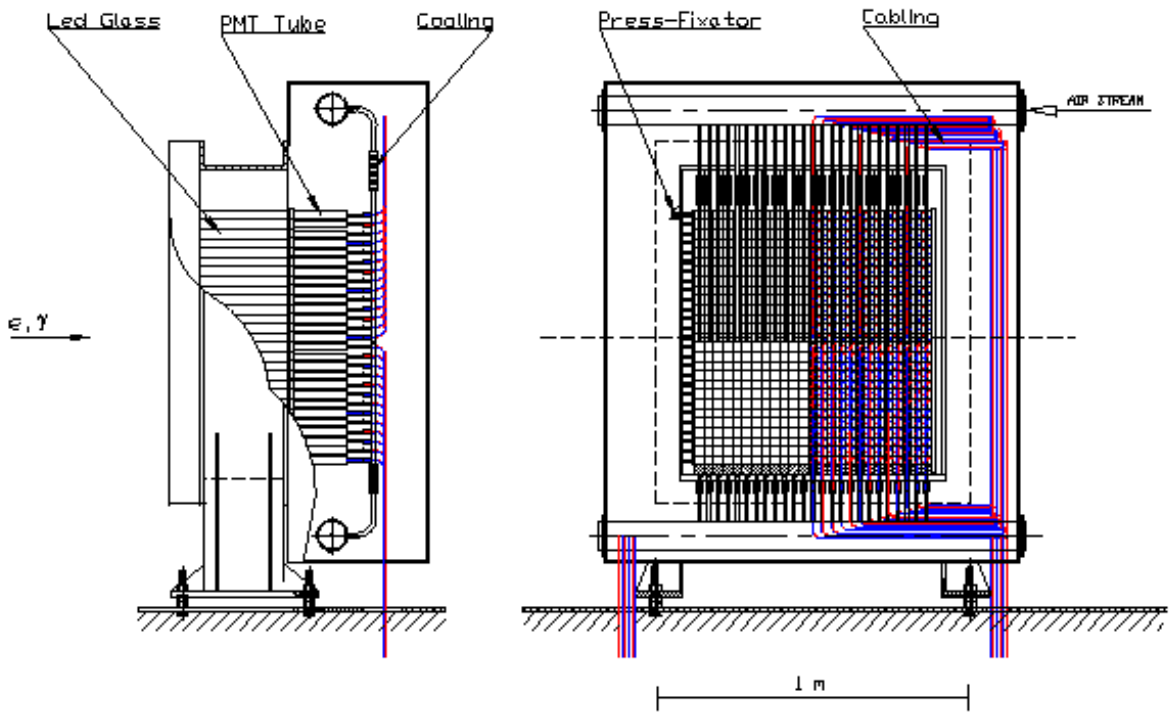

Figure 3.9: Drawing of RCS electromagnetic calorimeter, showing its internal structure.

inside a light-proof containment vessel, with doors at the rear for easy access in case of repair needs. The PMT were connected to the lead-glass blocks by using springs to apply pressure against the lead-glass surface , and optical grease was applied at the contact point to insure a good optical coupling. A drawing of the calorimeter can be seen in Fig. 3.9.

As mentioned earlier, the Čerenkov light emitted by the electrons is registered by the photo-multiplier tubes (PMT). PMT's are one of the most frequently used tools in medium and high energy physics. The principle behind a PMT's operation is the photo-electric effect. As the photons enter the PMT, they hit a metallic surface called photo-cathode. If the photon's energy is high enough it transfers its energy to an electron in the metal. If that energy is higher than the energy binding the electron to the metallic lattice, then the electron becomes free and is then accelerated by strong electric field of the first dynode. Once the

electron reaches the dynode, it strikes free new electrons, which are then accelerated towards the second dynode. This process is repeated about ten times, producing a large amplification of the original signal. For this process to be effective, the voltage between the dynodes has to be somewhat large. The total voltage applied between the last anode and the photo-cathode was $1600V$. The whole assembly of cathodes, dynodes and anode is kept in vacuum inside the tube. The collected electric signal is then sent to an electronic trigger logic and a Fastbus 1881 Analog-to-Digital Converter (ADC), which digitizes the accumulated charge and sends the result to data acquisition.

Due to minute differences in their construction, for the same amount of incoming light and for the same applied voltage different PMT's will give different signals. Since the final goal of this measurement is to determine the energy deposited in the calorimeter, it is necessary to calibrate the voltages, using a standard source of light emission, which will allow one to change the voltages of the PMT in order to achieve the same signal. This is called gain monitoring system. To expose different blocks to the same light amount, ultraviolet light from a nitrogen laser is used. The laser light has been incident on a plastic scintillator, which worked as a wavelength shifter. The scintillator eliminates the directionality of the light, and its output is sent by optical fibers to a plastic Lucite surface, which is placed immediately in front of the array of lead-glass blocks. In this manner, all the blocks are illuminated by the same intensity of light, allowing for an automated system to change the voltages applied to the PMT's in order to achieve the same signal. The automation has been performed by a Java control software, whose output has been sent to the LeCroy-1458 high voltage supply.

The support structure of the calorimeter was built from steel, and housed a number

of support units: the calorimeter array, the front-end electronics, cabling to and from the electronics, a forced air cooling system for the PMT's, gain monitoring system and the laser. The whole structure was built in a self-contained manner, in order to simplify the frequent task of moving the calorimeter from one kinematic point to another. To accelerate this procedure and to increase mobility, the system of more than two thousand cables which travelled from and to the rear of the calorimeter was placed on a train of wheeled carts. There has also been a need to develop a system which would allow the quick and simple alignment of the calorimeter with its kinematic position. To do this, the Hall A floor has been painted with a map of color coded dots – every degree angle, and every half meter, with the actual positions marked in paint. Furthermore, two "light pointer" tools, consisting of an aluminum tube with a incandescent light attached at the back, were attached to the support frame, in such a manner as to be aligned with calorimeter's axis. One of the lights was placed $0.5m$ in front, and other $3m$ behind the calorimeter face. During the move, the calorimeter was placed in such a way as to align the light spots with the dots on the floor. As a result the process of fine alignment took less than one minute. Only a moderate accuracy (within $2cm$) was necessary, since the misalignment of the calorimeter could later be precisely calculated using elastic scattering data and two-body kinematics of that reaction.

3.3.2 Electron "veto" Detector and Dipole Magnet

Elastic $p(e, e'p)$ electron scattering is one of the backgrounds which complicate the identification of the Compton scattering events. This is due to the constraint that in order to achieve high luminosities the acceptance's energetic window had to be close to the endpoint,

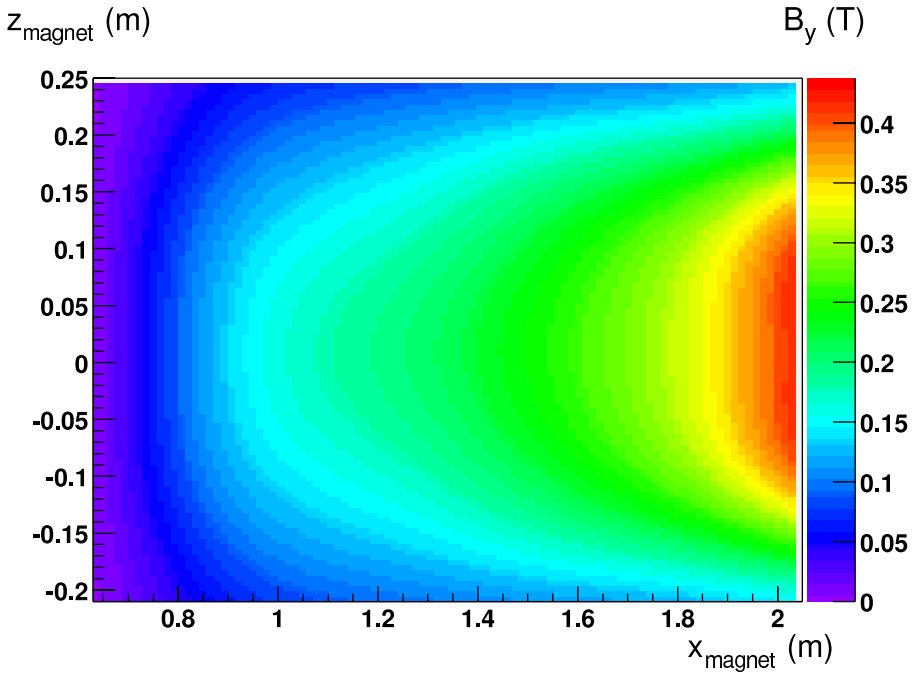

Figure 3.10: A numerical calculation of the component of the magnetic field perpendicular to particle's trajectory as a function of lateral(x_{magnet}, the abscissa) and longitudinal(z_{magnet}, the ordinate) coordinates. x_{magnet} is increasing toward decreasing scattering angles.

making the electron-photon beam unavoidable. From point of view of two-body kinematics, the electrons are completely indistinguishable from the photons due to their negligible mass. While the electromagnetic shower development is slightly different for electrons and photons, the calorimeter's resolution wouldn't allow one to make that distinction. The only other way to distinguish the electron events from the photon events would be to either place an electron *veto* detector in front of the calorimeter – allowing it to detect the Čerenkov light from the electrons in lucite – or to place a dipole magnet after the target, which would offset the two-body kinematic correlation between the recoil proton and the electron, thus allowing the separation of the electrons from the unaffected photons. The idea behind the use of magnet is based on kinematic correlations between the two arms of the experiment.

One can use the proton's kinematic variables and two-body kinematics to reconstruct the photon's or electron's scattering angle. If no deflections are present , the difference between the calculated value and actual measurement should be centered around zero (the width of its distribution entirely conditioned by resolution and multiple scattering effects). Thus, when viewing the kinematic correlation between the two arms, the electrons and photons would be superimposed. However, if a strong magnetic field were to be introduced immediately after the target, it would offset the correlation of the electrons, separating them from the Compton events. It was decided that a deflection of $10cm$ on calorimeter face when the calorimeter is at the distance of $5.2m$ away from the target would be sufficient to guarantee the separation. A numerical calculation of the field of the RCS dipole magnet [43] can be seen in Fig. 3.10. The magnetic field allowed for a $\gamma p/ep$ separation at all the kinematic points. What can be seen in the figure, and what is very important, is that the field is increasing with decreasing scattering angles: the electrons scattered at smaller angles have larger energies and need a larger field for the same amount of deflection.

One way to determine the field of the RCS Magnet is by using numerical calculations, the result of which can be seen in Fig. 3.10. Another manner is to simply observe elastic electron scattering, and determine the field integral $\int \mathbf{B} \cdot \mathbf{dl}$ by measuring electron deflection. This analysis has been performed for a number of kinematic points, for a setting when the current of the magnet was $500A$ and a setting where it was $600A$. The resulting dependence has been fitted using a polynomial expression [44]. The results for both current settings can be seen in Fig. 3.11.

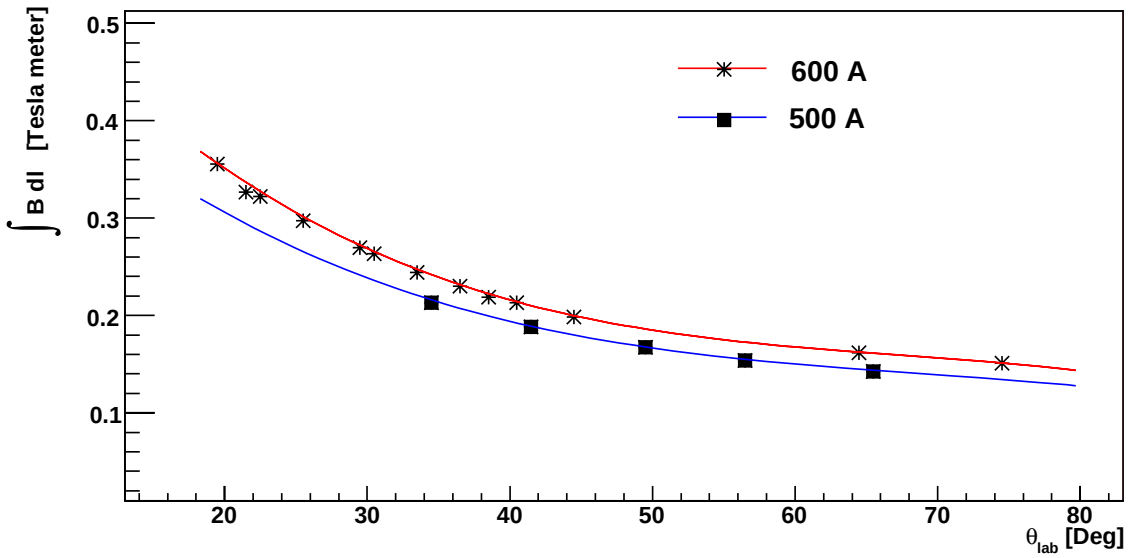

Figure 3.11: A plot of $\int \mathbf{B} \cdot \mathbf{dl}$ versus scattering angle. The two sets of data, as fitted with two different lines, correspond to the current settings of 600 A (red line) and 500 A (blue line)

3.4 Hall A Focal Plane Polarimeter

The measurements of Compton scattering polarization transfer asymmetry are an important part of the E99-114 experiment, as already discussed in Chapter 2. The task of determining the polarization of recoiled protons at the target requires a measurement of polarization at the focal plane of the spectrometer, as well as a good understanding of the precession of proton spin in the magnetic fields of spectrometer's magnetic elements. The Focal Plane Polarimeter (FPP) is the Hall A detector used for measuring particle polarization at focal plane by means of detecting the angular effects of secondary nuclear interaction in two analyzers. [45].

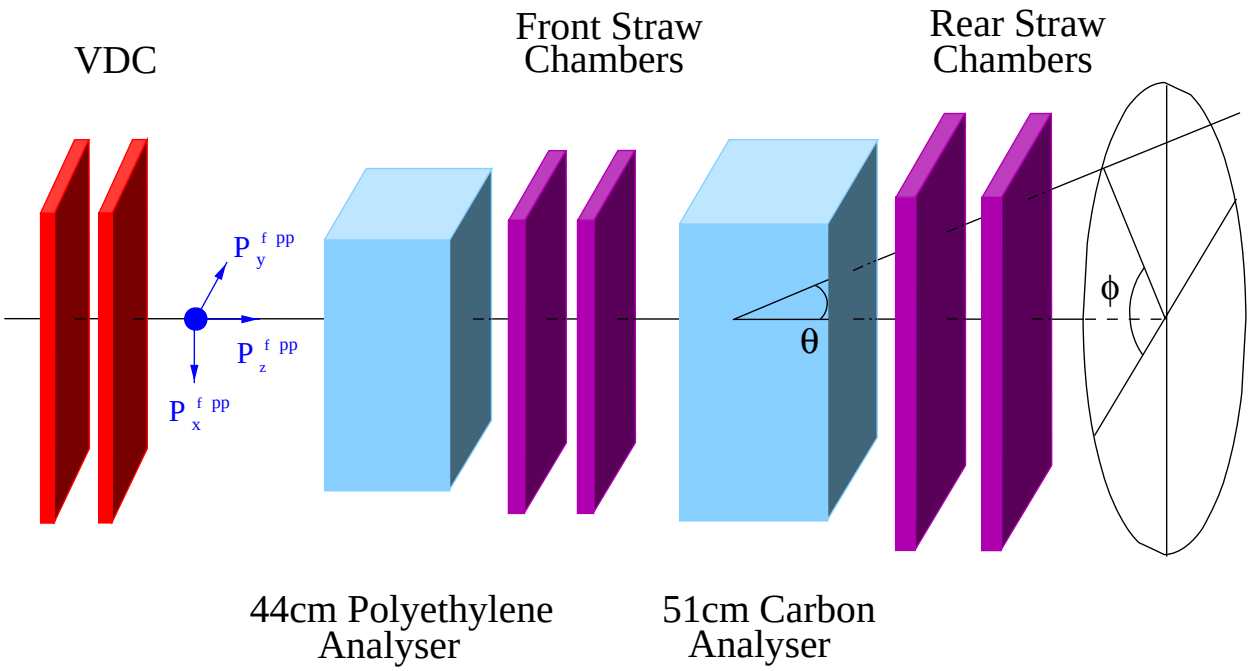

Figure 3.12: The dual analyzer configuration of Hall A Focal Plane Polarimeter (FPP).

3.4.1 Proton Polarimetry

As the proton scatters from a nucleus, its spin interacts with its induced orbital angular momentum. This spin-orbit coupling results in a sensitivity of the final scattering direction on the spin of the incoming proton. If one observes a large set of incoming protons whose spins are preferentially pointing in a given direction, then one will observe an azimuthal asymmetry in the scattering angle. By measuring this asymmetry it is possible to determine the polarization of the incoming protons. For example, in case if there is no preferred direction of the incoming proton spins, the azimuthal component of the scattering angle will be perfectly uniform in its distribution. In general a polarimeter is constructed of two sets of tracking detectors (such as VDC's and/or straw chambers), whose purpose is the determination of the particles' initial and final directions, and an analyzer scattering material (such as carbon or polyethylene) in between. A schematic diagram of the Hall A

FPP configuration can be seen in Fig. 3.12, showing a second analyzer and a third set of detectors, which are added to increase the analyzing efficiency of the apparatus. A detailed description of the technique of secondary scattering for particle polarimetry can be found in Ref. [46], [47] and [48].

The Hall A FPP has been developed and built by Hall A collaboration, and has been used in a number of experiments to extract information on proton polarization. The standard configuration, before the E99-114 experiment, consisted of one 51 cm-thick carbon analyzer and one set of straw chambers, to track the proton after it passed through the analyzer. The E99-114 experiment however saw the use of a second analyzer-detector package, with the addition of a 44 cm-thick polyethylene(CH_2) analyzer, which greatly increased the analyzing power of the polarimeter. The overall effectiveness of the FPP as a tool is described by a quantity known as the Figure-Of-Merit (FOM), which is a combination of the efficiency and analyzing power of the material. The efficiency is simply related to the quantity of material that the proton has to traverse. The analyzing power describes the intrinsic properties of the material, such as the induced spin-orbit coupling.

The variable nature of the analyzing power for a given material can be of a serious concern when choosing a material for the analyzer. The carbon analyzer of the FPP consists of blocks of high purity graphite. The experimental data has shown that the FOM for carbon drops significantly as proton momenta exceed 2.4 GeV/c. Hence other alternatives had to be considered to compensate for this drop in performance. The polyethylene was first introduced as the sole analyzer for FPP during a double polarization measurement of the proton form factors [49]. With proton momenta in the $2.6 - 3.8$ GeV/c range, a significant improvement

in the FOM was achieved, as compared to previous measurements with carbon [23].

It was therefore naturally concluded that a polarization measurement should optimally involve both carbon and polyethylene analyzers. A minor re-arrangement of the existing tracking apparatus resulted in the configuration of Fig. 3.12, where the proton can scatter either or both on carbon and polyethylene analyzers, and precise data on its trajectories can be obtained from the VDC's and straw chambers in order to reconstruct the azimuthal asymmetry, which then can be used in determining the total polarization of the incoming proton flux.

3.5 Data Acquisition and RCS Trigger

After the experimental hardware detects a signal, its amplitude and timing are processed and digitized by different front-end electronic ADC and TDC modules, whose signal is then sent to Hall A Data Acquisition (DAQ) system. This system is made of a variety of CAMAC, Fastbus and VME electronic units, in addition to which it also contains electronic modules developed and built by Hall A electronics group. The software processing of data is implemented by using the data acquisition software package CODA – CEBAF On-line Data Acquisition [50].

The DAQ system for the hadron arm and for the beamline monitoring apparati was essentially unchanged for our experiment, as it is part of standard Hall A instrumentation. However, the calorimeter, built and developed by the RCS collaboration, needed a separate system of readout package. Also, given the specifics of electronic support for the

calorimeter, a new type of coincidence trigger scheme had to be developed for the combined HRS-calorimeter system. While the readout package for left HRS is located in the shielding hut, which also houses the focal plane detector package, the electronics for calorimeter were placed on the left side of Hall A floor. To protect the micro-electronics from radiation damage – which can be extensive due to very high radiation levels during runtime – a heavy concrete wall was constructed to block radiation.

3.5.1 Trigger Configuration

Since the calorimeter unlike the HRS detector package is not protected from the massive volumes of radiation , it needs a very flexible trigger which can be both highly discriminative – to reject the vast amounts low energy background – and redundant at the same time in order not to reject true hits. The 704 calorimeter blocks are grouped in sets of 8 adjacent blocks, in 2×4 sub-arrays. The signals of the blocks of a given sub-array are summed in a linear summing module, giving a sum_8 signal. This signal however cannot be used for trigger: it is quite likely that the electromagnetic shower will start at the intersection of 4 sum_8 sub-arrays, and the maximum energy registered by the trigger electronics will be only the fourth of the total energy, causing it to reject the hit as a background. Hence, another summing scheme needs to be invented to allow for such a redundant summing as to insure that a shower, no matter where it is produced, will be entirely contained by a particular single sum. To do this, the sum_8 signals are further summed in groups of 4, giving sum_{32} arrays. However, this summing is performed inclusively, and every sum_8 is contained by four sum_{32} arrays, as can be seen in Fig. 3.13. As an input to the discriminator all the 56 resulting

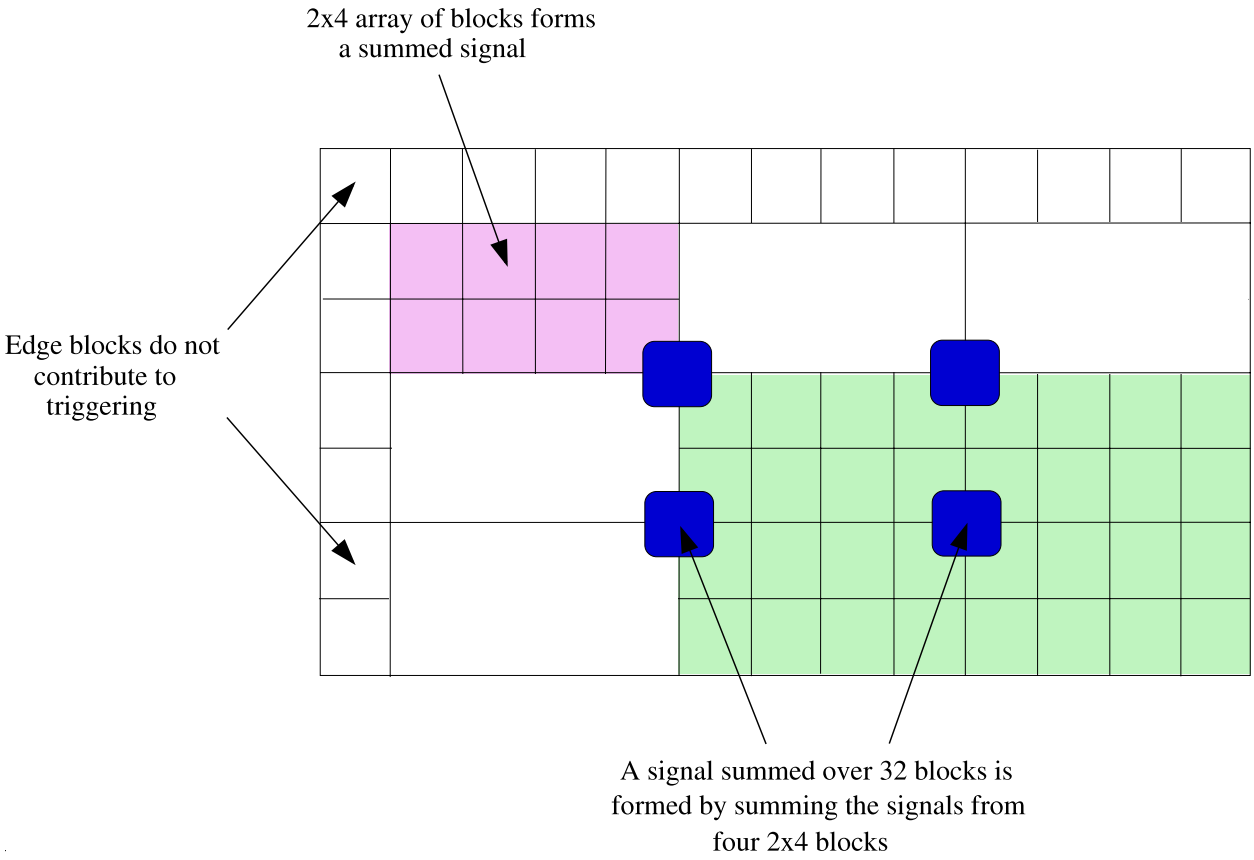

Figure 3.13: The photon trigger consists of the OR of the overlapping sum_{32} arrays, a configuration which makes sure that a given electromagnetic shower is entirely contained by at least one summing unit.

sum_{32} are compared to a threshold voltage, and an OR logical operation is performed on the result. This results in a photon single trigger, labeled in the data stream as T1.

Traditionally, hadron singles triggering in HRS is performed using two sets(S1 and S2) of scintillator paddles, whose coincidence defines the "single" trigger for the hadron arm. Each detector consists of a set of five scintillator paddles, each of which has two PMT's on each end. An electronic operation based on such a complex system of signals is somewhat complex and rather slow, in terms of electronic time, in a situation where it is important that the hadron signal is the first to arrive in order to open the electronic "gate"[1]. For this reason another scintillator, labeled S0, with only two PMT's, was used for the coincidence trigger. The scintillating material, while rather useless for coordinate reconstruction, is ideal for triggering purposes, since it allows for a very fast and highly efficient signal[2]. The S0 scintillator detector consists of a $10mm$-thick scintillator paddle, with two PMT's attached to the opposite ends. The logical AND of the two signals defines a trigger, T7. The logical of T7 AND T1 defines the coincidence trigger, labeled as T5 in the data stream.

The full schematic drawing of the trigger logic can be seen in Fig. 3.14, showing the T1 and T7 triggers separately. Since the T1 trigger works by opening an electronic gate of a limited time duration, it is important to insure that in case of a coincidence event the T7 trigger arrives within that time window, which is as short as $100ns$. However, due to different distances the times of flights for the hadrons and photons are different. This discrepancy is

[1]It would also have been possible to choose the calorimeter single trigger as the opener of the gate, however, due to calorimeters exposure to radiation, this would involve a huge amount of noise-based triggers, affecting the electronic dead time in a highly negative manner

[2]The S0 efficiency has been estimated to be more than 99.5%

resolved by introducing artificial electronic delays to the signals, to insure that in case of an actual coincidence event a coincidence trigger is in fact produced.

3.5.2 Data Acquisition System

During an event, the results are recorded in the raw data, in a format which only contains the raw values of TDC and ADC for thousands of detector channels. Later stages of physical analysis will use this information, as well as known detector geometries and positions, in order to compute actual physical values such as momentum, angles, and coordinates. The read-out of these ADC and TDC values and their writing into the data stream is controlled by a CODA-based system which has been configured for this particular experiment. As mentioned earlier, the digitization of the analog signals are performed by ADC and TDC modules, which were located in four Fastbus crates. These crate was controlled by a computer with a Fastbus interface called a Read-Out Controller (ROC). The photon arm electronics contained the VME crate which constituted the Trigger Supervisor(TS) and Event Builder modules. The Trigger Supervisor is a VME board specially developed by the JLab electronics group and controlled by a Motorola MVME 2400 unit. It can be used to program up to twelve different triggers, with a pre-scaler value applied to each one of them. The system of pre-scalers allows one to randomly reject not-so-crucial data – in order to save disk space and computational time – and keep the important data type. For example, in our case the Trigger 5 coincidence events were the most important, and a pre-scaler of 1(meaning every single event was recorded and stored) was applied on them. Other event types, corresponding to T1 and T7, were less important for future physical analysis, and a large pre-scaler values

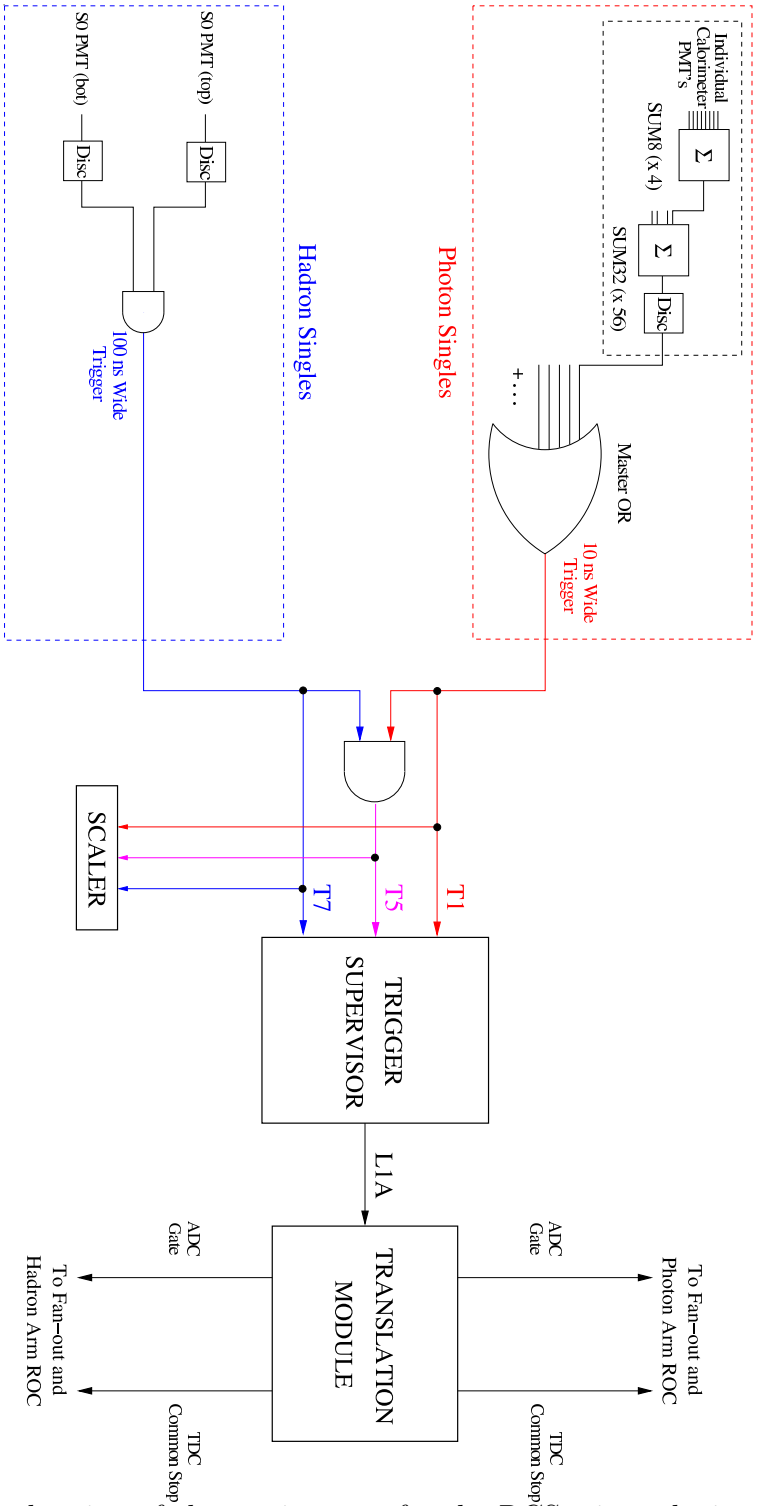

Figure 3.14: The drawing of electronic setup for the RCS trigger logic.

of order 1000 were applied to them, allowing us to keep only every 1000th event of that type.

When the trigger supervisor receives a trigger, it outputs a Level 1 Accept (L1A) signal to all ROC's, which then provide gates to all the ADC modules (allowing them to register the event's ADC values) and a common stop to all the TDC. When all the modules are finished recording and communicating the front-end data, a busy flag is turned off in the Fastbus crate and ROC informs TS that it is ready for the next event. In this manner a TDC hit in a detector starts the counting of time for that channel, and records it only if a trigger has been achieved. Otherwise, if a trigger signal has not been received, the timing reaches a threshold and the information is abandoned. The TDC's essentially calculate the time between a hit and a common finish command, from which the relative timing of every channel can later be deduced. The Fastbus 1877 TDC modules used have 96 channels, have a timing resolution of $1ns$ and are able to record multihit events. The Fastbus 1881 ADC modules have 64 channels with individual thresholds which can be set remotely. The function of the ADC's is to calculate and digitize the total accumulated charge from a signal pulse.

Chapter 4

Data Analysis: Data Reduction, and Preliminary Analysis

The data analysis of RCS experiment in many ways reflects the unique character of the experiment and the instrumentation involved. The analysis can be divided into two sections: data reduction, when raw ADC and TDC channel values are processed into more meaningful kinematic variables, such as scattering momentum, angle, and vertex position; use of the resulting "processed" data to extract Real Compton Scattering cross sections with the use of a Monte Carlo simulation package. This chapter will discuss the first part of the analysis – data reduction and extraction of proton and photon energies and scattering angles.

4.1 The General Flow of Analysis

The main bulk of data reduction is performed using three stand-alone packages: *espace* (Event Scanning Program for hall A Collaboration Experiments) [51], *RCS analyzer* and

merge. The first package performs the analysis of the hadron arm – analysis of VDC track information and reconstruction of the hadron kinematic variables at the target. The second package performs the analysis for the photon arm – determination of the calorimeter hit position and particle energy. Finally, the *merge* code merges the two data streams into a single one, at the same time calculating different "derivative" variables – such as incident particle energy and kinematic correlations between the recoil and scattered particles.

The data reduction and physical analysis can be broken into separate stages:

- Decoding of raw CODA data, and extracting ADC and TDC values for the more than 2000 channels.
- Use of calibration coefficients to convert the ADC and TDC values into information on absolute amplitude and timing of the signal.
- For the hadron arm, use the above data to reconstruct VDC hit positions, and from there determine the focal plane kinematic variables. For the photon arm, use center of mass algorithms and calibration constants to determine hit coordinate and energy of the electromagnetic shower.
- Determine proton's kinematic variables at the target using its focal plane variables and transformation tensors for the spectrometer's magnetic optics.

The next stages of the analysis consists of event separation, described later in this chapter, and Monte Carlo fits to the data, as described in the next chapter. By having measured the full extent of kinematic variables for an event, we can use a combination of kinematic correlations and trigger information in order to determine the probable origin of every event.

4.2 Proton Data

As mentioned before, the analysis of the proton data is performed using *espace* software package, which is written in ABSOFT Fortran [52], and uses standard data analysis CERN-LIB [53] libraries. The package decodes the raw CODA data , and uses timing information in order to reconstruct the hit position on a given Vertical Drift Chamber (VDC) plane, of which there are two. This in turn allows not only for the determination of focal plane coordinates, but also for the calculation of focal plane trajectory angles. In the next stage, *espace* uses optics transfer matrices in order to reconstruct proton's kinematic variables at the vertex in the target. These are the variables that are of a primary use in our data analysis.

4.2.1 HRS Vertical Drift Chambers

The Hall A left High Resolution Spectrometer (HRS) uses two Vertical Drift Chambers (VDC) in order to build the magneto-optic "image" of the vertex in the focal plane of the spectrometer. The function of a VDC is to track a particular event, and provide information which then can be used to fully determine that event's coordinate and vector of motion. As described in the previous chapter, the VDC's consists of an array of very thin tungsten wires subjected to the voltage of 4000V. The whole array is immersed in a mixture of argon and ethane gases [42].

When a charged particle traverses the detector, it causes ionization of the gas. The "droplets" of ionized gas experience the electrostatic attraction of the electric field, and

start drifting (hence the name) towards the wires. By measuring the relative time it took a centers of ionization to reach different neighboring wires one can reconstruct the position and angle at which the track traversed the detector. While the reconstruction of position can be quite precise, uncertainty in trajectory angle can be quite high, and depends strongly on a particular method of calculation employed. To eliminate this uncertainty, the VDC's are always used in pairs, and only position information from each VDC is used. By coupling the hit positions on the two VDC planes one can also calculate the angle of the trajectory, in two dimensions. At this point a full kinematic description of a track has been achieved, its values denoted as an array (U, V, η_U, η_V), where the first two parameters are the hit positions on the first detector, relative to a reference wire, and the last two variables are the trajectory angles relative to the normal of the detector plane.

The final stage of detector plane operations is the use of VDC geometry and positioning information in order to translate the above VDC coordinates into a more "universal" spectrometer variables. The Transport Coordinate System of the HRS is a system which is attached to the central trajectory of the spectrometer, with $\hat{z}$ axis pointing along the trajectory, while $\hat{y}$ pointing horizontally, away from the beam-line.

4.2.2 Spectrometer's Magnetic Optics

At any point inside the spectrometer a particle trajectory can be defined relative to the reference central trajectory by a vector of the following form:

$$\begin{pmatrix} x \\ \theta \\ y \\ \phi \end{pmatrix}$$

Here x and $\theta \equiv dx/dz$ are the trajectory's coordinate and angle in the vertical plane, while y and $\phi \equiv dy/dz$ are the trajectory coordinates in the horizontal plane.

If one were to treat the spectrometer optics as that of a perfect thin lens (*i.e.* no second order aberrations), one could achieve the following transformation between focal plane (fp) coordinate system to the target(tg) coordinate system:

$$\begin{bmatrix} \delta \\ \theta \\ y \\ \phi \end{bmatrix}_{tg} = \begin{bmatrix} \langle\delta|x\rangle & \langle\delta|\theta\rangle & 0 & 0 \\ \langle\theta|x\rangle & \langle\theta|\theta\rangle & 0 & 0 \\ 0 & 0 & \langle y|y\rangle & \langle y|\phi\rangle \\ 0 & 0 & \langle\phi|y\rangle & \langle\phi|\phi\rangle \end{bmatrix} \begin{bmatrix} x \\ \theta \\ y \\ \phi \end{bmatrix}_{fp} \tag{4.1}$$

In the first array $\delta \equiv (p - p_{central})/p_{central}$ is the relative momentum. Notice that it is impossible to independently determine both vertical position x_{tg} and momentum at the target. The vertical position however can be easily determined using y_{tg} and Beam Positioning Monitor information. Also, notice the zero's in the matrix: these arise from the assumption that the magnetic elements of the spectrometer are perfectly aligned in the horizontal plane, and the

magnetic features of the vertical plane do not affect the optical properties of the horizontal plane.

In practice, however, the HRS magnetic system is everything but a thin lens: the sextupole corrections of the quadrupoles amount to large non-linear aberrative effects, and these need to be taken into account when performing optic reconstructions, in order to achieve the highest possible angular and coordinate resolution. A more complete description of the transformation above is presented through tensor notation:

$$\begin{aligned} y_{tg} &= \sum_{i,j,k,l} Y_{ijkl} x^i_{fp} y^j_{fp} \theta^k_{fp} \phi^l_{fp} \\ \theta_{tg} &= \sum_{i,j,k,l} T_{ijkl} x^i_{fp} y^j_{fp} \theta^k_{fp} \phi^l_{fp} \\ \phi_{tg} &= \sum_{i,j,k,l} P_{ijkl} x^i_{fp} y^j_{fp} \theta^k_{fp} \phi^l_{fp} \\ \delta &= \sum_{i,j,k,l} D_{ijkl} x^i_{fp} y^j_{fp} \theta^k_{fp} \phi^l_{fp} \end{aligned} \tag{4.2}$$

where Y,T,P,D are the optics tensor elements. The mid-plane symmetry of the spectrometer requires that – just like in the linear case – for $k+l$ being even $Y_{ijkl} = P_{ijkl} = 0$ and for $k+l$ being odd $D_{ijkl} = T_{ijkl} = 0$.

Optics Calibration

Determining the optics tensor elements is a necessary task in order to achieve an optimal angular and vertex resolution for HRS. A method to achieve this has been developed by different members of Hall A collaboration [54]. The general idea behind the method is to somehow fix the values of the target variables y_{tg}, θ_{tb}, ϕ_{tg} and δ and observe how well

the optics tensor reconstructs those variables. The calibration is achieved my varying the tensor elements as to minimize the errors of the reconstruction using chi-square minimization method. The errors, or aberration functions, are defined as the following:

$$\Delta y = \sum_s \left[\sum_{i,j,k,l} Y_{ijkl} x^i_{fp} y^j_{fp} \theta^k_{fp} \phi^l_{fp} - y^0_{tg} \right]^2 \quad (4.3)$$

$$\Delta(\phi,\theta) = \sum_s \left\{ \left[\sum_{i,j,k,l} P_{ijkl} x^i_{fp} y^j_{fp} \theta^k_{fp} \phi^l_{fp} - \phi^0_{tg} \right]^2 + \left[\sum_{i,j,k,l} T_{ijkl} x^i_{fp} y^j_{fp} \theta^k_{fp} \phi^l_{fp} - \theta^0_{tg} \right]^2 \right\} \quad (4.4)$$

where the summation $\sum_s$ is performed over all the events in the statistic set. Notice that the calibration of the angles is performed simultaneously for both angles.

The experimental task is then to fix the values of y^0_{tg}, θ^0_{tb} and ϕ^0_{tg}. The procedure is the following:

- To fix y_{tg} (the transverse vertex position) a special optics target has been built. It is a set of nine thin ^{12}C foils, which allows for fixed values of z^0_{tg} (the vertex along beam-line). The data set used in the calibration consists of beam electrons scattering quasi-elastically from carbon into the spectrometer. It is important that the spectrometer be placed at such an angle as for the carbon target to span the full transverse acceptance ($\pm 5cm$ at the hall center) of the spectrometer.

- The spectrometer entrance is covered by a sieve-slit collimator, which is made of thick cadmium and has 49 small holes drilled at pre-determined positions. A drawing of the collimator can be seen in Fig. 4.1 (left).

- The combination of a particular hole on the sieve-slit and of a particular carbon foil defines a specific y^0_{tg}, θ^0_{tb} and ϕ^0_{tg}.

In order for the above mentioned variables to be known correctly, surveys have been performed, which have measured the positions of the target, the sieve-slit, and the spectrometer to a very high precision. A number of caveats exist when performing the optics calibration. Since the data set consists of quasi-elastic events, the distribution of those events across the spectrometer angular and momentum acceptance is determined by the strongly changing cross-section of quasi-elastic electron scattering on ^{12}C. It is then very important to weight the use of data in such a way as to uniformly span all the focal plane variables[1].

Calibration Procedure and Results

The first step of the calibration is the subtraction of detector offsets. Ideally, the detector package should be perfectly aligned with the central ray of the spectrometer. This however is not the case, and due to mechanical issues it is practically impossible to keep the detectors perfectly aligned with the ideal center. There are always offsets of order $1-2mm$. Furthermore, other non-linear offsets are also possible: the detector package may be tilted, both in vertical and in horizontal plane. Furthermore, the position offset of the detectors may vary across the detector face. This is due to the fact that the detectors may be somewhat bent and not perfectly rectangular.

To correct for these offsets we choose the data from the central foil of the carbon target, and from the central large hole of the sieve slit collimator (see Fig. 4.1(left)). Since both the

[1]One could of course argue that this may not be the most optimal thing to do, since the distribution of *production data*(i.e. data which is used to study the overall physics problem of the experiment) might not be uniform itself. In this case it might be wiser to weight the calibration in such a manner as to mimic the production data.

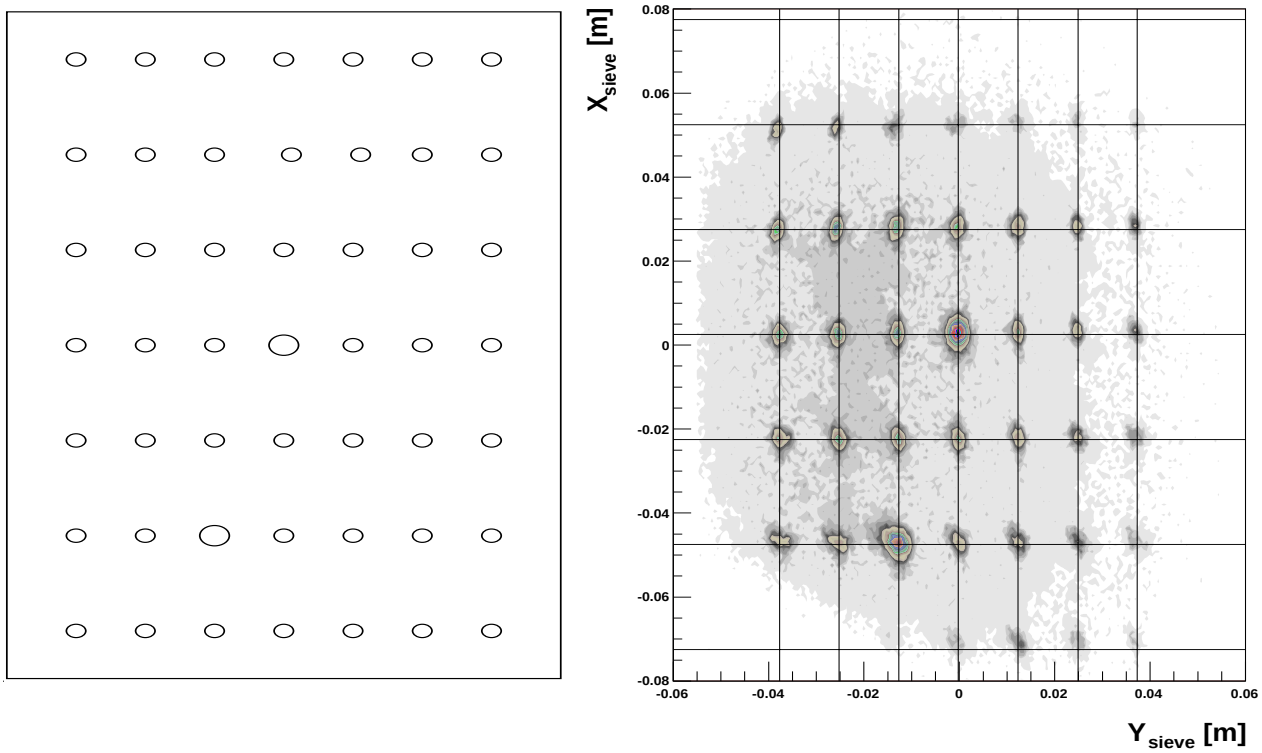

Figure 4.1: Left: Sieve-slit collimator pattern. Right: plot of event coordinates as projected on the sieve slit plane, clearly showing the position of the holes (compare with the picture on the left). The intersection of the lines correspond to the actual measured position of the holes.

central hole of the sieve-slit and the central foil of the target are set to be approximately on spectrometer's central axis, this selects trajectories which followed the central ray of the spectrometer. This makes the three focal plane variables of Eq. 4.3 vanish, $y_{fp} = \theta_{fp} = \phi_{fp} = 0$, leaving the final target variables sensitive only to a sum over the powers of x_{fp}, i.e.:

$$y_{tg} = \sum_i Y_{i000} x_{fp}^i \quad , \quad \theta_{tg} = \sum_i T_{i000} x_{fp}^i \quad \text{and} \quad \phi_{tg} = \sum_i P_{i000} x_{fp}^i \tag{4.5}$$

Here Y_{i000}, T_{i000} and P_{i000} entirely correspond to the position and angular offsets of the detector package. By doing a 2nd order fit, we achieve the following values for the offsets

(the units are in meters and radians):

$$\begin{array}{cccc} Tensor & i=0 & i=1 & i=2 \\ Y_{i000} & -7.7491 \cdot 10^{-3} & 1.7564 \cdot 10^{-3} & 7.8145 \cdot 10^{-4} \\ P_{i000} & -2.4842 \cdot 10^{-3} & -1.2188 \cdot 10^{-3} & -2.8384 \cdot 10^{-4} \\ T_{i000} & -1.0052 & -3.3331 \cdot 10^{-1} & -4.0880 \cdot 10^{-2} \end{array} \tag{4.6}$$

By studying the first row, corresponding to Y_{i000}, we conclude that the detector package has a general "zero-th order" offset of $7.5mm$, that the offset is increasing as one moves away from the origin, implying that the whole package is tilted by $\arctan(0.0017) \approx 0.1^o$. Also, observing a non-zero 2nd order term, we conclude that there is a slight bent in the VDC frame. Similarly, the non-zero values of P_{i000} and T_{i000} are indicating to an angular offsets of the VDC detector plane [2]

Once the offset corrections have been subtracted, the rest of the optics calibration can follow as described in the previous subsection. First, angular optimization is performed. The results can be seen in Fig. 4.1, showing a good agreement of the reconstructed sieve holes with their actual locations (intersections of the lines). The offsets of the central 5×5 holes

[2]The large value of T_{0000} is due to VDC's being set at 45^o angle to the central axis of the spectrometer, hence $T_{0000} \approx \tan(45^o) = 1$.

from their ideal positions can be seen in the table below (results are in *miliRadians*):

	$\delta\theta_1\ \delta\phi_1$	...			
$\delta\theta_1\ \delta\phi_1$	$-0.075, 0.076$	$0.18, -0.27$	$-0.33, 0.06$	$0.68, -0.6$	$0.9, 0.57$
$\vdots$	$-0.4, -0.1$	$-0.5, 0.25$	$-0.8, 0.3$	$-0.6, 0.4$	$-0.4, 0.6$
	$-0.2, -0.04$	$-0.3, 0.1$	$-0.4, 0.1$	$-0.4, 0.4$	$-0.3, 0.7$
	$-0.3, 0.3$	$-0.3, 0.2$	$-0.03, 0.1$	$-0.3, 0.2$	$-0.2, 0.5$
	$-0.1, -0.2$	$-0.1, 0.04$	$-0.2, 0.04$	$-0.3, 0.1$	$-0.5, 0.4$

(4.7)

Finally, once the angular calibration has been performed, we perform vertex coordinate calibration. The resulting distributions can be seen in Fig. 4.2. The left plot shows the nine foils of the optics target, while the right plot shows the dependence of the vertex position from scattering angle. As expected, there is no correlation between the later two variables, pointing to the stability of the optic reconstruction.

4.3 Photon Data

One of the key parts of the data analysis process is the reduction of data acquired from the calorimeter. At the lowest level this consists of the digitized ADC signals from the photo-multiplier tubes which are connected to the lead-glass blocks of the calorimeter (see Ch. 3.3.1). The amplitude of the signal is a measure of the energy deposited inside the block. Once the hit cluster has been identified, the sum of the ADC values corresponds to the total energy of the incoming photon. Also, by calculating an ADC weighted average of the block positions one can obtain the hit position. The energy and the hit position of the photon are needed to reconstruct the entire two-body reaction at the vertex.

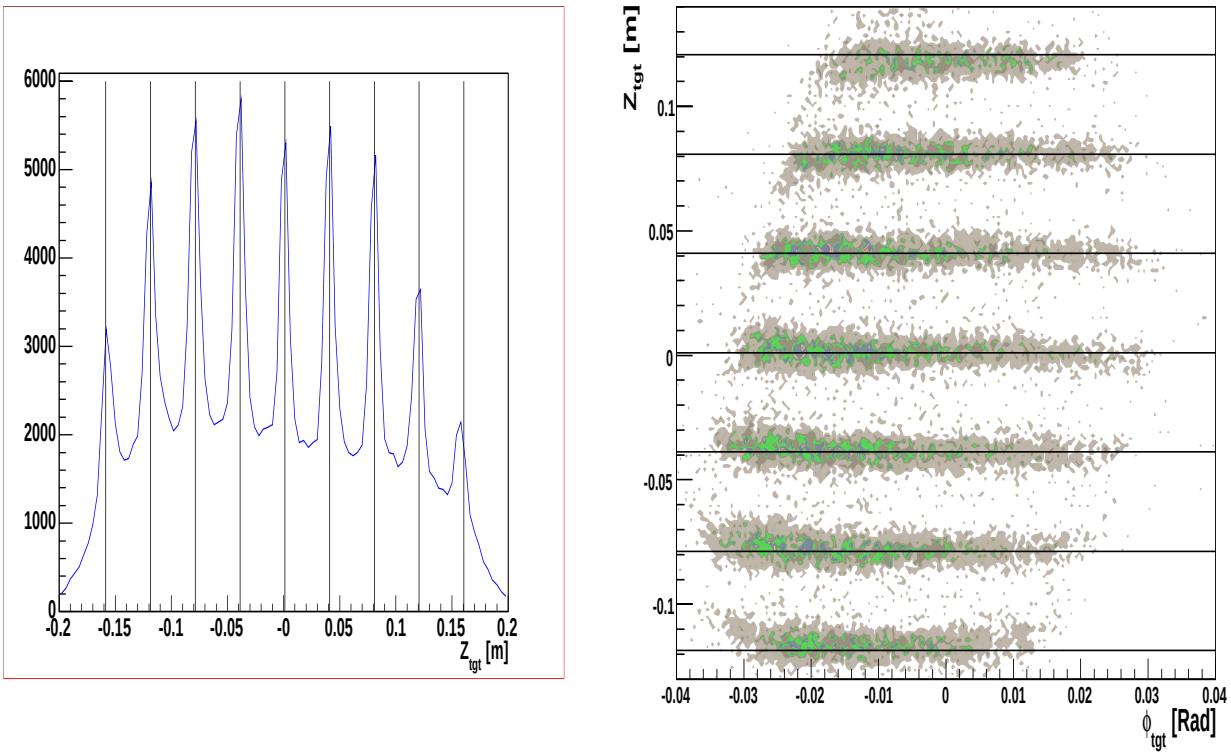

Figure 4.2: Left: the nine foils of the carbon target. Right: vertex position plotted against scattering angle. The lack of any correlation points to a good calibration and a stable optic transformation tensor. In both plots the lines correspond to the measured target foil positions.

However, to proceed with these steps, one first of all needs to find the correspondence between the ADC value and the energy deposited in the block corresponding to that ADC. A detailed description of calorimeter energy reconstruction and calibration procedure can be found in Ref. [10].

4.3.1 Energy and Position Calibration

When a photon or an electron enters a medium, it starts interacting with the electric field of the nucleus. This starts what is commonly referred to as an electromagnetic shower. In case

of an electron, the interaction causes it to experience bremsstrahlung and emit an energetic photon. The later, itself subject to the field of the nuclei, pair produces an electron and a positron, and the process of bremsstrahlung is repeated. At every "generation" of the shower, a single particle is converted to two, and the energy of an individual particle is on the average halved (assuming that the bremsstrahlung photon caries almost all the energy of the electron, which is of course the extreme case). The minimum number of the generations is determined using Eq. 3.1. The Čerenkov light emitted by the electrons and positrons is then detected by the photo-multiplier tubes.

As the shower is progressing, it is also spreading transversely relative to the direction of the original incoming particle. So, the lead glass block where the particle entered will experience the strongest signal, since the peripheral blocks of the cluster will register the "tails" of the transverse spread of the shower. The simple sum of the energies of the blocks will give the total energy of the shower:

$$E = \sum_i E_i$$

where the summation is performed over all the blocks of the cluster. Meanwhile, the position at which the particle entered the block can be reconstructed using so called "center of mass" method:

$$(x, y) = \sum_i (x_i, y_i) \cdot E_i / E \tag{4.8}$$

In order to reconstruct the energy deposited in a given block, one assumes that the ADC signal registered by the photo-multiplier tube is proportional to the energy. From here one can calculate E_i as

$$E_i = C_i \cdot (A_i - P_i)$$

where A_i is the ADC amplitude, P_i is the pedestal value, and C_i is the calibration coefficient.

In order to calibrate C_i one needs to know E_i. In order to achieve this calibration, part of the experimental beam time was used to accumulate elastic electron scattering data: the radiator was removed, and the kinematic setting was adjusted to observe elastic electron scattering. Once the proton is detected in the High Resolution Spectrometer, the electron's angle and energy can be reconstructed to very high precision, assuming two-body kinematics. This is then the needed input for the calibration. The calibration coefficients C_i are then determined by performing a numerical minimization of the error

$$\chi^2 = \sum_n \{ \sum_{i \in M_n} [C_i \cdot (A_i - P_i)] - E_n \} \tag{4.9}$$

where n is the event number, and E_n is the energy reconstructed from proton kinematics.

Results

Since the domain of calorimeter energies corresponding to the kinematic range of the experiment is very wide, calibration had to be performed for every single kinematic setting. Thus, before production data could be taken, elastic data was first acquired, to be used later for a calibration.

The results of calibration for kinematic point 5D can be seen in Fig. 4.3. The fits to the data show a calorimeter resolution of 5.4%. It also shows the intrinsic deficiencies of the "center of mass" method of position reconstruction, as one can see that the events are artificially systematically concentrated around the block centers. The plots in Fig. 4.4 contain fits to distributions of in-plane correlation δx and out-of-plane co-planarity δy for elastic $ep \rightarrow ep$ events. These show that the combined angular resolution of the experiment

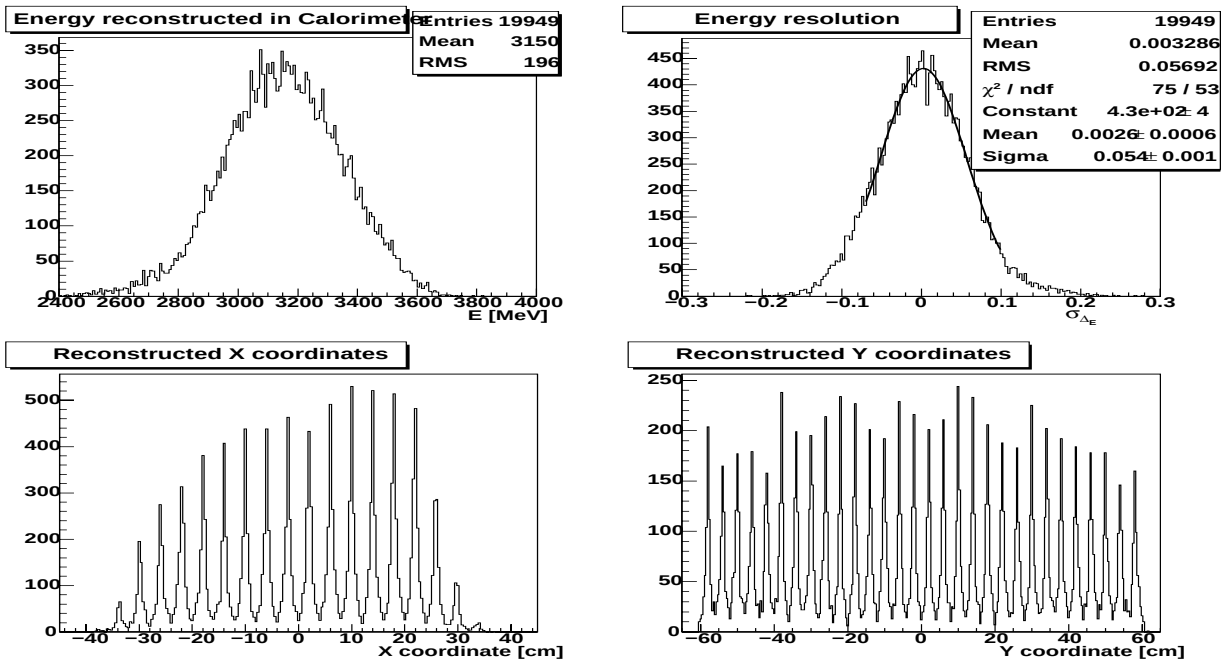

Figure 4.3: Top: plots of calorimeter energy E and $(E - E(p))/E(p))$, where $E(p)$is the expected energy, calculated from proton kinematics. The second plot is fitted, showing a calorimeter resolution of 5.4%. Bottom: Reconstructed calorimeter hit position coordinates. From Ref. [10].

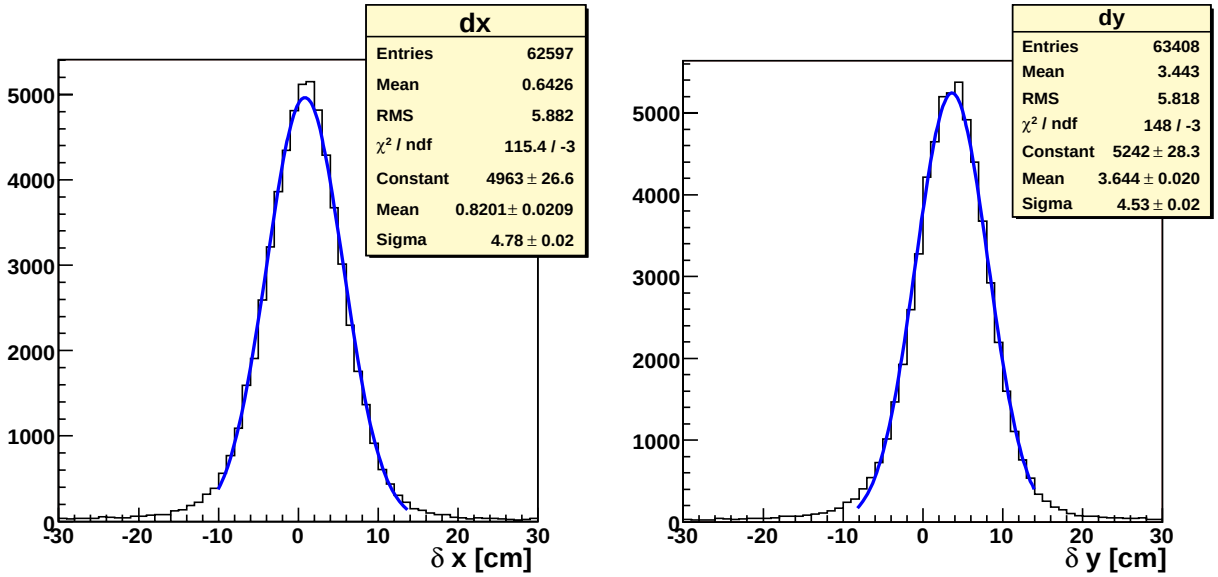

Figure 4.4: In plane (left) and co-planarity(right) correlations, calculated by subtracting measured calorimeter position from the predicted position as calculated from proton's kinematic variables. The Gaussian fits reveal the combined vertical and horizontal coordinate resolution of the experiment: 4.8 *cm* and 4.5 *cm* at the distance of 1200 *cm*.

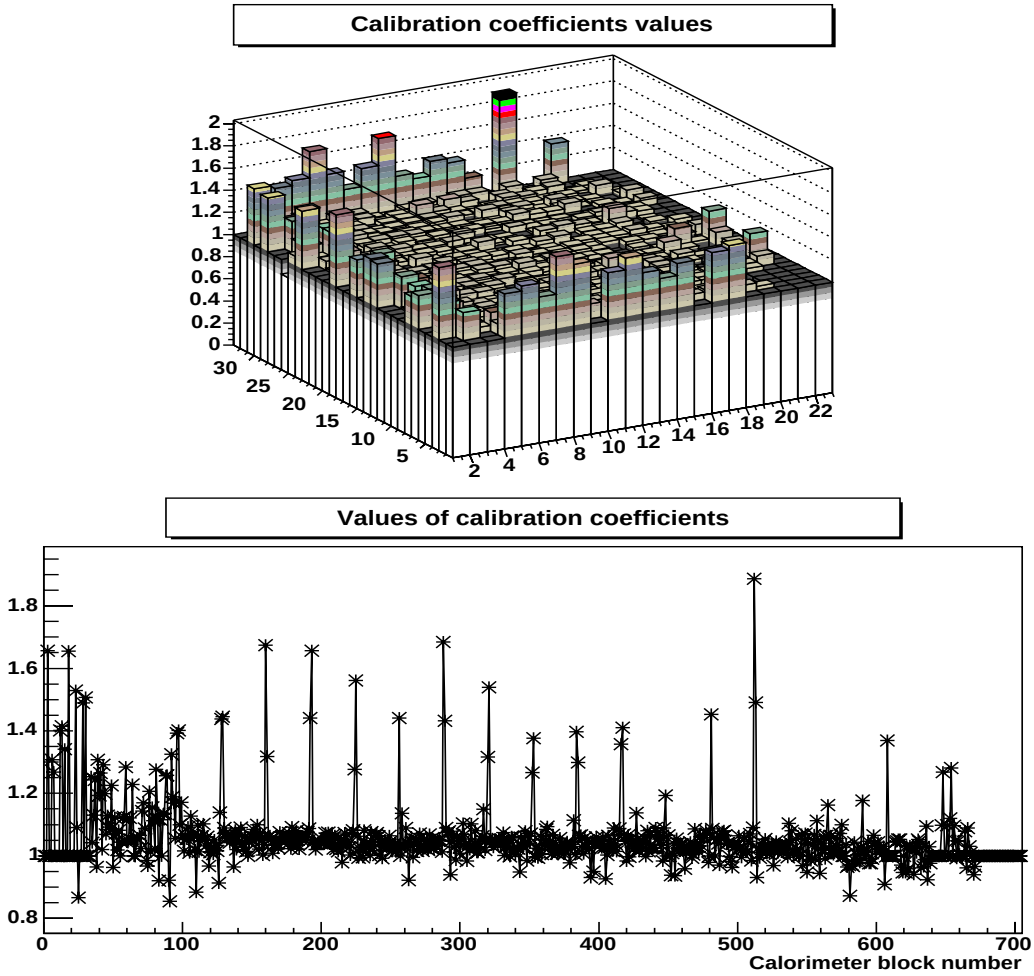

Figure 4.5: Calibration Coefficients C_i for every block of the calorimeter. From Ref. [10].

(in kinematic point $2A$, where the plotted data was taken) is about 4 $mRad$.

Another important feature of the calibration is the dependence of calibrated C_i coefficients on block number. Fig. 4.5 shows that the calibration of the peripheral blocks has yielded abnormally large values. The external positioning of the peripheral blocks causes them to "participate" in considerably less number of events, resulting in deficient calibrations. This problem is resolved by simply excluding the data corresponding to these blocks from the data analysis process. A C++ software package for analyzing the calorimeter

data has been developed by the collaboration. For a detailed description of the calorimeter analysis software refer to [55].

4.4 Coincidence Data

Once the first stage of data analysis (reduction) has been completed and the data has been analyzed both for proton arm and photon arm, a merging procedure is performed, where a ROOT based software is used to read in the outputs of ESPACE and ROOT Analyzer as input and to produce a single "merged" file as an output. A number of useful kinematic calculations were also included during the process of merging. These included calculations of incident particle's reconstructed energy, as well as scattered particle's angle and energy, all based on two body kinematics.

4.4.1 Event Structure and Separation

Once a final merged file is ready, one can start performing the first stages of scientific analysis, such as determining kinematic cuts. The goal of the preliminary, or "on-line" analysis it the determination of preliminary cross sections. This "pre Monte-Carlo" (pMC) analysis has been performed at different degrees of involvement since the end of the experimental run. Besides providing quick and arguably approximate answers to theoretical questions, the preliminary results can be refined to the point where they can be used as a benchmark for the final results. In this way, the difference between the results acquired using the Monte Carlo simulations and the results achieved using the preliminary analysis can be a measure of the systematic

uncertainties of the experiment.

Before discussing the challenges and deficiencies of the preliminary pMC analysis (and the subsequent need of a numerical model for the experiment) , it is important to first understand the general approach to the analysis. As mentioned earlier, the main difficulty of the experiment is its complex event structure: elastic electron scattering, neutral pion production, post-scattered electron bremsstrahlung, virtual Compton scattering(VCS) and finally real Compton scattering(RCS). Separating these event types is a highly non-trivial task. It is important to choose a kinematic variable (or a derivative of those) which will reveal best the differences between these event types. The variable which was chosen are the co-planarity and in-plane angular correlation between the two arms:

$$\delta x = x_p \ - \ x$$

$$\delta y = y_p \ - \ y$$

where x and y are the calorimeter hit coordinates, while x_p and y_p and those calculated based on proton information *and* assuming two-body kinematics, as well as a zero mass for the outgoing particles. If resolution and detector offset effects are ignored, δx and δy will be zero for the RCS events [3]. A plot of $\delta x, \delta y$ and E_{calo} can be seen in Fig. 4.8. The electrons are offset considerably due to the deflection which they experience in the magnetic field of the RCS magnet. Meanwhile, the neutral pions decay almost instantaneously after their production, in a manner which is isotropic in their rest frame, producing a uniform background. The main issues facing the analysis are following:

[3]This is also true for the VCS events. However the later can be subtracted with ease, see Chap. 6.2 for details, hence for the rest of the discussion we will not mention this even type, and hold their subtraction until the very end

- Subtraction of

  – neutral pion decay background and

  – post-scattered electron bremsstrahlung background.

- Inclusion of acceptance-related losses in determination of cross section.

Neither of these is by any means trivial. The shape of the pion background and bremsstrahlung is not obvious, and can cause large systematic uncertainties at kinematic points where the coordinate and energy resolutions are especially low. However, as mentioned earlier, besides these defects, the preliminary results achieved through polynomial fitting can be used to determine the overall systematic uncertainties of the experiment.

4.4.2 Preliminary Polynomial Fitting

In this subsection I will provide a description of preliminary data analysis, and as an example I will use the analysis performed on kinematic point 5A, which is one of the points which have the largest backgrounds.

The first step of the data analysis is to determine the standard cuts needed which will reduce background and remove the acceptance effects. The variable fG_EV_type denotes the particular type of trigger which an event satisfied. The type $fG\_EV\_type = 5$ corresponds to events which recorded a hit in the calorimeter *and* proton spectrometers S0 scintillator detector (see Chap. 3.5.1). However even after placing the coincidence cut, the highly sensitive nature of the experimental apparatus allows for a very large volume of accidental coincidences. To observe and manage the structure of the accidental background,

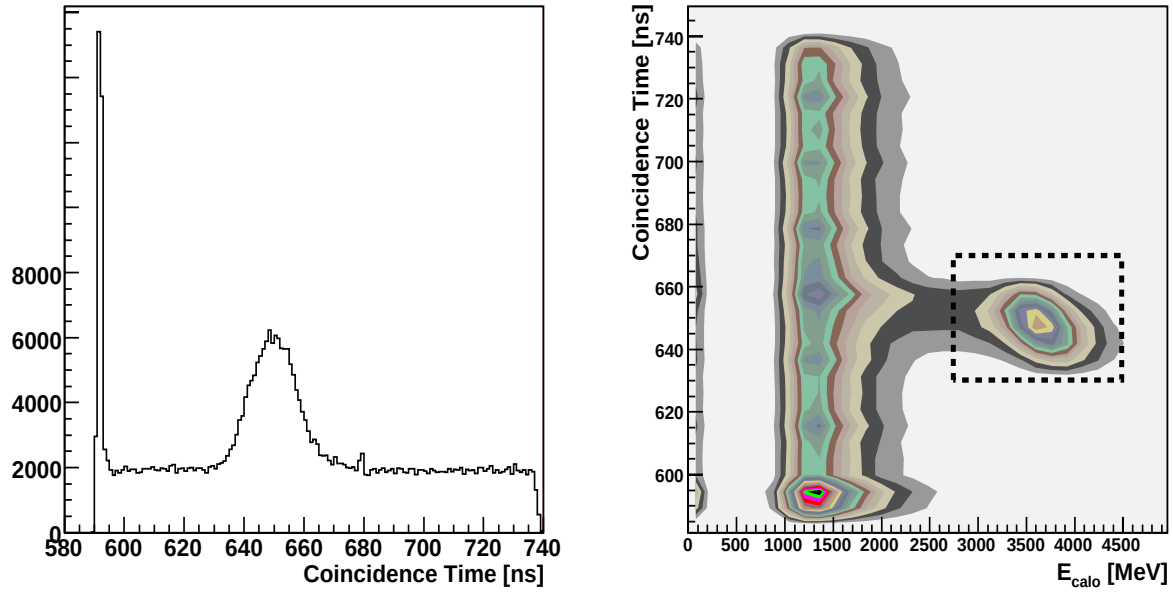

Figure 4.6: Left: time difference("coincidence time") between the hits in the two arms for coincidence events. Right: coincidence time vs. calorimeter energy for the events which registered coincidence hits between the two arms. The doted square denotes the cut used for data analysis.Both plots are done for kinematic point 5A.

it is very useful to look at the coincidence time between the two arms: that is, the time interval between the two hits. Coincidence time for real events should be a fixed number, somewhat smeared by detector related effects. The accidental background on the other hand should have a uniform distribution in time. Fig. 4.6 (left) illustrates this point very well. As it becomes clear from the plot, solely a coincidence time cut won't suffice to remove the background. In Fig. 4.6(right) one can see the distribution of background as a plot of time versus calorimeter energy. A combined energy and time cut can almost entirely eliminate the accidental background, without a tangible effect on actual physics event. A number of other cuts which further reduce the probability of random background include cuts on vertex coordinate, with the purpose of removing data from the target end-caps.

The next task is to determine the cuts needed for elimination of uncertainties due to acceptances. While in the scope of preliminary work it is very important to choose the correct cuts, it is however of no importance in the overall domain of this dissertation, since our final results were obtained using Monte Carlo simulations which did take into account acceptances and hence involved very wide cuts. Therefore we will limit the discussion to the minimum, with the limited purpose of only providing a general understanding of the methodology and procedure.

The goal of the acceptance cuts is to eliminate parts of the phase space where events are lost due to acceptance in a manner which is not possible to account for. Once the cuts have been determined, the cross sections can be calculated using $d\sigma/d\Omega \propto Y/(\Delta\Omega)$ where $\Delta\Omega$ is the solid angle corresponding to the acceptance cut. There are two manners of constraining the acceptance, the first and most obvious one being the one of placing cuts on spectrometer variables (since acceptance affects primarily the proton arm). However, due to a number of reasons – including but not limited to the need of determining the Jacobian $d\Omega_p/d\Omega_\gamma$ – it has been decided that a corresponding cut will be placed on scattered photon angle *and* incoming photon energy. The full list of the cuts is the following:

- Event type – coincidence: $fG\_EV\_type == 5$
- Coincidence time: $fG\_MS\_tdc1\_c[7] \in (630, 670)\ ns$
- Calorimeter energy: $fG\_GC\_e > 2750 MeV$
- Vertex: $z_{trgt} \in (-6, 6)\ cm$
- Beam Energy: $E\_in \in (5300, 5500)\ MeV$

- Photon in-plane geographic angle: $fG\_GC\_ph \in (-5.2, 5.2)\ mRad$

- Photon out-of-plane geographic angle: $fG\_GC\_th \in (-30.6, 30.6)\ mRad$

Once the standard cuts have been identified, the next step consists of determining the cuts on δy(see Fig. 4.8). The purpose of this cut is to reduce the pion decay background, which strongly contributes to the statistical error. It was decided to place a $2\sigma_y$ cut on δy, and then correct the yield by 1/.95. However, in order for this step to be accurate, it is imperative to know both the mean of y as well as σ_y very precisely. To achieve this, an iterative procedure of repetitive fitting is performed: first, very tight and approximate cuts are placed on δy and a fit of δx is performed; then a similarly tight cut is placed on δx and δy is fitted. This is repeated twice, until a very precise values of δx_0 and δy_0 are acquired.

Fitting Function: δx and δy

A fitting function for δx and δy is chosen, based on the assumption that the effects defining the RCS and elastic electron peaks are of stochastic nature, and hence the shape of the peaks is Gaussian, in both dimensions. Meanwhile, a smooth 2nd order polynomial is used for the pion decay background. The functions used to fit δx and δy are

- δy: $a_0 + a_1 \cdot \delta y + a_2 \cdot \delta y^2 + a_3 \cdot e^{-(\delta y - a_4)^2/2a_5}$

- δx: $a_0 + a_1 \cdot \delta x + a_2 \cdot \delta x^2 + a_3 \cdot e^{-(\delta x - a_4)^2/2a_5} + a_6 \cdot e^{-(\delta x - a_7)^2/2a_8}$

The results of the fits can be seen in Fig. 4.8 (top), and the schematic structure of the data is illustrated in Fig. 4.7.

Fitting Functions: E_{calo}

A process which we haven't yet fully discussed is bremsstrahlung radiation by electrons. The Fig. 4.7 shows the propagation of the electron events through the experimental setup. As the electrons are scattered in the target, they travel through dense target material, through vacuum windows and air, before being deflected by the magnetic field of the dipole magnet. However, during their trajectory preceding the deflection the electrons can interact with these materials and produce bremsstrahlung radiation. The bremsstrahlung photons are almost parallel to the electrons, and have the same angular kinematic dependences as the RCS photons, a circumstance which makes them angularly indistinguishable from the RCS events.

If there were no bremsstrahlung photons in the data, the yield would be determined from the above fit, and the preliminary analysis would end there. However, the presence of bremsstrahlung photons complicates the picture somewhat: the Gaussians of Fig. 4.8(top) are only partially made of RCS events and contain a large number of bremsstrahlung events. This calls for an additional step in the analysis. The only manner to distinguish and subtract the bremsstrahlung photon events is to observe their energy as registered by the calorimeter.

Again, to minimize the participation of pion decay background, which inherently increases the statistical error, we place a narrow $\pm 2\sigma_x$ cut, centered on δx_0. Using our fits of δx we determine the so-called dilution factor $D = Pi/(RCS + ep\gamma)$. Next, we refer to the calorimeter energy of the events inside the cut. However, calorimeter energy proper reflects also the combined energy acceptance of the experiment. To subtract this effect, we instead

plot the variable

$$E \;\rightarrow\; \Delta E + < E > \quad \text{with} \quad \Delta E \equiv E_{calo} - E(p) \tag{4.10}$$

where $E(p)$ is the calorimeter energy *predicted* from proton side, assuming two-body kinematics. Fig. 4.8(bottom) shows the distribution of $\Delta E + < E >$.

The Gaussian peak itself represents the combination of the RCS and pion decay events. Since the narrow cuts on δx and δy correspond to the pion decay photons with a rest-frame decay angle of ≈ 0, these photons carry essentially the full energy of the pions, which – given the fact that vertex-kinematic dependences have been entirely canceled by the subtraction of $E(p)$ – can be assumed to be approximately equal to that of the RCS events. The combination of the above arguments allows us to treat the RCS and pion decay events in this plot as essentially the same.

The long tail below the Gaussian is the shape of bremsstrahlung radiation. It can be approximated to have a $\propto 1/E$ dependence on energy, with a sharp cutoff at endpoint E_0. Since the electron, which was the source of bremsstrahlung radiation had an energy identical to that of RCS event, here E_0 is simply the energy of the RCS event, and should coincide with the mean of the Gaussian representing RCS and pion decay events. This type of dependence can be modeled with the following approximate analytical expression:

$$\frac{E_1}{E} \cdot \frac{1}{e^{\frac{E-E_0}{E_2}} + 1} \tag{4.11}$$

The first factor of the expression is simply the $1/E$ dependence of bremsstrahlung spectrum on energy. The second factor is the energy spectrum of Fermi distribution: this is a factor which is ≈ 1 when E is less than E_1, and ≈ 0 when E is greater than E_1. At the border

region of $E \approx E_1$ it "smears" the otherwise sharp step by the measure of E_2. Combining this with the Gaussian for the RCS and pion decay events we get

$$\frac{E_1}{E} \cdot \frac{1}{e^{\frac{E-E_0}{E_2}} + 1} + E_3 e^{(E-E_0)^2/2E_2}$$

where E_0, E_1 and E_2 are the fitting parameters. Notice two important features of the above function: the mean of the Gaussian E_0 and the "cutoff" of the Fermi distributions are the same – this reflect the requirement that bremsstrahlung endpoint is equal to the RCS photon energy; the "smearing" of the Fermi distribution is equal to the variance of the Gaussian: this is because measurements of RCS photon energy and bremsstrahlung spectrum's endpoint are limited by the same calorimeter resolution, E_2.

Once fitting is performed, and the coefficients are determined, the absolute number of bremsstrahlung events can be determined by integrating Eq. 4.11. The rest of the events in the histogram correspond to the sum of the RCS and pion decay events. Using the information about the dilution factor from the δx fit, we form two equations with two unknowns:

$$D = Pi/(RCS + ep\gamma)$$

$$Pi + RCS = A$$

where A and $ep\gamma$ have been determined from the energy fits. This allows us to determine RCS yield and to use it to calculate the cross section.

4.4.3 Shortcoming of Preliminary Analysis

While the above discussion detailed the logic, the methodology behind and the merits of preliminary analysis, it also revealed its shortcomings. First and but not foremost, it involves severe cuts on acceptances, resulting in considerable loss of statistics. But most importantly, it involves a very large number of fit parameters: 19 for the overall fit, and 10 to determine the cross sections. It is intuitively assumed that the polynomial fit to the pion background in Fig. 4.8(top) does in fact correspond to the reality, however there is no rigorous basis to this assumption. For the kinematic points where $\sigma_{\delta x}$ and$\sigma_{\delta y}$ are large this is of a particular concern, since the pion decay backgrounds then plays a larger role in determining the RCS yield. The same can be said about the assumptions that the pion decay events in Fig. 4.8(bottom) does in fact follow a Gaussian form. And more importantly, Eq. 4.11 is clearly a very approximate model for the behavior of the bremsstrahlung, not only because the $1/E$ dependence of the spectrum is not exact, but also because that background – originating from electrons – is also dependent on acceptance effects. Furthermore, while Fermi distribution is a clever and ingenious analytic model for resolution effects, it is by no means an exact one: the Fermi distribution function describes a process where particles, due to thermal interactions within the Fermi sea, are excited into *higher* energy states, hence causing the "smear" of the otherwise sharp step. Resolution effects on the other hand have a "two-way" character – they affect statistic samples in both directions.

The above listed problems, while small by themselves, can add up to large systematic uncertainties for the kinematic points where background volumes are large. This is the reason why a full numerical model of the experiment is needed in order to understand fully

the event structure and physical composition of the data.

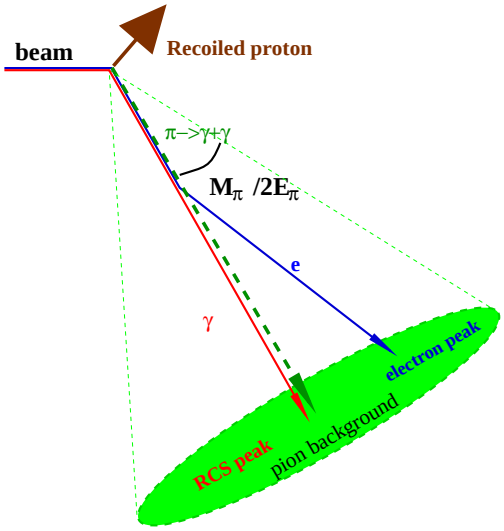

Figure 4.7: A schematic illustration of data and background structures.

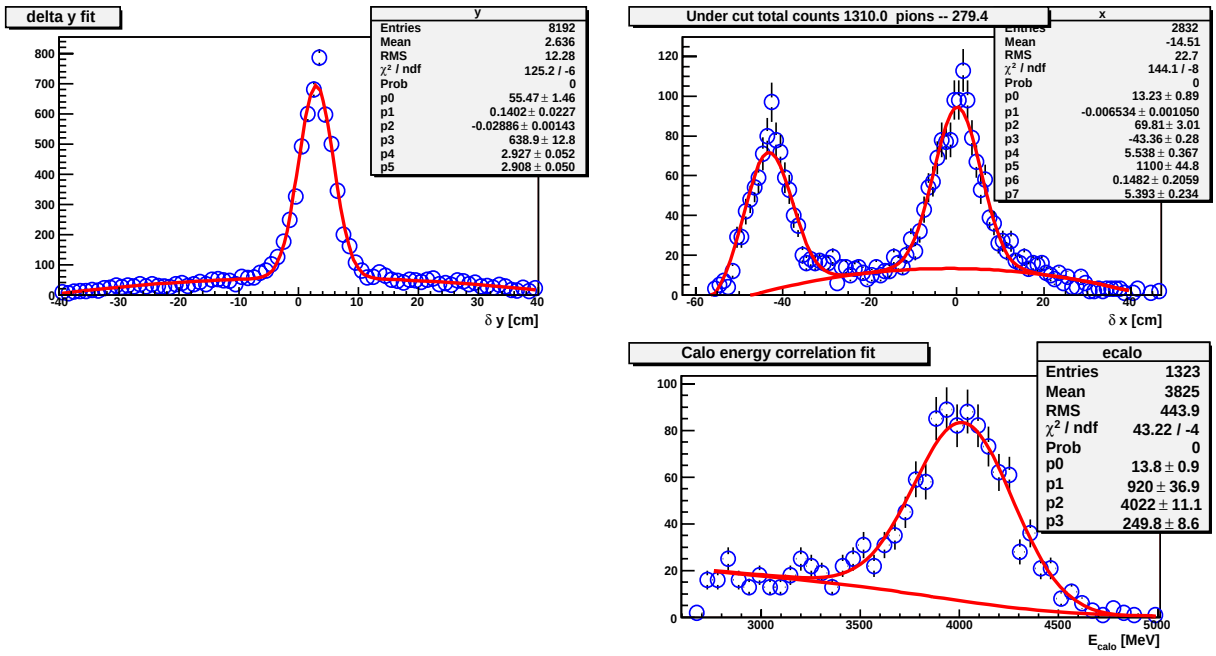

Figure 4.8: Top: plots of δy and δx, revealing RCS peak at $\delta y \approx \delta x \approx 0$, the electron peak at $\delta x \approx -40$ *cm* and the π^0 decay background continuum underneath the peaks. The fit consists of a combination of two Gaussian functions (to account for RCS and *ep* events) and a polynomial functions to account for pion background.

Bottom: calorimeter energy distribution, fitted using a combination of a Gaussian and a $1/E$ function which has been "smeared" by calorimeter resolution.

Chapter 5

Monte Carlo Simulation

5.1 Introduction

Monte Carlo method is a very versatile computational tool which is extensively used not only in nuclear physics, but also in such seemingly unrelated fields as medical physics, market finance, and biology. In its essence, Monte Carlo is a numerical method of evaluating integrations and convolutions of very complex (and sometimes non-analytical) functions – a task which is often impossible to perform analytically. The general purpose of the Monte Carlo is to sample a particular phase space with a known (or assumed) distribution, and then apply different conditions: at this point one can calculate expectations and other observable quantities.

5.2 Monte Carlo Method

A typical Monte Carlo consists of two main parts: event generator, and "condition cut." The purpose of the event generator is to simulate the initial conditions of the process. It samples the phase space in a manner which is similar to a particular known(or assumed) function. Question arises – how does one generate a statistic set of numeric events which are distributed according to a particular probability density function? There are different methods to achieve this, but all of these methods need a good random number generator, which generates a uniform and statistically independent numerical values in the interval of [0,1). There are a number of different well known generators. The one used in our work is called RANLUX, and belongs to the CERNLIB libraries [53]. It has a very large period, and is based on mathematical models derived from chaos theory [56].

5.2.1 Rejection method

Also known as "Metropolis" or "Van Neumann" method, the Rejection Method is intuitively the simplest manner to achieve a statistic distribution based on a particular multi-dimensional probability density function. In order to generate a statistic set with a distribution $f(x, y, z)$, we generates four random number:

$$x_{rnd} = x_{max} \cdot rand[0,1) \qquad y_{rnd} = y_{max} \cdot rand[0,1) \qquad z_{rnd} = z_{max} \cdot rand[0,1) \qquad \text{and}$$

$$f_{rnd} = f_{max} \cdot rand[0,1)$$

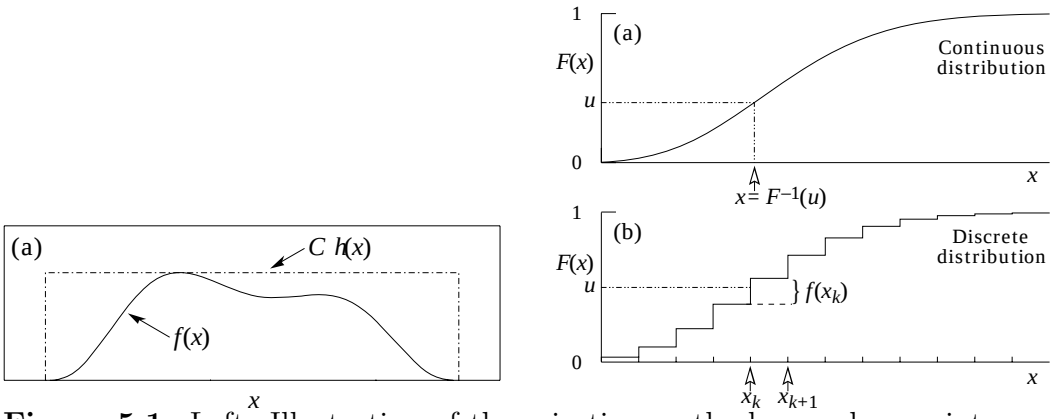

Figure 5.1: Left: Illustration of the rejection method – random point are sampled in the bounding box, and rejected if the ordinate is larger than $f(x)$. Right: Inverse Transform Method for continuous (a) and discrete (b) distributions

where $rand[0,1)$ is a random number between 0 and 1. In this way we have achieved some entirely random (within the random number generator's qualities, of course) values for $x,\ y$ and z (for simplicity's sake here we assume that $x_{min} = y_{min} = z_{min} = 0$). At this point we evaluate $f(x_{rnd}, y_{rnd}, z_{rnd})$ and apply the following condition:

$$\text{if } (f(x_{rnd}, y_{rnd}, z_{rnd}) < f_{rnd}) \qquad \{\text{reject}\}$$

$$\text{else} \qquad \{\text{keep}\}$$

If one were to repeat this procedure a very large number of times, then within statistic uncertainty the resulting distribution would be identical to $f(x, y, z)$. Note that $f(x, y, z)$ does not have to be an analytical function. For the cases where the probability density is a very complex function, it is useful to calculate it only once for an array of values of (x_i, y_i, z_i) before starting the main loop, and then use interpolation to determine $f(x, y, z)$ for a particular value of (x, y, z). An illustration of this method can be seen in Fig. 5.1.

One should be warned that while this procedure is rather simple, it may however involve a massive loss of computational time due to the necessary rejection of samples. This is true especially in the case when $f(x, y, z)$ varies strongly within the domain of interest. Not only does this method incur a loss of computational resources, but it also involves lower statistics for the parts of the phase space with relatively low $f(x, y, z)$. We do use Rejection Method in our event generator, however in our particular case the RCS cross sections do not change much within the detector acceptance, hence the above concern is not applicable.

5.2.2 Inverse Transform Method

For cases where the probability density is a one-dimensional function, it is possible to avoid the above mentioned inefficiencies of rejection method by using the Inverse Transform Method. Consider a continuous probability density distribution $f(x)$ and

$$F(x) = \left\{ \int_{x_{min}}^{x} f(x')dx' \right\} / \left\{ \int_{x_{min}}^{x_{max}} f(x')dx' \right\} \tag{5.1}$$

In this case $F(x)$ is itself a uniformly random variable in the domain [0,1], and by finding

$$x = F^{-1}(rand[0, 1])$$

we will generate a distribution which will be identical to $f(x)$. The above example can be easily generalized for discrete distributions, as can be seen in Fig. 5.1.

5.3 Monte Carlo Simulation of Experimental Apparatus

Cross section is one of the main observables which is used in experimental nuclear physics to test particular theories or models. Essentially, the cross section of a process (be it scattering, decay, or particle production) corresponds to the probability of that process occurring under particular kinematic constraints. The differential cross section is defined as

$$\frac{d\sigma}{d\Omega} = \frac{Y}{\Omega \cdot k \cdot N_\gamma} \tag{5.2}$$

where Ω is the solid angle of the detector acceptance, k is the concentration of scatterers per unit area ($\#nuclei/cm^2$), N_γ is the number of scattering particles (photons, in our case), and Y is the yield – the number of the detected scattered particles. Hence, assuming one knows $k \cdot N_\gamma$ (target and beam characteristics), the problem of measuring $\frac{d\sigma}{d\Omega}$ is reduced to evaluating $\frac{Y}{\Omega}$. The difficulty then is obvious – in even a slightly complicated experiment, especially one which employs a spectrometer with a very complex acceptance due to its magnetic optics, as described in Chap. 3, Ω has a very non-trivial dependence on detector geometries. Said in another way, the yield observable has a very complicated dependence on the geometries, and what we actually observe is not the simple $Y \propto \frac{d\sigma}{d\Omega} \cdot \Omega$ but rather a complicated convolution:

$$Y \propto \int_{allspace} \frac{d\sigma}{d\Omega} \cdot A(\Omega) \cdot \frac{dN(E_\gamma)}{dE_\gamma} \; d\Omega \; dE_\gamma \tag{5.3}$$

where $A(\Omega)$ is a sort of "acceptance" function – the probability that a particle outgoing into the infinitesimal solid angle $d\Omega$ will actually be registered by the detector setup. $\frac{dN(E_\gamma)}{dE_\gamma}$ is

the bremsstrahlung distribution – photon number per energy beam *per* incoming electron (hence the need later to multiply it by the number of the incoming electrons, N_e).

The above discussion shows the impossibility of the simplistic Eq. 5.2 approach to determining cross sections. Instead, a more complex approach is needed – that of Monte Carlo numerical simulations of the experimental procedure. The general concept of the simulation is the following: recreate the experimental procedure (starting with beam incident on target, and ending with particle detection), allowing only one (ideally) variable – cross section – to vary, and then compare the result with data. In other words we get two quantities:

$$Y_{data} = k \cdot N_e \cdot \int_{allspace} \left\{ \frac{d\sigma}{d\Omega} \right\} \cdot A(\Omega) \cdot \frac{dN(E_\gamma)}{dE_\gamma} \; d\Omega dE_\gamma \tag{5.4}$$

and

$$Y_{MC} = k \cdot N_e \cdot \int_{allspace} \left\{ \frac{d\sigma_{MC}}{d\Omega} \right\} \cdot A(\Omega) \cdot \frac{dN(E_\gamma)}{dE_\gamma} \; d\Omega dE_\gamma \tag{5.5}$$

where Y_{MC} is the simulated data which is generated with an assumed cross section $\left\{ \frac{d\sigma_{MC}}{d\Omega} \right\}$), Y_{data} is the actual yield in the experimental data, $\left\{ \frac{d\sigma}{d\Omega} \right\}$ is the *actual* (unknown) cross section, and $N(E_\gamma)$ is the energy spectrum of the incoming photon beam. The purpose of the calculation is to determine $\left\{ \frac{d\sigma}{d\Omega} \right\}$. To achieve this we simply divide Eq. 5.4 by Eq. 5.5 and rearrange, obtaining

$$\frac{d\sigma}{d\Omega} = \frac{d\sigma_{MC}}{d\Omega} \cdot \frac{Y_{data}}{Y_{MC}} \tag{5.6}$$

Notice that there are two assumptions in the above calculations: a) that the ratio $d\sigma/d\sigma_{MC}$ is approximately constant across the acceptance and b) that both Eq. 5.4 and

Eq. 5.5 have the same values for K,N_γ and for $A(\Omega)$. This is based on the *assumption* that our simulation is accurate, and that we are correctly reproducing the experimental apparatus. This, of course, needs to be checked – it is not unusual for experiments to ignore the presence of an object or piece of equipment which is blocking the acceptance. There are methods to check for and ascertain that the above assumption is in fact correct. We achieve this by collecting "controlled" data – data with a very simple event structure and known cross section, such as elastic electron scattering on proton – to study whether the simulation reproduces this data. Any deviations are treated as systematic uncertainties, and are included in the calculations of total uncertainties of the final experimental results.

Our Monte Carlo code was written in Absoft Fortran [52], which is a variation of F77, and has structures.

5.3.1 General Structure

The Monte Carlo used to simulate the experimental apparatus can be broken into the following sections:

- Input of kinematic variables and constants needed to calculate the RCS form factors and RCS cross section.
- Input of bremsstrahlung calculation for the 6% copper radiator.
- Use the above input (bremsstrahlung and cross sections) to determine the ratio of electrons to RCS to π^0 events for that particular kinematic point.
- Calculation of the RCS, π^0, and *ep* cross sections across the phase space to be covered

in the Monte Carlo. The phase space is divided into 40 steps (in polar angle and in beam energy), and for each point the cross section is calculated. This needs to be done very carefully, since in our Monte Carlo we generate the recoiled proton values(instead of scattered values), so appropriate Jacobians have to be applied where needed. These tables later will be used for a "Rejection Method" Monte Carlo.

- At this point the Monte Carlo output needs to be normalized to the accumulated charge of the experimental run. Hence, using a fixed value ($1mC$), the cross sections and the solid angle, the number of events corresponding to the covered phase space is calculated. This is the number of events which correspond to $1mC$. Here we also introduce a weight variable which is the ratio of the statistics requested by the user and the number of events corresponding to $1mC$. Later corrections for accumulated charge will be done at the end stage of the analysis (*e.g.*, if the *actual* charge was $2.5mC$, then the Monte Carlo output will be weighted by 2.5).

- Here start the Monte Carlo loop, which progresses in the following order:

  - First, using the above calculations, the reaction type is chosen between RCS, ep or π^0.

  - Beam energy is chosen using the inputs of bremsstrahlung calculations.

  - The vertex is chosen, randomly on the $15cm$ target.

  - Similarly, the azimuthal scattering angle is chosen randomly.

  - Using the Rejection Method and the tables of cross sections for the particular reaction, we choose a polar (total) scattering angle for the recoiled proton. Using

2-body kinematics we calculate the recoil momentum.

- From the above values of azimuthal and polar scattering angles (spherical coordinates) we calculate the "geographic" angles in spectrometer coordinate system(ϕ_{tg} and θ_{tg}). We do the same with the vertex coordinate(z_{tg} to y_{tg}) and momentum ($\delta = (p - p_{central})/p_{central}$).
- The coordinates and energy of scattered particle are calculated. For a π^0 event we also simulate the isotropic decay in pion's rest frame and transform it back to laboratory frame.
- A this point we have all the kinematic variables defining the event, and we can start with all types of corrections. First, we apply a combination of internal and external (a vertex-coordinate dependent adjustment to the exponent in cross section) bremsstrahlung radiative correction to the angle/momentum of the proton, and to the energy of the incoming and scattered electron.
- Multiple scattering is applied: in radiator; target entrance window; target exit windows; target chamber exit windows; air (on calorimeter arm).
- At this point the event is truly complete: we apply acceptances. First, we check if the event was within the boundaries of the calorimeter.
- Given that the event passed the above check, we use mc_hrsl.f from SIMC [65] simulation package to trace the proton back and forth through HRS, transporting it from target to focal plane, aperture by aperture (using COSY magnetic model for quadrupoles and dipole), and at every point checking whether the proton is

within the aperture or quadrupole geometry. In the case if any of these conditions fail, the event is abandoned.

- End of simulation. Calculations of peripheral kinematic variables (such as *calo_x* and *calo_y*). The HBOOK ntuple is filled.

The general RCS Monte Carlo structure is illustrated in the flow chart of Fig. 5.3.1

5.3.2 Input Parameters

The Monte Carlo code has been developed in such a manner as to allow for a simple operation under quick changes of kinematic variables. The input file is called ggmc.in, and among a number of fixed variables requires the specification of the following for each kinematic point:

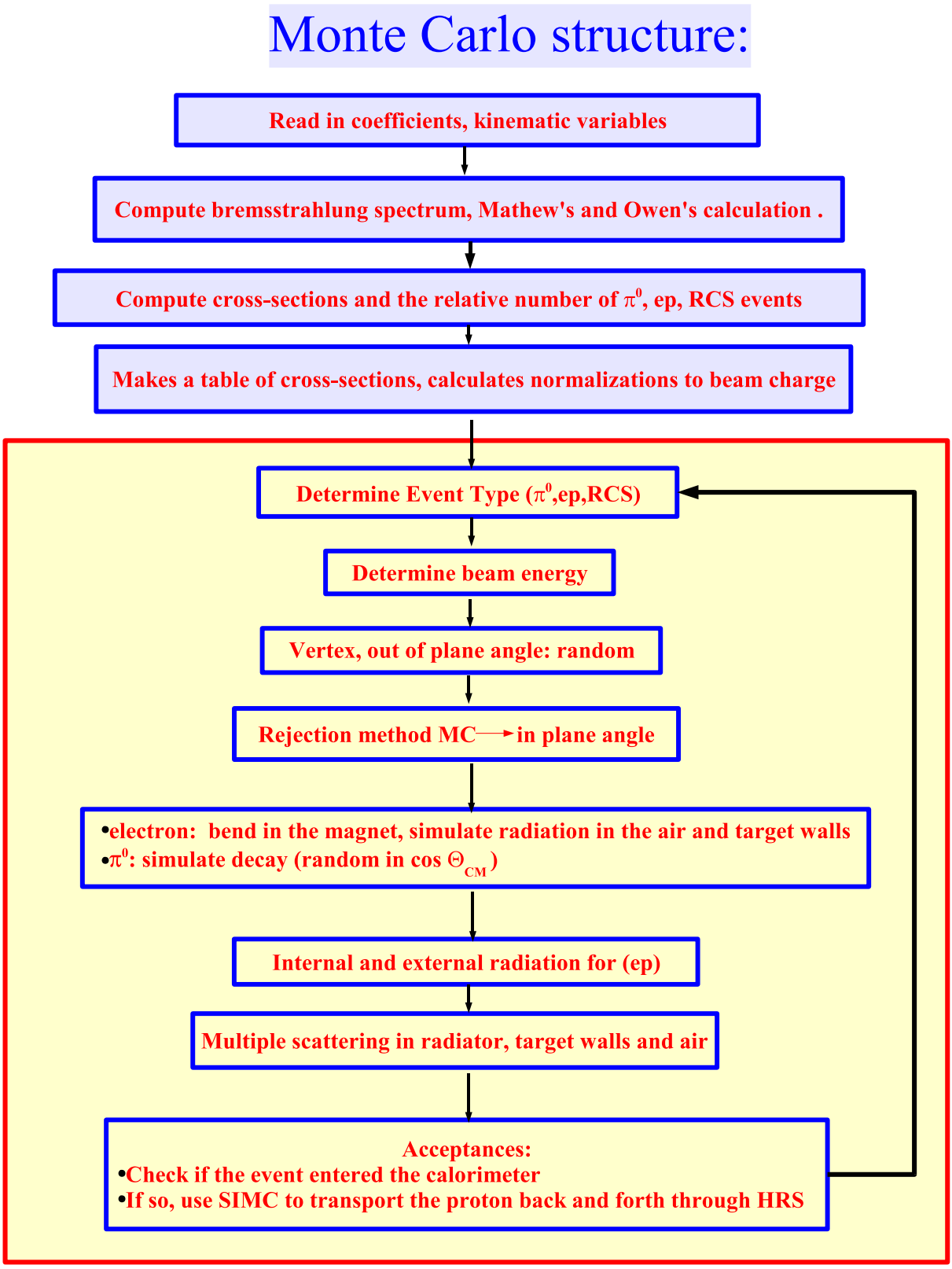

Figure 5.2: The structure of RCS Monte Carlo Simulation. The shaded region corresponds to the Monte Carlo loop itself.

Input Variables	Input type	Units
Number of Events to run	Integer	N/A
Radiator Thickness	Float	%
Polar (scattering) Angle of Event Generation	Float	mRad
Azimuthal (out-of-plane) Angle of Event Generation	Float	mRad
Relative Momentum of Event Generation	Float	%
Transverse Position Coordinate of Event Generation	Float	cm
Incoming Beam Energy	Float	GeV
Calorimeter Angle	Float	Deg
Calorimeter Distance	Float	m
High Resolution Spectrometer (HRS) angle	Float	Deg
High Resolution Spectrometer (HRS) central momentum	Float	GeV
Cu Radiator On/Off	Integer	1/0
Magnet On/Off	Integer	1/0
Magnet Current	Integer	Amperes
Random Number Generator Kernel	Integer	N/A
Name of output file	Character String	N/A

At this point all the setup and positioning of the detectors has been defined, and one can proceed with the actual simulation.

5.3.3 Bremsstrahlung Calculation

To start the simulation, we need to determine $N(E_\gamma)$ of Eq. 5.5. The liquid hydrogen cryo-target includes a copper radiator, which, with the target itself amounts to 6.84% of the radiation lengths for copper. The diagram for "external" bremsstrahlung can be seen in Fig. 5.3.7. There exists a rigorous analytical calculation by J.L. Matthews and R.O. Owens [41] for rather thin ($< 1\%$) radiator thicknesses. For an infinitesimal material with a radiation thickness of dt the bremsstrahlung yield is

$$\frac{d^2n(Z, E_0, k)}{dk\ dt} = \frac{3.495 \times 10^{-4}}{Ak} \left[Z^2\Phi_n + Z\Phi_e\right] \left(\frac{cm^2/g}{MeV}\right) \tag{5.7}$$

where the following variables are used: k is the photon energy ; E_0 is the incident electron energy; t is the thickness of material in radiation lengths ; A is the atomic number ; Z is the nuclear charge; Φ_e and Φ_n are electron-electron and electron-nuclear spectra, respectively. In order to determine the bremsstrahlung spectrum for a rather thick material we need to integrate not only over thickness, but also over the varying electron energy: as the beam traverses the radiator the bremsstrahlung radiation and ionization by collision with atomic electrons cause electron energy to decrease, a circumstance which leads to a completely different bremsstrahlung yield.

The two principal mechanisms which cause electron energy loss in the material are the following: ionization by electron-atom collisions $W_C(E, E_0, Z, T)$ (see calculations by Blunk and Leisegang [57]), and radiation loss due to electron-nuclear soft interaction, which has the spectrum of

$$W_R(E, E_0, Z, T) = \frac{[\ln(E/E_0)]^{\zeta-1}}{E \cdot \Gamma(\zeta)} \tag{5.8}$$

Here ζ is related to radiation thickness T through $\zeta = 1.44 \cdot T$, and $\Gamma(\zeta)$ is a parameterization based on Padé approximation [58]. In this case the total energy loss distribution is

$$W(E, E_0, Z, T) = \int_E^{E_0} W_C(E_0, E', Z, T) \cdot W_R(E', E, Z, T) dE' \tag{5.9}$$

Finally, after having calculated the total energy loss we can calculate the bremsstrahlung spectrum:

$$\frac{dN(k, E_0, Z, T)}{dk} = \int_{E_0-\Delta/2}^{E_0+\Delta/2} \frac{dE}{\Delta} \int_{k_{min}}^{E} dE' \int_0^T dt \; W(E', E, Z, t) \; \frac{d^2 n(Z, E', k)}{dk \; dt} \tag{5.10}$$

This is the correct formula for a thick radiator ($> 1\%$), which is clearly the case in our experiment. To calculate this complex integral numerically, a *c* code has been developed [59] at Jefferson Laboratory. The output of the code can then be used for calculating the total number of the bremsstrahlung photons in a particular energetic domain, or can be used as an input for the event generator of a Monte Carlo simulation – which is exactly how we use it. After the output of the computation is read by the Monte Carlo code and registered as an array, it's integral is calculated, to be used later according to Inverse Transform Method(see Chap. 5.2.2) inside the Monte Carlo loop proper.

5.3.4 Cross Section and Normalization of Yield to Accumulated Charge

Before entering the Monte Carlo loop we need to prepare a table of cross sections – $d\sigma_i(\cos\theta_i, E_i)/d\Omega$ – as well as compute the normalization to the accumulated charge.

The purpose of preparing tables of cross sections, instead of calculating them inside the loop, is that it will economize a considerable amount of computational time. For both

electron scattering and π^0 processes we use variable cross sections both in angle and energy, however for Compton Scattering events we use uniform cross sections. This is done so since it is easier to interpret the data, mostly due to the fact there is no certainty that the variation of theoretical cross section in fact corresponds to the reality. We do however use varying cross sections for π^0 photo-production, since the δx (see Chap. 4.4.1) distribution for the π^0 is somewhat correlated with the variation of cross section, and a good reproduction of δx distribution is essential for event separation.

As discussed in Chap. 5.3 the purpose of the simulation is to produce a statistic yield for a particular kinematic requirement with a particular accumulated charge and a particular acceptance. The idea of the event generator is to sample a phase space which is (has to be) larger than the combined acceptance of the experiment. This is critical: in order for the simulation to produce correct results, it needs to explore every corner of the phase space – both in terms of solid angle and momentum acceptances. Hence, we need to choose an incoming energy domain which is larger than the corresponding acceptance of the High Resolution Spectrometer (since the energy acceptance is primarily limited by the $\pm 5\%$ acceptance of the spectrometer), and a solid angle which is larger than that corresponding to the entrance window of the spectrometer. Once the correct values are chosen, we can calculate Eq. 5.5, which becomes

$$Y_{MC} = N_e \cdot k \int_{allspace} \left\{ \frac{d\sigma_{theory}}{d\Omega} \right\} \cdot \frac{dN(E_\gamma)}{dE_\gamma} \; d\Omega dE_\gamma \tag{5.11}$$

where the number of the electrons is found from accumulated charge and electron charge $N_e = C/e$, and k is found from $k = \rho \cdot l \cdot A$ – A being Avogadro's number, l being target thickness, and ρ being the density of liquid hydrogen. The integration is performed numerically. To

recapitulate, we calculated the yield for an accumulated charge C, which we conventionally chose to be $C = 1\ mC$. [1]

To simulate a process where C amount of charge has been accumulated, we need to sample a Y_{MC} events over the acceptance of the experiment, and then compare it to Y_{data} of Eq. 5.4 to calculate the cross section according to Eq. 5.6. However, we cannot limit our statistics to Y_{MC} as found above, since the number may in fact be too small for insuring a high statistic accuracy. So, to circumvent this, instead of sampling only Y_{MC} events, we sample a much larger $Y_{simulation}$ number of events, and later weight our final results by $Y_{MC}/Y_{simulation}$. In this manner our final results will still be Y_{MC} as calculated above but will have the much smaller statistic error corresponding to $Y_{simulation}$.

Theoretical Cross Sections

As discussed, the simulation needs to include a cross section for the simulated processes. From our three event types to simulate – elastic electron scattering, Real Compton Scattering and neutral pion photoproduction – only elastic $p(e, e'p')$ process has a known cross section. For that reaction we use the Rosenbluth separation formula, which presents elastic scattering differential cross section as a combination of magnetic and electric form factors:

$$\frac{d\sigma}{dt} = \left(\frac{d\sigma}{dt}\right)_{Mott} \cdot \left[\frac{G_E^2 + \frac{Q^2}{2M}G_M^2}{1 + \frac{Q^2}{2M}} + \frac{2Q^2}{M}\tan^2\theta/2 \ \cdot G_M^2\right] \tag{5.12}$$

where four-momentum transfer squared is calculated as $Q^2 = 2EE'(1 - \cos\theta)$, E and E' being incident and scattered particle's energies, respectively.

[1] Notice the assumption that $A(\Omega) \equiv 1$. The convolution with this factor is essentially "naturally" performed when we apply acceptance checks at the end of the Monte Carlo loop.

The choice of cross section for RCS and pion production processes is less obvious. For RCS this is because there are no fully tested theoretical models to describe the process – hence the need of our experiment. However, as far as RCS events are concerned this is not much of a concern, since the primary method of event separation employs kinematic correlations, which for a two-body reaction is independent of cross-section's behavior. We use a constant value of RCS cross section throughout the simulation. The value of the cross section is based on theoretical calculations of Radyushkin, Diehl and Kroll based on Soft Overlap "Handbag" Mechanism. For the pion events the kinematic correlation is strongly dependent on the variation of cross section throughout the acceptance of the experiment, hence some sort of a theoretical cross section needs to be employed. The model used in the Monte Carlo simulation assumes that pion production has the same angular dependence as Real Compton Scattering, while its energy dependence is stronger by an extra factor of $1/s$, where s is one of the Mandelstam variables:

$$\frac{d\sigma_{\pi^0}}{dt} = \frac{d\sigma_{RCS}}{dt} \cdot \frac{1}{s}. \tag{5.13}$$

Here $\frac{d\sigma_{RCS}}{dt}$ is the RCS cross section evaluated using the "Handbag" Mechanism. The logic behind the extra $1/s$ factor is based on the argument that pion production diagram is essentially identical to that for RCS, with the exception that in case of pion production instead of the final photon of RCS we have a quark-antiquark pair. Using constituent quark counting rules one can argue that the extra fermion line should bring about the extra $1/s$ suppression of the cross section.

5.3.5 Event Generator

We can completely define a particular event by choosing the following four kinematic and geometric variables: scattered particle's (be it a photon, a π^0 or an electron) initial energy, recoiled proton's polar angle, recoiled proton's azimuthal angle, and the reaction vertex. From incoming particle's energy and recoil angle we can calculate also the recoil momentum. This may be somewhat counterintuitive, but instead of sampling the phase space of the scattered particle (and then calculate the recoil particle's kinematics) we sample the recoil particle. While this causes some complications – it necessitates calculations of Jacobians for the cross sections – overall this is the correct strategy: due to its decay into two photons the phase space of the π^0 is highly complicated. Hence, to avoid the necessity of applying different generation volumes for π^0 we simply do our sampling on proton's side.

First, we determine the event type: RCS, π^0, or electron. This is not done entirely randomly, but weighted by a convolution of cross sections and bremsstrahlung(for RCS and π^0) or energy loss (for electrons) distributions: before starting the Monte Carlo loop we calculate

$$f_{RCS} = \int \frac{d\sigma_{RCS}}{d\Omega} \cdot \frac{dN_\gamma}{dE_\gamma} dE_\gamma \quad , \quad f_{\pi^0} = \int \frac{d\sigma_{\pi^0}}{d\Omega} \cdot \frac{dN_\gamma}{dE_\gamma} dE_\gamma \quad \text{and} \quad f_e = \int \frac{d\sigma_e}{d\Omega} \cdot \frac{dN_e}{dE_e} dE_e$$

with these factors normalized as $f_e + f_{RCS} + f_{\pi^0} \equiv 1$. Here, the electron energy loss and bremsstrahlung are related as $\frac{dN_e}{dE}|_{E=E_e} = \frac{dN_\gamma}{dE}|_{E=(E_0-E_\gamma)}$ where E_0 is the initial (beam) energy. We choose a random number in the domain $a \in rand[0,1)$ and apply the following

condition:

$$if(a < f_{RCS}) \quad then \quad \text{event type=RCS}$$

$$if(f_{RCS} < a < f_{RCS} + f_{\pi^0}) \quad then \quad \text{event type= } \pi^0$$

$$if(a > f_{RCS} + f_{\pi^0}) \quad then \quad \text{event type=electron}$$

Once the event type has been determined, the next task is to determine the energy of the incoming particle(which may be an electron or a photon). Here we use the results of the calculation based on Eq. 5.10, which is recorded in form of an array of $(\frac{dN_i}{dE_i}, E_i)$ and of an array $\mathbf{n}_m = (\sum_{i=0}^{m} \Delta E \cdot \frac{dN_i}{dE_i}, E_m)$. The sum in $\mathbf{n}$ is essentially the integral of Eq. 5.1. This allows us to use the inverse transform method, as described in Chap. 5.2.2 in order to simulate the incoming photon's energy distribution.[2]

Next we determine two geometric variables: vertex z_{tgt} and proton's azimuthal angle. These two variables are chosen in a uniformly random manner in the domain of target size (15cm) and spectrometer's maximum known acceptance (plus an extra amount).

Finally, we have to determine the scattering angle. As mentioned before, we actually generate the proton's recoil angle rather than that of the scattered particle. To do this we first choose a value of $\cos\theta$ in a uniformly random manner. Then, we use a prepared array of $d\sigma_i(\cos\theta_i, E_i)/d\Omega$, and use interpolation to determine $d\sigma(\cos\theta, E)/d\Omega$, as well as $d\sigma_{max}(E)/d\Omega$. Once we have these numbers, we can run a rejection method Monte Carlo, as described in Chap. 5.2.1. We generate a random number $\frac{d\sigma_{max}(E)}{d\Omega} \cdot rand[0,1)$, and if the outcome is less than $d\sigma(\cos\theta, E)/d\Omega$ then we continue with this event.

[2]For the electrons we simply substitute $E \rightarrow E_0 - E$: an electron with an energy E has produced a bremsstrahlung photon whose energy is equal to the energy loss (i.e. $(E_0 - E)$) of the electron.

At this point we have determined all the defining variables of the reaction: from the above quantities we can calculate the proton's momentum, and performing two-body kinematic calculations we can determine all the kinematic variables of the scattered particle, whether it is an electron, a photon or a neutral pion.

5.3.6 External Bremsstrahlung in Air and Target material

As described in Chap. 4.4.1 the electrons are kinematically inseparable from the photons. To separate those event types, a powerful dipole magnet has been placed in front of the calorimeter. However, before being bent and separated, the electrons go through a considerable amount of air and target material, emitting bremsstrahlung photons. These photons are incident on the calorimeter, have electron's vertex kinematics, and hence, at least as far as scattering angle is concerned, are entirely inseparable from the Compton scattering photons. In other words, the central Gaussian peak observed in δx distribution consists of events which include both bremsstrahlung photons($ep\gamma$, to be short) and Compton scattering photons. There is only one criteria which betrays the $ep\gamma$ event - their energy distribution, as detected by the calorimeter, is entirely different from those of the pions and Compton events (see Chap. 4.4.2). This allows us to identify and subtract the bremsstrahlung photons from the data. The sampling of the radiative photons is done in a very similar manner to that of bremsstrahlung from the copper radiator, as described in Chap. 5.3.3, with the only difference that since the total material thickness is less than 1% of radiation length, we use the analytical calculations of Ref. [41] for an inverse transform (Chap. 5.2.2) Monte Carlo. It is assumed that the radiated photon has a trajectory which is almost perfectly parallel to

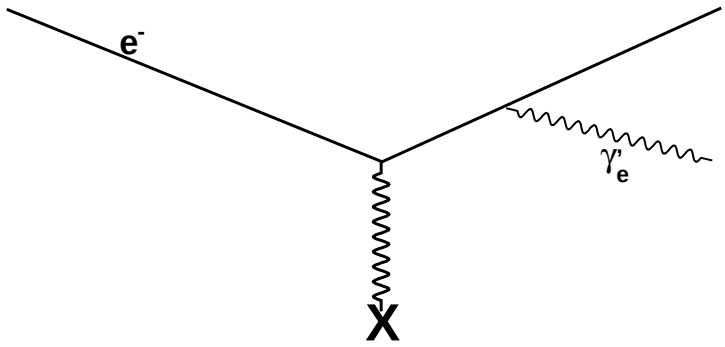

Figure 5.3: The Feynman diagram for external bremsstrahlung.

that of the electron.

5.3.7 Radiative Corrections at Reaction Vertex

Since we use elastic electron scattering on proton as a "control" data for testing experimental simulation, we need to include all other reactions related to this process. One reaction which considerably alters the simple two body kinematic dependences of elastic scattering is the internal radiation, which occurs at the hard scattering point, as can be seen in the diagram of Fig. 5.4.

The cross section of radiative corrections for $(e, e'p)$ reaction is calculated using Quantum Electrodynamics, and is very well compiled and presented in Ref. [60] and Ref. [61]. In our simulation we use the Peaking Approximation [60, pp.10-14], which is based on the assumption that the bremsstrahlung photon is emitted in a direction parallel to that of the emitter. A plot of the exact calculations of scattering angle can be seen in Fig. 5.3.7.

In Peaking Approximation the angular distribution of the emitted photon is approximated to be

$$A_{peaking}(\hat{\omega}) = \lambda_e \delta(\hat{\omega} - \hat{k}) + \lambda_{e'} \delta(\hat{\omega} - \hat{k}') + \lambda_{p'} \delta(\hat{\omega} - \hat{p}') \tag{5.14}$$

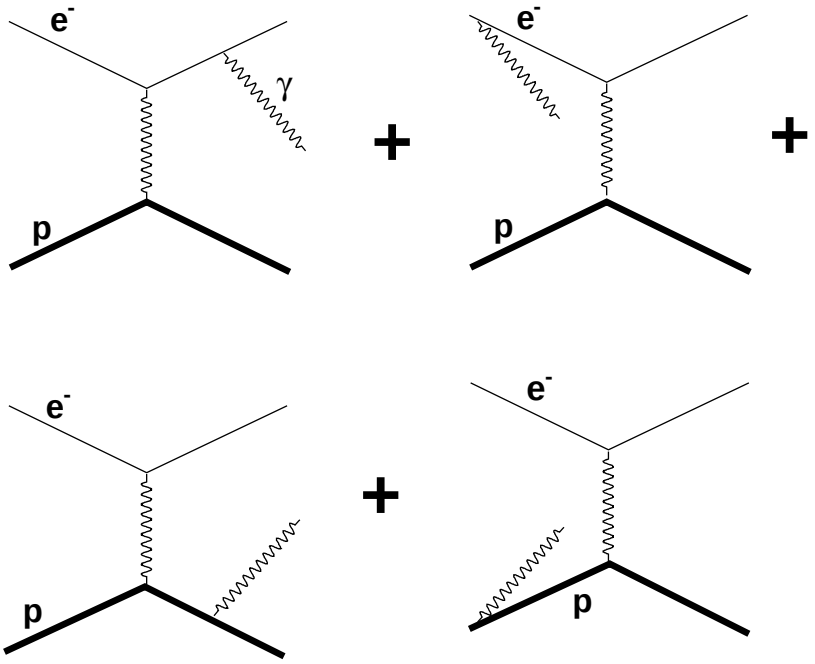

Figure 5.4: The Feynman diagram for internal bremsstrahlung.

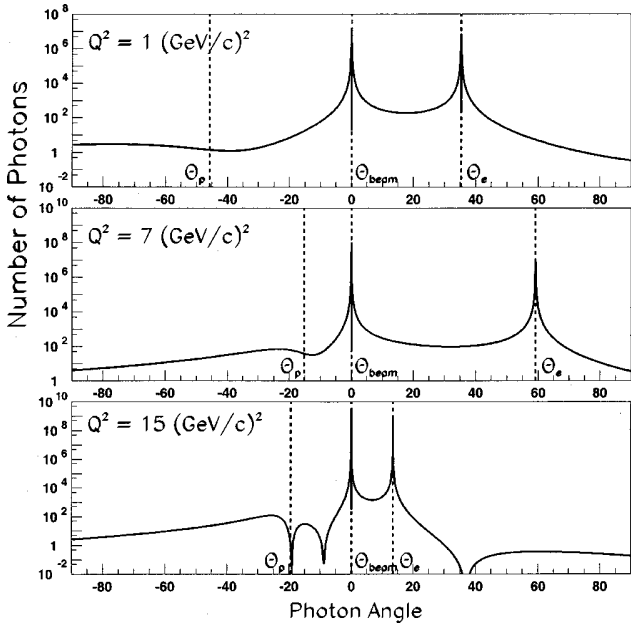

Figure 5.5: The angular distributions of radiated photons, for different values of Q^2. The abscissa is the cosine of the angle between photon's and emitting electron's direction

where $\hat{\omega}$,$\hat{k}$,$\hat{k}'$ and $\hat{p}'$ are radiated photon's, incident electron's, scattered electron's and recoiled proton's directions, respectively, while the λ-s are the corresponding relative strengths. The "typical" peaking approximation for electron bremsstrahlung gives the following values for the relative strengths:

$$\begin{aligned} \lambda_e = \tfrac{\alpha}{\pi}\left[2\cdot\ln\left(\tfrac{2|\mathbf{k}|}{m}\right)-1\right] \quad \lambda_{e'} = \tfrac{\alpha}{\pi}\left[2\cdot\ln\left(\tfrac{2|\mathbf{k}'|}{m}\right)-1\right] \\ \lambda_{p'} = \tfrac{\alpha}{\pi}\left[\tfrac{p'^0}{|\mathbf{p}'|}\cdot\ln\left(\tfrac{p'^0+|\mathbf{p}'|}{p'^0-|\mathbf{p}'|}\right)-2\right] \end{aligned} \tag{5.15}$$

a quick inspection of the above reveals that the $1/m$ term in λ_e and $\lambda_{e'}$ makes the later at least an order of magnitude larger than $\lambda_{p'}$. Since radiation is itself a correction to the elastic cross section, we could ignore $\lambda_{p'}$. The above values of λ are essentially the integrals around the peak of the photon angular distributions, as shown in Fig. 5.3.7. However, since the of-peak contribution is considerable, the relative strengths need to be corrected as follows:

$$\begin{aligned} \tilde{\lambda}_e &= \lambda_e + \tfrac{\alpha}{\pi}\left[2\cdot\ln\left(\tfrac{|\mathbf{k}|}{|\mathbf{k}'|}\right)+\ln\left(\tfrac{1-\cos\theta_e}{2}\right)\right] \\ \tilde{\lambda}_{e'} &= \lambda_{e'} + \tfrac{\alpha}{\pi}\left[2\cdot\ln\left(\tfrac{|\mathbf{k}|}{|\mathbf{k}'|}\right)+\ln\left(\tfrac{1-\cos\theta_{e'}}{2}\right)\right] \end{aligned} \tag{5.16}$$

Now that we have determined the relative strengths of radiation, all we need to do is determine the total energy loss of the particle. The cross section of energy loss is found from [60, Eq. 72]

$$\frac{d\sigma}{dE} \propto \frac{1}{E^{1-\lambda}} \quad \text{where} \quad \lambda = \lambda_e + \lambda_{e'} + \lambda_{p'} \tag{5.17}$$

The code of the simulation calculates λ, then performs an inverse transform method Monte Carlo to select E, and then splits it between the different branches with relative fractions of (λ_e/λ),$(\lambda_{e'}/\lambda)$ and $(\lambda_{p'}/\lambda)$.

5.3.8 π^0 decay

One of the most difficult aspects of our data analysis is, as discussed in Chap. 4.4.2 the subtraction of the π^0 background. Unlike the electron and photon the pion does not survive to reach the calorimeter. It decays almost instantaneously (Particle Data Group lists its life time as 8.4×10^{-17} seconds, which in laboratory frame corresponds to 25 nm), and what we observe are the resulting photons of the decay.

From kinematic point of view the pion decay is simple. The pion, a combination of $q\bar{q}$ pairs as $\pi^0 = (u\bar{u} - d\bar{d})/\sqrt{2}$, decays isotropically in its rest frame, and due to momentum conservation the photons are emitted back-to back, that is

$$\cos\theta_\gamma \in rand(0,1) \quad , \quad \phi \in rand(0,\pi) \quad \text{and} \quad E_\gamma = m_{\pi^0}/2 \tag{5.18}$$

where θ_γ is the angle between the forward-emitted photon and the initial direction of the pion,

and m_{π^0} is the pion mass. We use Lorenz transformation to go back to lab frame,

$$E_\gamma^{lab} = \gamma \cdot (E_\gamma + \beta p_{\gamma\|}) \tag{5.19}$$

where $\beta = v/c$ and $\gamma = 1/\sqrt{1-\beta^2}$. Using the expression for E_γ from above and noting that $\cos\theta_\gamma = p_{\gamma\|}/E_\gamma$ we find that

$$E_\gamma^{lab} = \gamma \cdot \frac{m_\pi}{2} \cdot (1 + \beta \cdot \cos\theta_\gamma) = \frac{E_\pi}{2} \cdot (1 + \beta \cdot \cos\theta_\gamma) \tag{5.20}$$

where in the last step we used $E_\pi = \gamma \cdot m_\pi$ as the original vertex energy of the pion. Correspondingly, the energy of the second "weaker" photon is achieved by substituting $\theta \rightarrow \pi - \theta$, which gives us

$$E_{\gamma 2}^{lab} = \frac{E_\pi}{2} \cdot (1 - \beta \cdot \cos\theta_\gamma) \tag{5.21}$$

so that the total energy is $E_{\gamma 2}^{lab} + E_{\gamma}^{lab} = E_{\pi}$, that is, the original energy of the pion.

Doing a similar calculation for the longitudinal component of momentum, we receive

$$p_{\parallel}^{lab} = \frac{E_{\pi}}{2} \cdot (\beta + \cos\theta_{\gamma}) \tag{5.22}$$

from where we can calculate the photon's relative angle to the pion's original direction:

$$\cos\theta_{\gamma}^{lab} = \frac{p_{\parallel}^{lab}}{E_{\gamma 2}^{lab}} = \frac{\beta + \cos\theta_{\gamma}}{1 + \beta \cdot \cos\theta_{\gamma}} \tag{5.23}$$

For example, when the photon is emitted in the direction parallel to that of the original pion, we get $\cos\theta_{\gamma}^{lab} = \cos\theta_{\gamma} = 1$, as expected.

So, as we saw, the simulation of pion decay essentially consists of sampling the following variables

$$\begin{aligned} \cos\theta_{\gamma 1}^{lab} &= \tfrac{\beta+z}{1+\beta\cdot z} \qquad E_{\gamma 1}^{lab} = \tfrac{E_{\pi}}{2} \cdot (1 + \beta \cdot z) \\ \cos\theta_{\gamma 2}^{lab} &= \tfrac{\beta-z}{1-\beta\cdot z} \qquad E_{\gamma 2}^{lab} = \tfrac{E_{\pi}}{2} \cdot (1 - \beta \cdot z) \end{aligned} \tag{5.24}$$

where $z \in rand(0,1)$ is a randomly chosen number between 0 and 1.

5.3.9 High Resolution Spectrometer

As mentioned above, the complicated nature of our experiment's acceptance is explained by the complex magnetic and geometric structure of the Hall A High Resolution Spectrometer. The spectrometer has a quadrupole-quadrupole-dipole-quadrupole configuration, with different slits and apertures in-between the optical-magnetic elements. While the non-magnetic parts of the spectrometer can be reduced to simple linear transformations and *if() then* statements in the code, the magnetic parts are much more complicated. This is however not a new problem, since the design and construction of particle accelerators demands a

good understanding of beam dynamics in magnetic elements. Over the years a number of software packages have been developed which use differential algebra in order to numerically calculate the transformation matrices for the optic system of the magnetic elements, the most notable of those packages being COSY [62]. This package, in combination with known HRS geometries and optic studies has been used to develop a magnetic model for the spectrometer.

COSY uses Taylor expansions in order to describe the magnetic system to determine the trajectories of particles. The input into COSY consists of geometric measurements of the magnetic elements – quadrupoles and dipole – as well as actual field measurements which were performed during Hall A commissioning. Most importantly, these measurements included studies of fringe fields at the non-flat entrance and exit faces of the dipole. The inclusion of the known values increases the accuracy of the magnetic model. The output of the software is presented as a set of transformation matrices which then can be used to calculate the exit values of the trajectories based on their entrance values. A number of recent experimental studies have been performed to minimize the error on transformation matrices by studying the relative alignment of the quadrupoles [63] and to understand the source of the remaining uncertainties [64].

The COSY magnetic model for Hall A left High Resolution Spectrometer has been used by previous experiments to develop a Monte Carlo package, called SIMC [65], which contains different types of event generators, target types, as well as the left and right spectrometers (lHRS and rHRS). Due to a previously known reliability of COSY based codes, it was decided to use the SIMC simulation for the spectrometer as part of our general Monte Carlo.

After the event generator produces a particular event, the variables corresponding to the photon arm are used to check whether the event entered calorimeter's acceptance (which is simulated as a simple square). After this, the proton vertex variables are presented as an input to SIMC's mc_hrsl.f module. The event is then transported through vacuum toward the first quadrupole, and a check of entrance window and quadrupole entrance is performed. If passed, the event is then transported to the 2/3 of the length of the quadrupole, where it is again checked for being inside the quadrupole radius[3]. Afterwards, it is transported through the rest of the quadrupole, then transported through vacuum, where it is checked for apertures, after which it finally reaches the next quadrupole. This process is performed repeatedly until the event reaches the detector hut of the spectrometer, where its values are "smeared" by a Gaussian distribution of 0.275 mm standard deviation in order to reproduce the VDC resolution. Once this is done, the focal plane variables are used to reconstruct the vertex variables.

5.4 Data Analysis: Elastic Electron Scattering

As mentioned before, a particular simulation or numerical model needs to be tested before being used for determining experimental results. To test the simulation, one needs some sort of "controlled data" – a data which is extracted from a process with simple event structure, known kinematic dependences and known cross sections.

[3]Using GEANT simulations and independent calculations it has been established that the beam envelope reaches its maximum radius at 2/3 of a quadrupole length. COSY has been used to perform two calculations: one for the first 2/3 of the quadrupole, and second for the last 1/3

A reaction which perfectly satisfies these conditions is elastic electron scattering on proton. Besides having a known cross section, the target needed for observing this process is identical to that of Compton scattering, with the only difference that Compton scattering also requires a radiator in order to produce a photon beam. To collect elastic electron data the radiator is removed, and the spectrometer-calorimeter configuration is changed so that the combined acceptance is centered on the beam energy. Due to high beam currents of $> 40\mu A$ the data collection takes very short time.

One of the deficiencies of of elastic scattering (or any other two-body process) when used for the above mentioned purpose is that its momentum is correlated with its scattering angle. This causes a non-uniform illumination of the HRS focal plane. The reason this is so is because $x_{fp} \sim p$ and $y_{fp} \sim \theta$, where x_{fp} and y_{fp} are the vertical and horizontal coordinates of the particle at the focal plane. The result of these correlations is that the data illuminates only the diagonal of the focal plane. This may leave large areas of focal plane untested. To eliminate this problem, we change the central momentum of the spectrometer in order to shift the diagonal up and down the plane. The resulting illumination can be seen in Fig. 5.6.

The data sets corresponds to spectrometer central momentum values of $1.788\,GeV$, $1.762\,GeV$, $1.711\,GeV$, $1.681\,GeV$, $1.661\,GeV$, $1.637\,GeV$. Spectrometer is rotated to an angle of 33.97^0 to the beam, while the calorimeter is placed at an angle of 46^0 and distance of $12m$ from the target. A thorough comparison between data and Monte Carlo can bee seen in Fig 5.4, showing an excellent agreement. A list of comparisons among the other five runs can be seen in Fig. 5.8

While the qualitative comparisons between the data and Monte Carlo look encouraging,

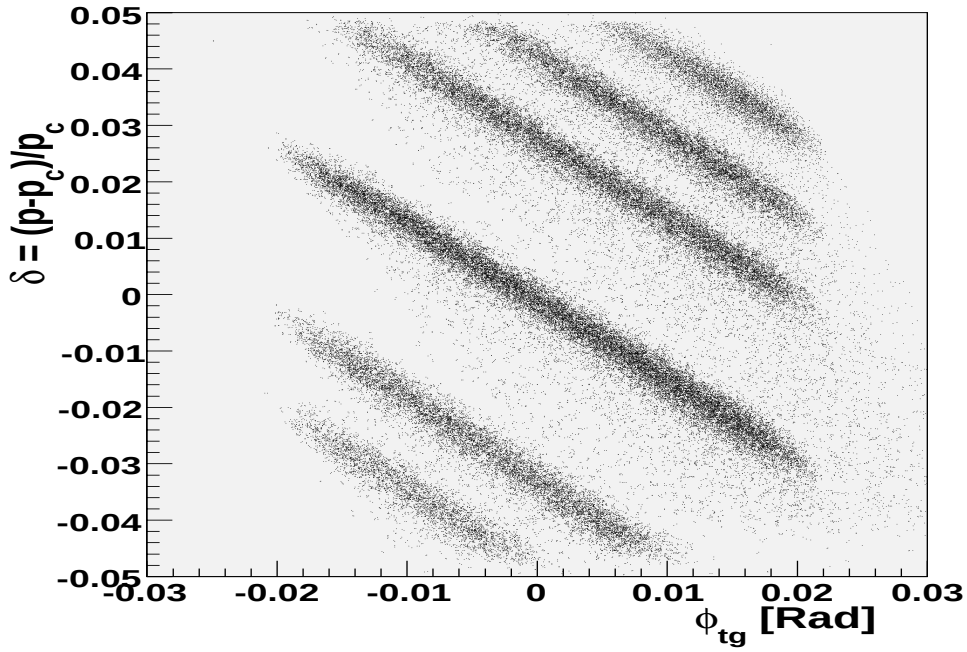

Figure 5.6: The momentum vs. angle distribution for the data set from acceptance scan runs.

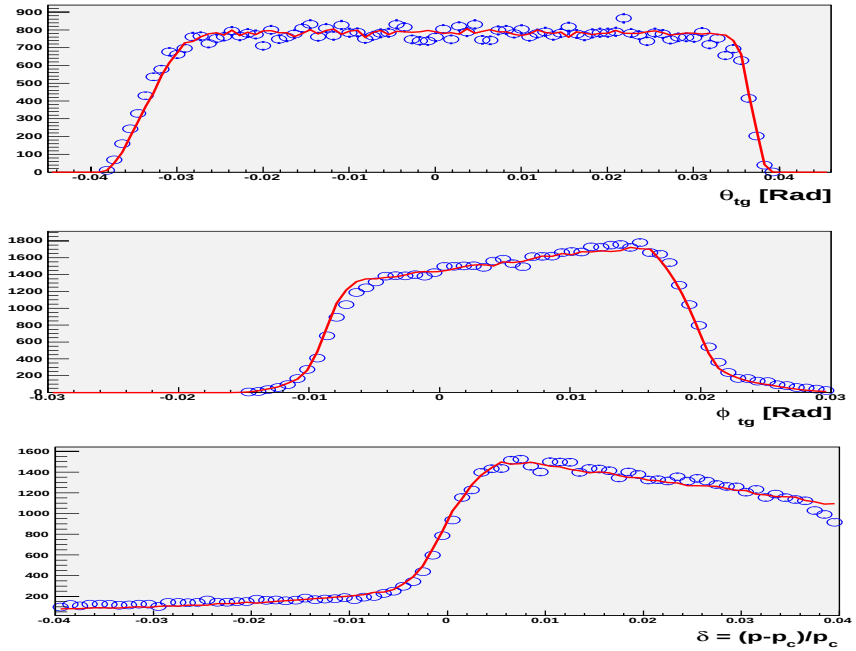

Figure 5.7: Comparison of data and Monte Carlo for run 1635. Monte Carlo corresponds to red circles, data corresponds to blue circles.

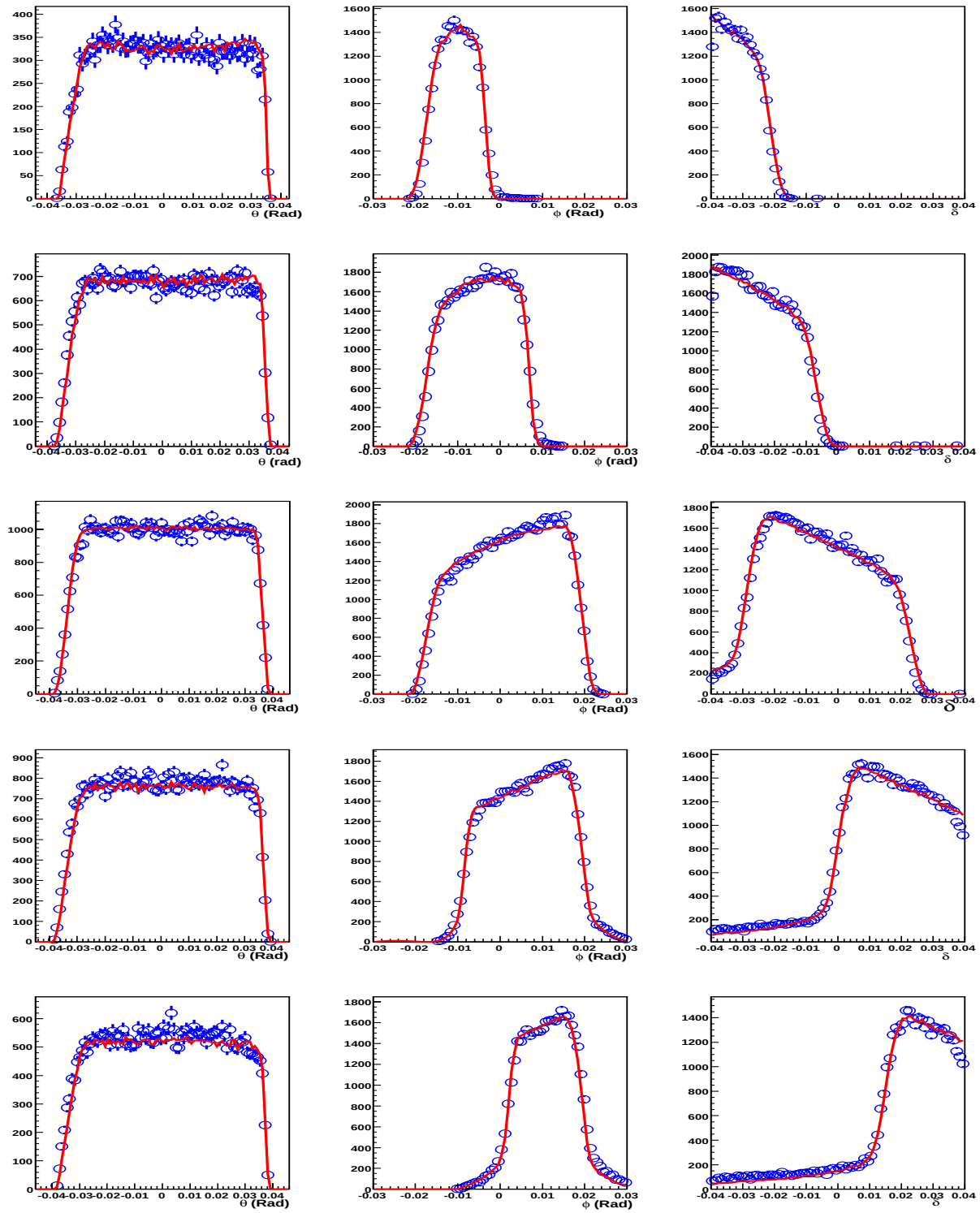

Figure 5.8: $2a$ **scans, momentum(from top to bottom)** – $1.788 Gev/c$, $1.762 Gev/c$, $1.711 Gev/c$, $1.661 Gev/c$, $1.637 Gev/c$.

it is however important to perform a quantitative analysis in order to determine the actual precision of the simulation. To do this we use the elastic data to determine elastic scattering cross section, which we then can compare with the known values. The previously known value of cross section, as extracted from literature [66] [21], is

$$\frac{d\sigma}{d\Omega} = 0.52 \text{ nBarn/sRad}$$

Despite containing a rather clean event structure, the data still contains a significant number of events from $e\ p \rightarrow e\ p\ \pi^0$ neutral pion electro-production. It is not however very difficult to eliminate these: unlike elastic electron events, the pion events, just as in production data, do not produce a correlation between left and right arms. To clean the data from background noise, from π^0 events and other backgrounds, we place the following cuts:

Event type 5 – insures electronic coincidence between the two arms.

$\mathbf{E_{calo} > 600}$ – cut on calorimeter energy, to eliminate low energy background.

abs(fg_gc_gx) < 36 and abs(fg_gc_gy) < 56 – remove the last row of peripheral calorimeter blocks, to insure an area of reliable calibration.

abs(calo_x) < 36 and abs(calo_y) < 56 – same for the reconstructed calorimeter variables, to reduce π^0 background.

$\mathbf{abs}(\delta\mathbf{x} - \delta\mathbf{x_0}) < \mathbf{2}\sigma_\mathbf{x}$ **and** $\mathbf{abs}(\delta\mathbf{y} - \delta\mathbf{y_0}) < \mathbf{2}\sigma_\mathbf{y}$ – place a 2σ cut on the $\delta x \delta y$ distribution, to further reduce the number of the pions, as discussed above. This will result in a loss of 10% of the elastic (e, p) events, a factor which is taken into account in the final comparison.

run	p_0 [GeV/c]	Live Time	Acc. Charge [mC]	Ratio
1630	1788	0.91	11.60	1.005 ± 0.007
1632	1762	0.92	12.60	0.995 ± 0.005
1611	1711	0.91	10.72	1.01 ± 0.007
1635	1661	0.91	9.79	1.004 ± 0.004
1636	1637	0.92	9.33	1.01 ± 0.005
1637	1614	0.91	9.05	0.99 ± 0.01

Table 5.1: Ratio of observed and measured (e,p) cross sections

abs(δ) $<$ **4**% – a cut on momentum. As a result of data-Monte-Carlo comparisons it has been discovered that there are very strong disagreements in the region of $abs(\delta) > 4\%$. This is mostly due to the fact that the mc_hrsl.f module, due to a number of reasons related to the functionality of COSY model for non-flat magnets, doesn't contain any acceptance checks inside the dipole magnet. Meanwhile, in real life a large volume of events are "lost" when they hit the bottom and top of the magnet. This cut causes a negligible loss – less than 10% – of statistic volume.

The achieved final results can be seen in Table 5.1. We conclude that the Monte Carlo simulation reproduces the elastic data to within 1% of its known value, and that the variations of determined cross section across the HRS acceptance are less than $(2 \pm 1.2)\%$.

Chapter 6

Data Analysis with Monte Carlo Simulations

6.1 Production Data

Once the analysis of "controlled" data is complete, we can confidently proceed with the production data – that is, the data which contain the actual process of interest, Real Compton Scattering. In this chapter we will discuss in detail the analysis procedure for only one kinematic point – 3C. The other kinematic points have an analysis procedure either identical or very similar to that of 3C. See Table 6.4 for the experimental settings of this point. Through the plots in this section, the data is denoted by the blue dots with error bars, while red lines correspond to the simulation.

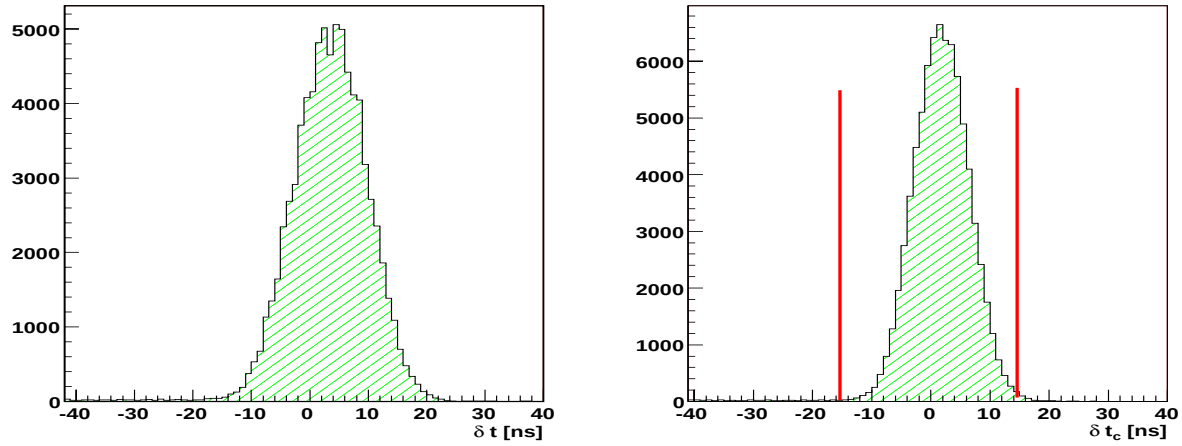

Figure 6.1: Uncorrected (left) and corrected (right) coincidence time distributions,after extensive cuts on calorimeter energy and other kinematic variables. The red lines denote the timing cut used in the analysis.

6.1.1 Kinematic point 3C: Event Separation and Extraction of Yields

As mentioned earlier, the variables which allows us to separate the events from different processes are δx and δy, which are defined as

$$\begin{aligned} \delta x &= x_p \ - \ x \\ \delta y &= y_p \ - \ y \end{aligned} \tag{6.1}$$

where x and y are the particle's horizontal and vertical hit coordinates, as detected by calorimeter, and x_p and y_p are the predicted coordinates calculated from proton's kinematic variables as detected by the spectrometer. Since we need to reduce the pion decay background as much as possible, and since the correlation achieved by pion decay events is much broader than that of RCS events , we place a narrow (approximately $3 \cdot \sigma_y$) cut on the δy variable, after which we plot the event distribution of δx variable. The resulting plots can be seen in

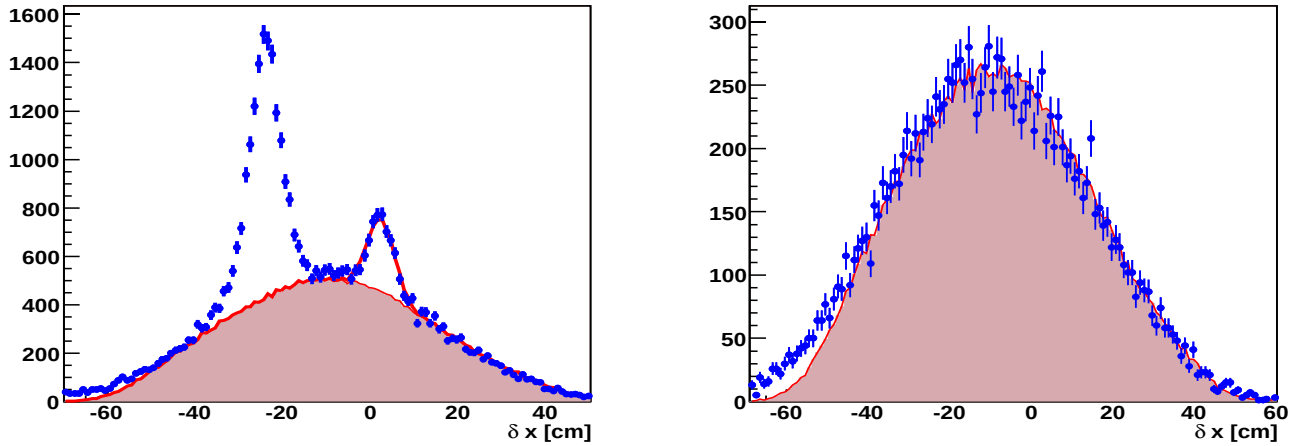

Figure 6.2: Left: δx distribution with $\mathbf{abs}(\delta\mathbf{y} - \mathbf{3}.) < \mathbf{15}$. Right: same, with $\mathbf{abs}(\delta\mathbf{y} - \mathbf{3}.) > \mathbf{15}$, showing the pion distribution.

Fig. 6.2

The set of the cuts, which we will call *cut1* is presented below:

Event type == 5: Insure coincidence between the two arms.

$\mathbf{abs}(\delta\mathbf{t} + \delta\mathbf{p} \cdot \mathbf{200} - \mathbf{650}) < \mathbf{15}$**:** Cut on coincidence time, which shows a signal at ≈ 0 and random noise background underneath. The $\delta p \cdot 200$ correction is done to correct for different flight times for events which crossed different parts of the HRS dipole and hence had different flight distances (See Fig. 6.1 for comparisons between corrected and uncorrected coincidence times).

$\mathbf{abs}(\mathbf{z_{tgt}}) < \mathbf{6}$**:** Cut on target length, to remove possible background from the end-caps (aluminum walls) of the target.

$\mathbf{abs}(\delta\mathbf{p}) < \mathbf{4\%}$**:** Cut on spectrometer momentum, to remove MC-data disagreements at the edges of the momentum acceptance. Here $\delta p \equiv (p - p_{central})/p_{central}$, where $p_{central}$ is

the central momentum of HRS.

$\mathbf{E_{calo} > 700}$: Cut on calorimeter energy, to remove low-background noise.

$\mathbf{abs(\delta y - 3.) < 15}$: Cut on δy variable, to reduce the pion background and thus to increase the signal-to-noise ratio. The $-3.$ term in the parentheses is the vertical offset of the calorimeter positioning, which translates into an offset in δy.

$\mathbf{abs(x_{calo}) < 36}$ AND $\mathbf{abs(y_{calo}) < 56}$: Cuts on calorimeter hit position, to remove the peripheral rows and columns of the calorimeter, known to have a rather poor calibration.

$\mathbf{E_\gamma > 3000}$ AND $\mathbf{E_\gamma < 3300}$: Cut on incoming energy.

In addition to the above set of cuts, we use a second set of cuts, called *cut2*, which is identical to *cut1* with the the only difference of $\mathbf{abs(\delta y - 3.) > 15}$. The purpose will be clear soon. The resulting δx distributions of the data can be seen as the blue dots of Fig. 6.2. A two-dimensional scatter plot of the experimental data can be seen in Fig. 6.3(a).

Pion Background: kinematic correlations and coordinate-energy dependences

Once we have applied these cuts on the data, we do exactly the same for Monte Carlo – both for Compton and pion events. At this point we can start working on pion background subtraction. To do this, we need to place additional cuts which will isolate the pion events, as in *cut2* – by placing an "anti-cut" on the kinematic correlation, we have eliminated all electron, Compton and $ep\gamma$ events. So, the combination of cuts is { *cut2* $\times(\delta x > -15)$cm } + { *cut1* $\times(\delta x > 10)$cm }, and a δx vs. δy plot of the resulting events is shown in Fig. 6.3(b).

Finally we can determine the K_π coefficient of Eq. 5.4:

$$K_\pi = n_\pi / n'_\pi \quad \text{and} \quad \frac{d\sigma_\pi}{dt} = K_\pi \cdot \frac{d\sigma'_\pi}{dt} \tag{6.2}$$

where n_π is the number of counts under the above mentioned cut, and all primed variables correspond to Monte Carlo output or input. K_π is the factor by which the input cross section underestimates the real cross section, and indicates by how much we need to scale our Monte Carlo output to fully reproduce the pion background.

The plots of the data volume which was used above to determine the pion background can be seen in the two dimensional plots of Fig. 6.3. The left plot is the general event distribution, showing the electron and RCS peaks superimposed on pion decay continuum. The plot on the right is the event volume used to determine the Monte Carlo to data normalization. The projections of Fig. 6.3 (b) on δx and δy axes can be seen in Fig. 6.4, showing a solid agreement between the experimental data and the simulation.

Besides studying the δx and δy distributions for the pion background, we can also look on two important variables: energy of the photons from pion decay, either as measured by the calorimeter, or as calculated using the pion kinematics. The first variable, which we will simply denote as E_{calo}, can be observed simply by placing the above mentioned cuts. The second variable can be calculated in the following manner: from proton kinematics calculate the pion energy, and then determine the final photon energy using Eq. 5.24,

$$E_{\gamma 1}^{lab} = \frac{E_\pi}{2} \cdot (1 + \beta \cdot z) \quad \text{where} \quad z \equiv \cos(\theta_{CM}) \tag{6.3}$$

θ_{CM} being the pion decay angle in its rest frame. Using Lorentz transformations z can be

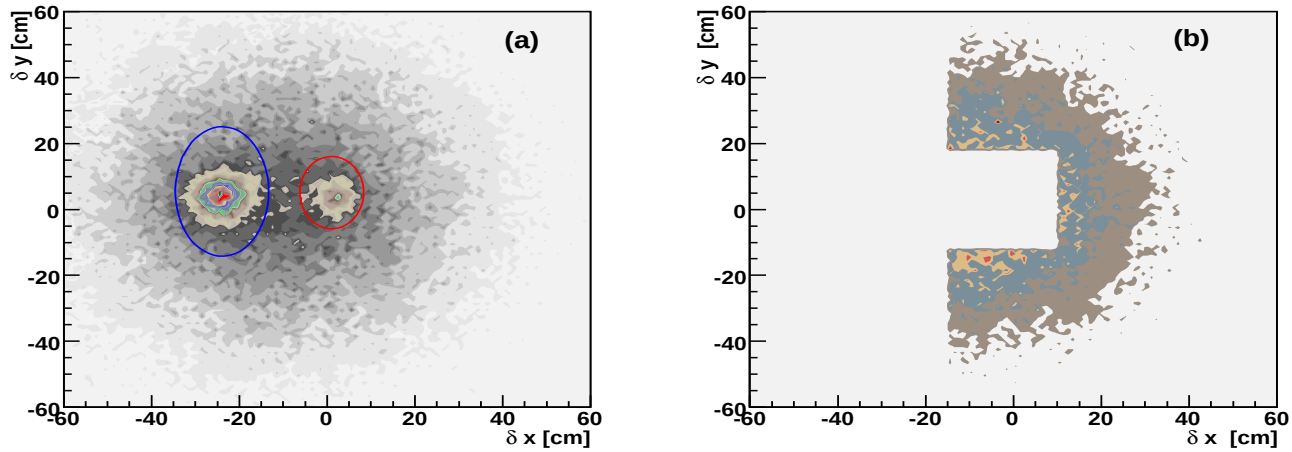

Figure 6.3: a) general event distribution. Blue circle marks the electron distribution, and red circle marks the RCS event distribution. b) events extracted as a result of the cuts used in Eq. 6.2, and later used for determining the pion background normalization

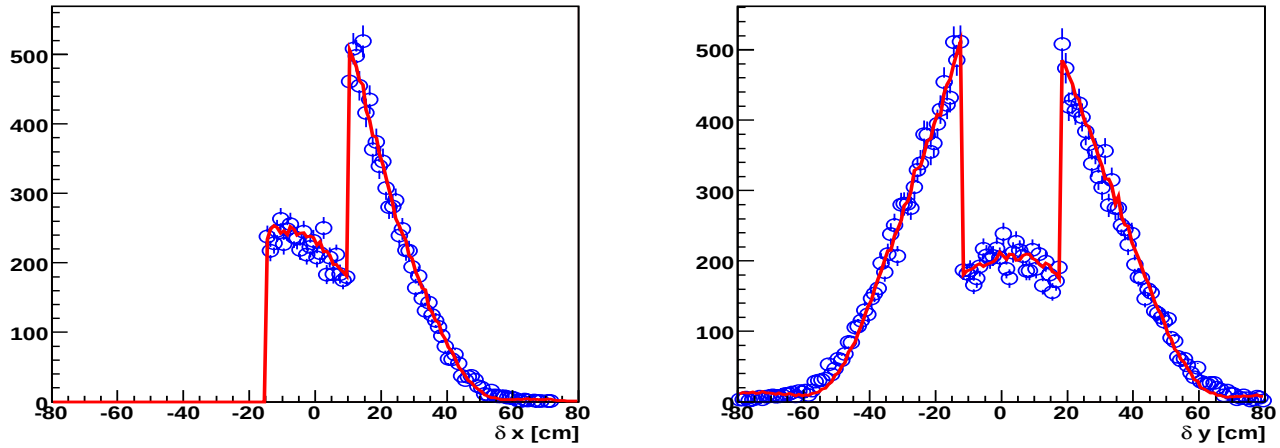

Figure 6.4: Events from Fig. 6.3(b) projected on δx and δy axes. Simulation is denoted by red line, while the blue circles represent data.

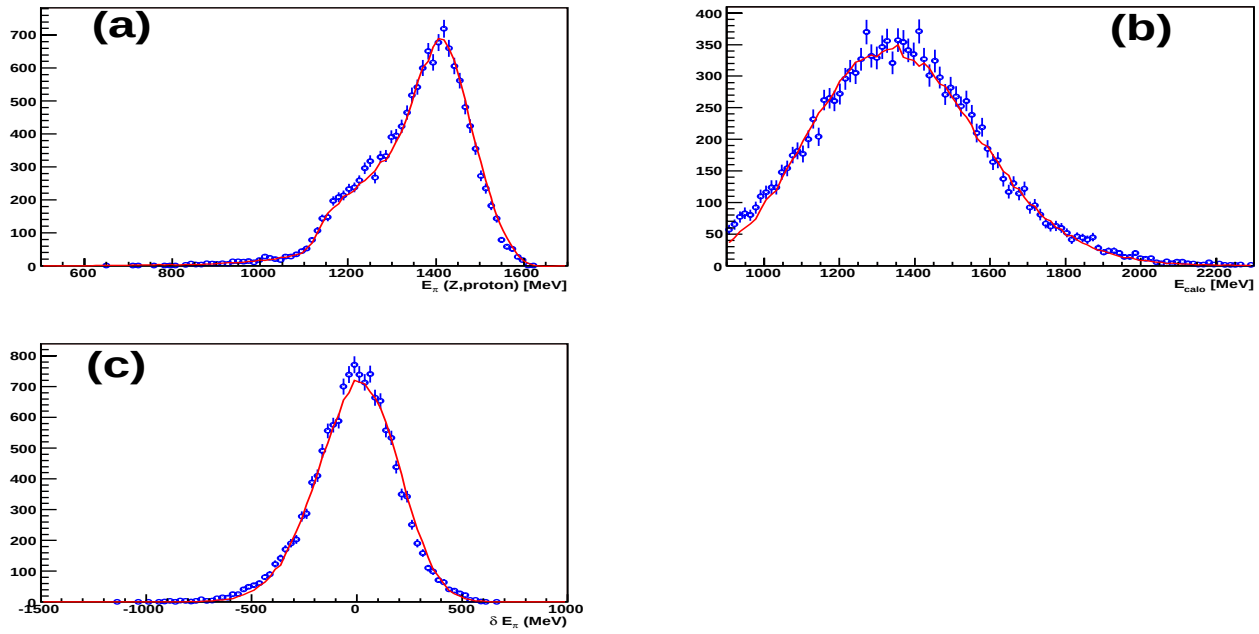

Figure 6.5: In all following plots the simulation is denoted by a red line: a) The energy of π^0 decay photon, as calculated from proton's kinematics and photon calorimeter coordinate, using Eq. 5.24; b) The energy of π^0 decay photon, as measured in the calorimeter; c) the difference of the previous two quantities.

found as

$$z = \frac{r_0^2 - r^2}{r_0^2 + r^2} \quad \text{where} \quad r_0 = D \cdot \frac{m_\pi}{E_\pi} \quad \text{and} \quad r^2 = \delta x^2 + \delta y^2 \tag{6.4}$$

Here D is the distance to the calorimeter, while m_π and E_π are pion's mass and total energy, respectively. The resulting distribution of pion decay photon's energy, measured and computed as discussed before, can be seen in Fig. 6.5. The closeness of simulation to the experimental data is another proof that the neutral pion background is well understood and that the simulation contains a complete description of that process.

Once corrected by K_π, the Monte Carlo output can be seen in Fig. 6.2 (left), where it is compared with the experimental data. Also, Fig. 6.2 (right) shows the same distribution with the $\mathbf{abs}(\delta\mathbf{y} - \mathbf{3.}) > \mathbf{15}$ "anti-cut"(*cut2*), which in purpose isolates the pion events, allowing

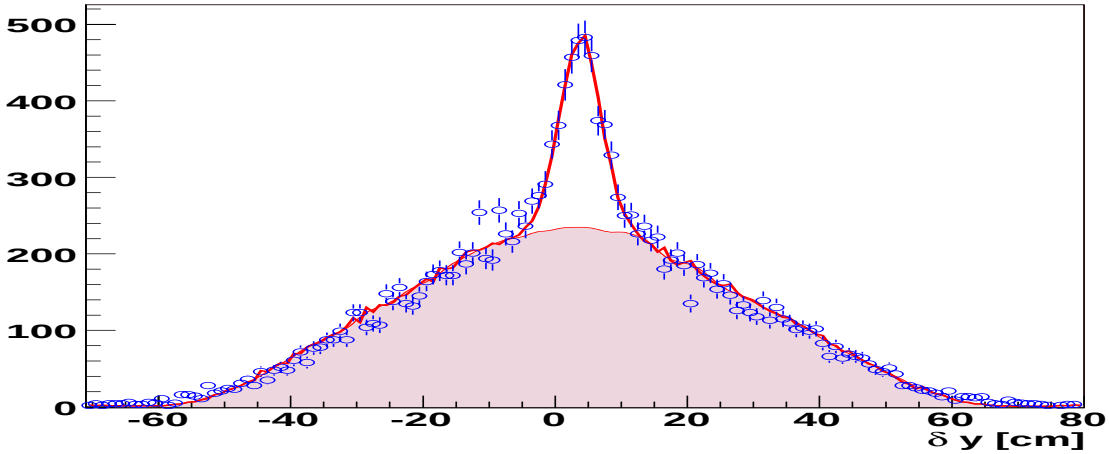

Figure 6.6: Left: δy distribution with $\mathbf{abs}(\delta \mathbf{x} - \mathbf{2.}) < \mathbf{8}$.

a full data-to-Monte-Carlo comparison. This is another test which shows that the Monte Carlo can reproduce the data very well in the [-40,60]cm domain, where our signal is located.

Pion Background: Co-planarity correlation

Before proceeding to the next stage of the analysis, we would like to look at another variable – the co-planarity correlation δy, as defined in Eq. 6.1. The count distribution is plotted Fig. 6.6. The peak at $\delta y \approx 0$ are the RCS and $ep\gamma$ events, while the continuum beneath are the neutral pion decay events. This is a very revealing test, since the δy distribution is dependent solely on the combination of acceptance and pion decay's simple kinematics. The fact that we have such a good agreement between the simulation and data is indicative to simulation's completeness.

Pion Background: incoming energy dependence

The δx and δy distributions for electron, RCS and $ep\gamma$ events is defined entirely by offsets caused by the magnet as well as resolution effects. However, the situation is quite different for the pions. The strong left-right arm correlation for the pion is diluted by its decay photon distributions, which is isotropic in pion's rest frame, and quite broad in laboratory frame. The decay process weakens the otherwise strong correlation. This makes the δx distributions very broad for pions and strongly dependent (as mentioned earlier) on acceptance effects. This circumstance makes the δx distribution also dependent on pion production differential cross sections. The difficulty of simulating pion production then becomes obvious: unlike such other processes as elastic electron scattering, there are no complete and tested theoretical models which describe the dependence of pion photoproduction cross sections on angle and energy. The only model which is available predicts that neutral pion photoproduction cross section should vary as

$$\frac{d\sigma_{\pi^0}}{dt} \propto \frac{1}{s} \cdot \frac{d\sigma_{RCS}}{dt} \tag{6.5}$$

However, as previous and actual (see Table 6.3 measurements show, this is not always correct.

The solution to the problem is then the following: since we can isolate the π^0 events, we can also study their incoming energy (which is reconstructed from proton's kinematic variables), and observe whether the Monte Carlo simulation matches the experimental data. If not, further $1/s^n$ weights need to be applied to achieve a best fit. To illustrate, the results of two kinematic points are brought in Fig. 6.7. The plot in Fig. 6.7(left) is for kinematic point 3C, while Fig. 6.7(right) is for kinematic point 5E. Both plots show the Monte Carlo simulation with and without scaling. For 3C an $1/s^n$ as prescribed by Eq. 6.5 has been

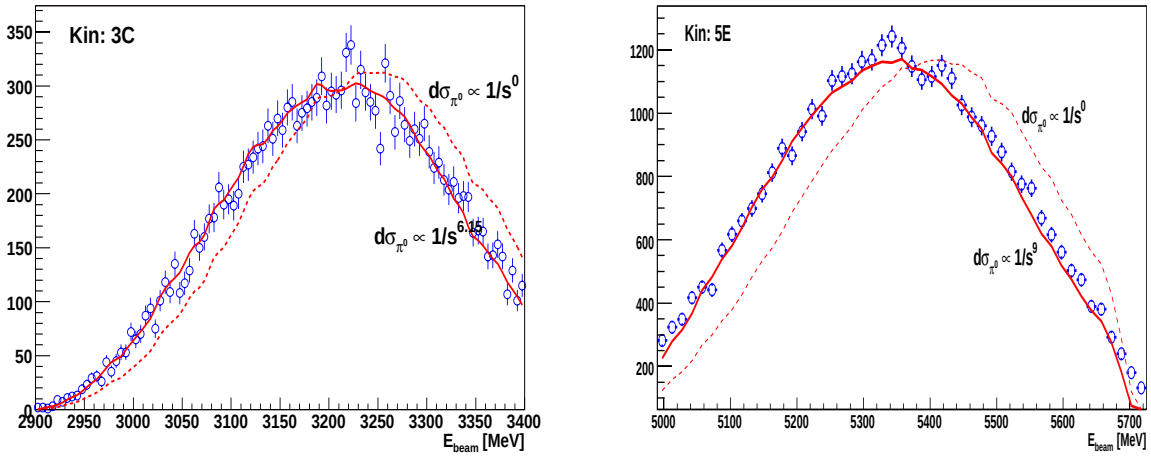

Figure 6.7: Energy dependences of neutral pion photoproduction for 3C(left) and 5E(left) kinematic points. Blue circles denote the data, full lines denote simulation with a non-constant cross section, and doted lines denote simulation with a constant cross section.

applied. For 5E an exponent of $n = 9$ for $\frac{d\sigma_{\pi^0}}{dt} \propto \frac{1}{s^n}$ has been selected, showing a resulting robust agreement with the experimental data.

Bremsstrahlung Photon background and Real Compton Scattering cross section

At this point we can move on to the next task – determining K_{rcs} and $d\sigma_{rcs}/dt$. As mentioned in previous chapters, we cannot simply use the same method in δx distribution as we did for the pions: the Gaussian in Fig 6.2(left) contains both Compton and bremsstrahlung photon events. As mentioned earlier, the electrons, before being deflected by the magnet, interact with target material and air, producing bremsstrahlung radiation which is directed parallel to electron's direction, and has an energy of $E_0 - E'$, where E_0 and E' are the electron's original and final energies, respectively. This makes the bremsstrahlung photons angularly(that is, in δx and δy) indistinguishable from the Compton events. The only manner to distinguish them is to look at the energy of the particle, as registered by the calorimeter. To do this,

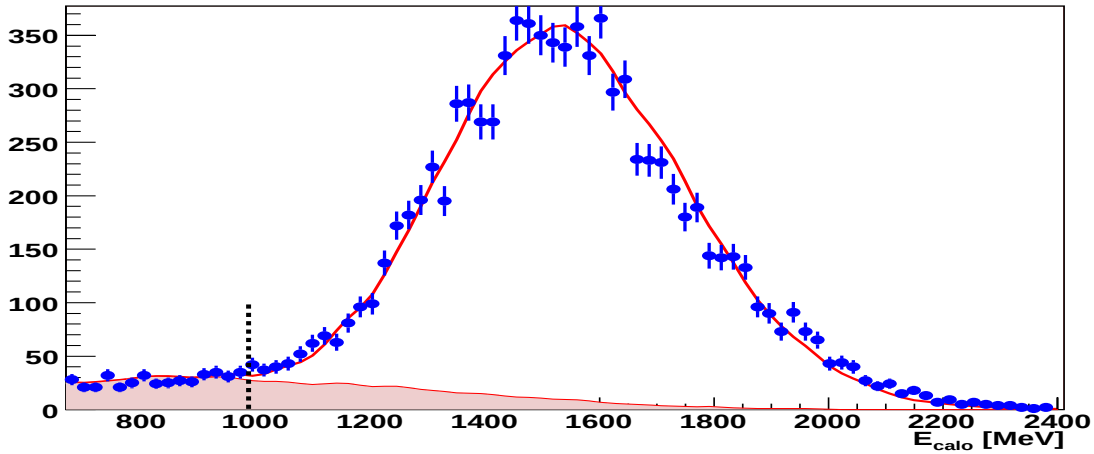

Figure 6.8: E_{calo} distribution with $\mathbf{abs}(\delta\mathbf{x} - \mathbf{2}.) < \mathbf{8}$. The punctured line denotes the cut used to isolate the $ep\gamma$ background.

we observe the count distribution with a combination of cuts $\{$*cut1* AND $\mathbf{abs}(\delta\mathbf{x} - \mathbf{2}.) < \mathbf{8}$ $\}$. Resulting distribution can be seen in Fig. 6.8 as the blue points.

This distribution contains in itself three event types: Compton (RCS), bremsstrahlung ($ep\gamma$), and pions. The number of the counts corresponding to the later we can find out easily: it is $N_\pi = N'_\pi \cdot K_\pi$, where as always priming corresponds to the simulation output. The only other event type left are the $ep\gamma$. We however can separate those by observing the low E_{calo} "tail" of the count distribution. All we have to do is place a cut which will eliminate everything except the bremsstrahlung events: $E_{calo} > 700 \text{and} E_{calo} < E_{peak} - 3 \cdot \sigma_E$, where E_{peak} is the peak value of the distribution, and σ_E is the standard deviation of the Gaussian fit to the $E_{calo} > E_{peak}$ part of the distribution. This way, by isolating the $ep\gamma$ events, we can determine the coefficient K_γ, which indicates by how much the simulation underestimates or overestimates the volume of bremsstrahlung:

$$K_\gamma = \frac{n_\gamma}{n'_\gamma} \tag{6.6}$$

where n_γ is the number of data counts under the above mentioned cut, and n'_γ is the same number but for simulation.

Finally, we move under the domain of $E_{calo} > E_{peak} - 3 \cdot \sigma_E$, where we can now subtract the bremsstrahlung and pion events, and determine K_{rcs}:

$$K_{rcs} = \frac{N - K_\pi \cdot N'_\pi - K_\gamma \cdot N'_\gamma}{N'_{rcs}}$$

where N is the total number of data counts under the $E_{calo} > E_{peak} - 3 \cdot \sigma_E$ cut, and the primed values of N are the counts of simulated output. A more explicit expression can be achieved using the values of K_π and K_γ –

$$K_{rcs} = \frac{N - n_\pi \cdot (\frac{N'_\pi}{n'_\pi}) - n_\gamma \cdot (\frac{N'_\gamma}{n'_\gamma})}{N'_{rcs}} \tag{6.7}$$

Assuming that the statistical error of the simulation is negligible, we calculate the statistic uncertainty of K_{rcs}:

$$\delta^2_{rcs} = (\frac{\partial K_{rcs}}{\partial N} \cdot \delta_N)^2 + (\frac{\partial K_{rcs}}{\partial n_\pi} \cdot \delta_\pi)^2 + (\frac{\partial K_{rcs}}{\partial n_\gamma} \cdot \delta_\gamma)^2$$

which gives us

$$\delta_{rcs} = \frac{1}{N'_{rcs}} \sqrt{N + n_\pi \cdot \left(\frac{N'_\pi}{n'_\pi}\right)^2 + n_\gamma \cdot \left(\frac{N'_\gamma}{n'_\gamma}\right)^2} \tag{6.8}$$

Table 6.1 lists the values of the above numbers.

The final results for the remaining kinematic points are presented in the Table 6.3.

Stability of Results Under Acceptance Cuts

As part of our systematic checks, we need to observe the stability of our final results under different conditions. One of these check is to place different cuts on calorimeter face, and

n_π	20802	n_γ	291
n'_π	9708	n'_γ	92.
K_π	2.143	K_γ	3.172
N	8632		
N'_{rcs}	967.		
K_{rcs}	1.565		
$\frac{d\sigma'_{rcs}}{dt}$	0.1651 nB/GeV^2	$\frac{d\sigma'_\pi}{dt}$	7.70 nB/GeV^2
$\mathbf{\frac{d\sigma_{rcs}}{dt} = \frac{d\sigma'_{rcs}}{dt} \cdot K_{rcs}}$	**0.258** nB/GeV^2	$\mathbf{\frac{d\sigma_\pi}{dt} = \frac{d\sigma'_\pi}{dt} \cdot K_\pi}$	**16.5** nB/GeV^2
δ_{rcs}	0.02 nB/GeV^2	δ_π	0.1 nB/GeV^2

Table 6.1: Table of numerical values used in the analysis process. The primed variables are those produced by the simulation for an accumulated beam charge of $1mC$.

observe dependences of RCS cross section on these cuts. Fig 6.9 shows that the results are very stable under different cut conditions. The numerical results are also listed in Table 6.1. The stability of the results under varying acceptance cuts is yet another successful test of simulation's good reproduction of experimental acceptance.

Systematic Uncertainties due to Bremsstrahlung Background

Another possible source of systematic uncertainties is the presence of the $ep\gamma$ background. The manner in which this background is subtracted has been discussed earlier. However, it was done assuming that all of the observed background consists of bremsstrahlung photon events, or more precisely – it follows the general shape of bremsstrahlung background. By default this does not have to be so – it is hard to a priori exclude the possibility that other

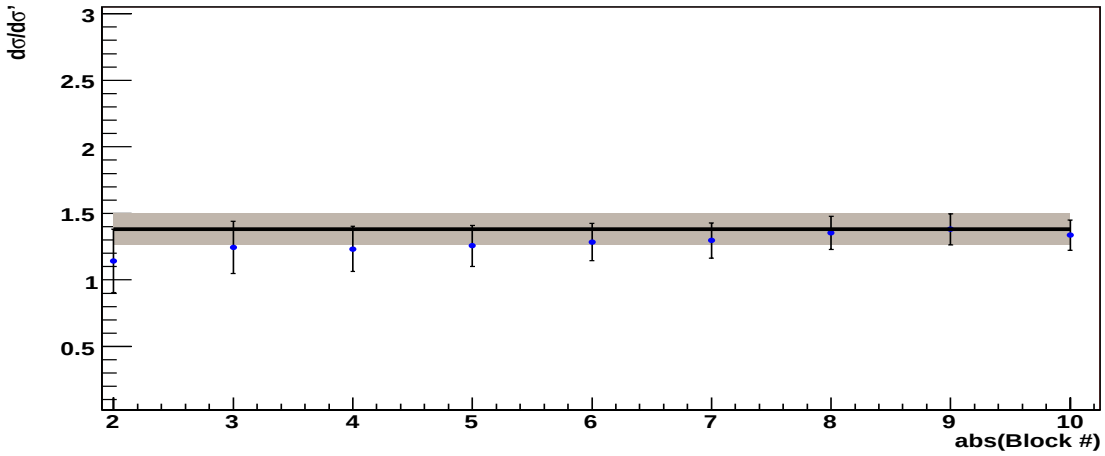

Figure 6.9: Dependence of absolute cross section on calorimeter cuts. The ordinate is presented as the ratio of cross section to a constant cross section supplied to the Monte Carlo simulation. The line and the gray error band represent our final result.

sources of background could be present. To investigate this we can use the electrons in the experimental data. In our simulation of off-endpoint kinematic points the normalization of electron yield is arbitrary. However, the ratio of the electrons to bremsstrahlung photons is not. So, we can compare the ratio of experimental data electrons to simulated electrons, and see if that ratio is the same for the bremsstrahlung radiation events. Fig. 6.10 illustrates this procedure: after subtracting pion background and RCS events of the simulation from the data, we are only left with electrons. This then allows us to compute the ratio N_e/N'_e, where the primed number corresponds to the simulation. The variable α, defined as $\alpha = \frac{n_\gamma/n'_\gamma}{N_e/N'_e}$ (where n_γ and n'_γ are defined in Eq. 6.6), should be equal to one. Its deviation from one is a measure of how much the simulation underestimates the background.

The main sources of bremsstrahlung radiation are target material (liquid hydrogen), target cell walls (0.125 mm of aluminum), target chamber vacuum window (0.4 mm of aluminum) and the air between target chamber wall and the magnet (105. cm, after which the

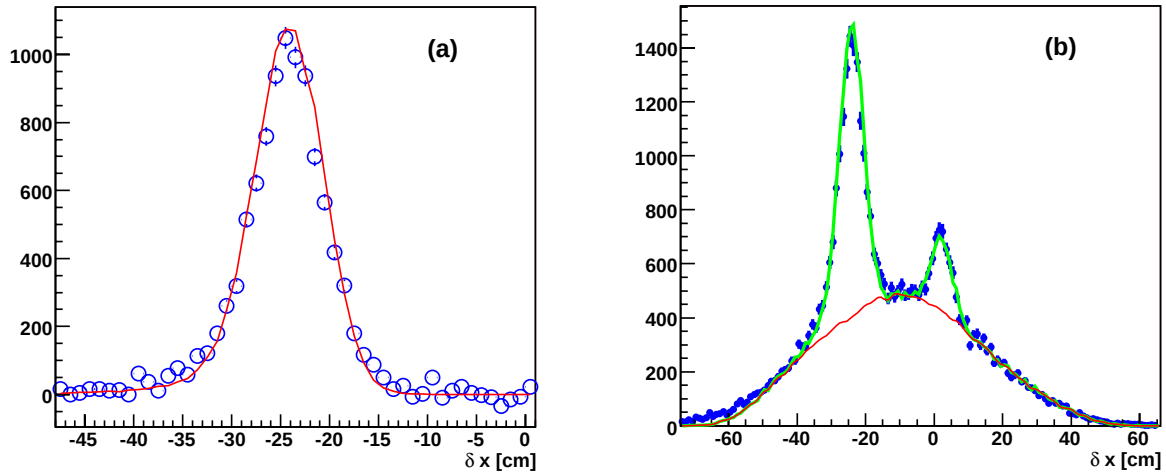

Figure 6.10: a) Electron data count distribution, with π^0 background subtracted. Red line is the simulation. b) A full data to simulation comparison, with a simulation of electron background added to the other event types.

electrons are deflected). One source of uncertainties is the real thickness of target chamber vacuum window: due to the atmospheric pressure the vacuum window surface is not flat, but is in fact highly wrinkled. This implies that the real distance traveled by electrons could be somewhat larger than the nominal thickness of the window. We estimate that the real thickness cannot exceed $2 \times 0.4mm$, and perform our simulation both with and without this assumption.

The value of α determined thus have been $\alpha_0 = 1.7 \pm 0.07$ and $\alpha_{wrinkling} = 1.4 \pm 0.06$. This proves that there is in fact other background, which is not of same origin as bremsstrahlung radiation. Meanwhile it is important to note that α is within the order of magnitude of one, and that the secondary background is less than our main well known bremsstrahlung background. Furthermore, it is important to understand that it is intuitively reasonable to assume that whatever the origins of the background, it decreases with increasing calorimeter

energy E_{calo}, and overall follows a shape which is similar to that of bremsstrahlung radiation.

To answer the question of by how much would the deviation of secondary background's shape from that of bremsstrahlung affect our results, we consider two assumptions. One assumption – one that we have used all along to determine the RCS cross section – is that *all* of the background follows the shape of bremsstrahlung radiation, making our results essentially perfect. The other assumption – a worst case scenario – is that while up to 900 MeV the background is identical to bremsstrahlung, it drops linearly with increasing energy, and becomes zero at $2300MeV$ (we can see from the data that at $2300MeV$ all types of backgrounds and signals come close to zero). The two resulting fits can be seen in Fig. 6.11 as the red lines, where the pointed line corresponds to assumption number two, and the full line is our standard fit (assumption number one). The difference of the cross sections calculated by these two methods has been found to be 7%. It would be correct then to assume that the real value of cross section is in the domain of $[0.93 \cdot d\sigma/dt; d\sigma/dt]$, where $d\sigma/dt$ is the cross section determined by assumption number one (standard fit). We then take the average of the two quantities, that is $0.965 \cdot d\sigma/dt$, as our final value of RCS cross section, and quote a systematic error of 3.5% due to bremsstrahlung background subtraction

.

6.2 Subtraction of Virtual Compton Scattering Events

At this point we have discussed the three event types – electron scattering, neutral pion production and electron bremsstrahlung – which constitute our main background. However, Virtual Compton Scattering(VCS), $ep \rightarrow ep\gamma$, is another process which is present in the

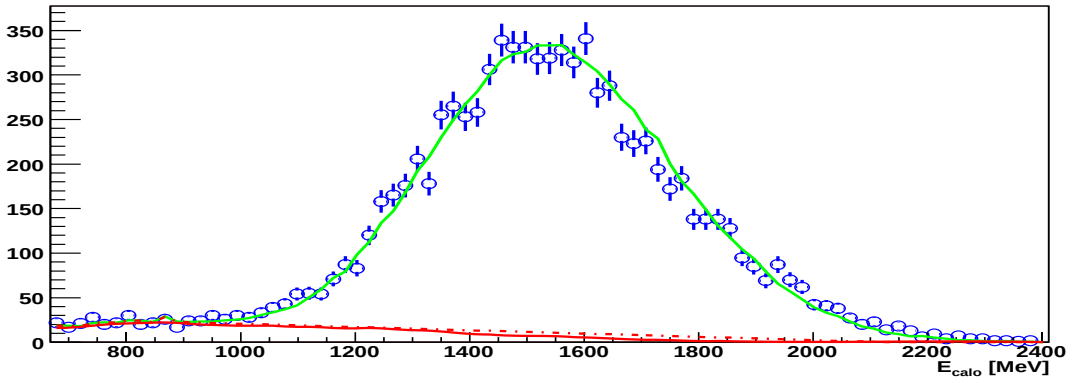

Figure 6.11: Calorimeter energy distribution. Red lines correspond to simulation with two assumptions: pointed line – that background drops linearly; full line – that background follows the simulated shape of bremsstrahlung radiation. The difference between the resulting cross sections is 7%

data and contributes to the background. Furthermore, due to kinematic similarity to Real Compton Scattering, it is impossible to separate the VCS events during data analysis. The Born diagram of VCS can be seen in Fig. 6.12.

There are however some constraints on VCS which make it highly predictable, in terms of relative cross sections. As the photon's virtuality increases, so does the angle between its direction and that of the beam. This translates into an offset in the angle of the final photon, resulting in larger absolute values of δx and δy. We perform a simple kinematic calculation for the electron vertex of the diagram in Fig. 6.12, in order to determine the dependence of virtual photon angle and it's virtuality $Q^2 \equiv -q^2$. The resulting relation is

$$\theta = \sqrt{Q^2 \cdot \frac{E_0 - E_\gamma}{E_0 E_\gamma^2}} \tag{6.9}$$

where E_γ is the virtual photon energy, and E_0 is the beam (electron) energy. From here we can see that as the incoming photon's virtuality increases, so does the angular offset of the reaction and proton vertex. Since the final proton's momentum stays the same, the offset

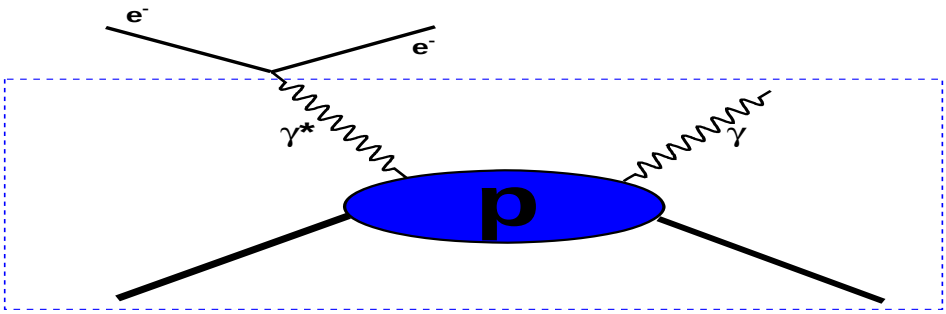

Figure 6.12: Virtual Compton Scattering(VCS). Due to very low virtuality ($-q^2 < 0.01GeV^2$) of the incoming photon, the part of the diagram enclosed in the blue square is essentially identical to Real Compton Scattering(RCS), in terms of amplitude and kinematic dependences. The only difference between this process and RCS is the incoming photon(γ^*) flux.

in in-plane angle causes a miscalculation of incoming energy, and hence of δx. Furthermore, the out-of-plane angles of the proton and the photon change in the same direction (while in normal kinematic conditions the out-of-plane angles change in opposite direction): this causes miscalculations in the value of δy as well. The acceptable virtuality of the incoming photon is hence severely limited by our narrow cuts on δx and δy.

Once the full range of Q^2 and E_γ has been determined, one can calculate the virtual photon flux and compare it to the real bremsstrahlung photon flux. A detailed calculation has been performed by V.M.Budneev *et al.* [67], determining the total number of virtual photons per energy per virtuality to be

$$\frac{dn_\gamma}{dE_\gamma\, d(Q^2)} = \frac{\alpha}{\pi}\,\frac{1}{Q^2\cdot E_\gamma}\left(1-\frac{E_\gamma}{E_0}+\frac{1}{2}(\frac{E_\gamma}{E_0})^2-(1-\frac{E_\gamma}{E_0})\frac{q^2_{min}}{q^2}\right) \tag{6.10}$$

where

$$q^2_{min} = m_e^2 \frac{(\frac{E_\gamma}{E_0})^2}{1 - (\frac{E_\gamma}{E_0})}$$

would be the lower limit of q^2 integration, m_e being the electron mass. Here it is worth noticing that the m_e^2 factor makes the last term in the parentheses of Eq. 6.10 extremely small, allowing us to write

$$\frac{dn_\gamma}{dE_\gamma \; d(Q^2)} = \frac{\alpha}{\pi} \; \frac{1}{Q^2 \cdot E_\gamma} \left(1 - r + \frac{1}{2} r^2\right) \quad \text{where} \quad r \equiv \frac{E_\gamma}{E_0}$$

Since the experimental acceptance is set very close to the bremsstrahlung endpoint, it could also be approximated that $r \approx 1$ and $\Delta r \equiv 1 - r \ll 1$. Using this, and performing a first order Taylor expansion of the $r^2/2$ term we get

$$\frac{dn_\gamma}{dE_\gamma \; d(Q^2)} \approx \frac{\alpha}{\pi} \; \frac{1}{Q^2 \cdot E_\gamma} \left(\Delta r + \frac{1}{2} \cdot (1 - 2\Delta r)\right) = \frac{\alpha}{2\pi} \; \frac{1}{Q^2} \cdot \frac{1}{E_\gamma}$$

Two important conclusions can be reached. First, that the energy dependence and Q^2 dependence of the flux are almost entirely disjoint of each other. And second, that the $1/E_\gamma$ dependence of the virtual photon flux is almost identical to that of the thin-target bremsstrahlung, which is the source of Real Compton Scattering. This has an important consequence: since the energy dependence at proton vertex (the blue box on Fig. 6.12) is also the same for VCS and RCS events, the calorimeter energy distribution of the final photons can be expected to be identical for both even types.

To determine the VCS to RCS ratio in the data, the VCS process has been added to the Monte Carlo simulation, allowing us to determine the $N_{VCS}/(N_{VCS} + N_{RCS})$ in a rigorous manner. The Monte Carlo simulation for the VCS events is almost identical to that of the RCS events, with the following differences:

- In the kinematic calculations, the incident photon has a "mass" of $\sqrt{Q^2}$
- The values of Q^2 and E_γ are chosen uniformly in a random manner.
- The final photon direction is offset by geometrical in-plane and out-of-plane angles of $\theta_v \cdot \cos(\phi_v)$ and $\theta_v \cdot \sin(\phi_v) \cdot \cos\theta_{scatt}$, respectively, where θ_v is virtual photon's angle relative to the incoming beam, determined by Eq. 6.9, ϕ_v is its azimuthal angle, chosen randomly between 0 and 2π, and θ_{scatt} is the final photon scattering angle.
- The same procedure is performed for the proton, with the only difference that θ_{scatt} is taken as proton's recoil angle.
- δx and δy are determined using 2-body kinematics, with the assumption of an RCS event.
- When calculating normalization to beam charge, bremsstrahlung flux is not included in the integration of cross section, but an extra weight factor of $\frac{dn_\gamma}{dE_\gamma\ d(Q^2)} \cdot \Delta E_\gamma \cdot \Delta(Q^2)$ is included in the final phase of the analysis, which is performed in ROOT. Here, $\Delta E_\gamma \cdot \Delta(Q^2)$ is the phase space of event generation in energy and virtuality.

Plots of simulations of RCS and VCS events can be seen in Fig. 6.13. During the analysis procedure, we apply cuts used in the data analysis on both RCS and VCS simulated events, and from there determine the ratio of $N_{VCS}/(N_{VCS} + N_{RCS})$. The final results of the VCS correction analysis are presented in Table 6.2. A quick examination shows that the correction to the RCS cross section is in the range of 11% to 15%. The final results of cross sections can be found in Table 6.3.

Kin. point	$VCS/(VCS+RCS)$	Calorimeter Distance (m)	cut on $\pm\delta x$ and $\pm\delta y$ (cm)
2a	0.120	12.0	15.,15.
2b	0.117	7.1	11.,8.
2c	0.113	5.2	10.,10.
3a	0.122	14.4	12.,11.
3b	0.124	10.0	10.,9.
3c	0.126	7.9	8.,15.
3d	0.134	6.2	9.,15.
3e	0.124	5.7	9.,10.
3f	0.128	5.3	9.,15.
4a	0.134	18.0	15.,7.
4b	0.151	16.4	15.,15.
4c	0.138	13.1	8.,10.
4d	0.137	10.1	8.,10.
4e	0.143	7.9	8.,8.5
4f	0.139	6.9	8.,7.
4g	0.134	6.2	8.,10.
4h	0.138	5.6	8.,10.
5a	0.140	18.0	9.5,5.2
5b	0.143	18.0	11.8,6.1
5c	0.138	14.5	8.1,5.8
5d	0.138	11.4	5.6,5.6
5e	0.132	9.5	6.4,5.
5f	0.130	8.8	5.3,5.2
5g	0.133	8.1	4.8,5.4
5h	0.125	7.0	3.8,6.1

Table 6.2: The proportion of Virtual Compton Scattering events, VCS/(VCS+RCS), calculated using Monte Carlo simulations, for different kinematic points.

	$d\sigma_{rcs}/dt$	δ_{rcs}	(E_{min}, E_{max})	s	t	θ_{CM}	$d\sigma_{\pi}/dt$	δ_{π}
2A	6.37	0.18	(1.95,2.25)	4.819	-1.649	-1.411	1046	4
2B	4.59	0.13	(1.95,2.25)	4.819	-2.010	-1.050	801	5
2C	2.18	0.05	(1.95,2.25)	4.819	-2.600	-0.460	201	2
3A	0.798	0.035	(3.,3.3)	6.789	-1.961	-3.069	80.17	0.50
3B	0.247	0.026	(3.,3.3)	6.789	-2.537	-2.493	12.10	0.16
3C	0.223	0.017	(3.,3.3)	6.789	-3.039	-1.990	16.50	0.10
3D	0.282	0.009	(3.,3.3)	6.789	-3.695	-1.335	17.50	0.11
3E	0.291	0.009	(3.,3.3)	6.789	-4.028	-1.002	43.13	0.16
3F	0.304	0.011	(3.,3.3)	6.789	-4.349	-0.681	56.40	0.20
4A	0.386	0.017	(4.05,4.5)	8.900	-2.030	-5.110	27.800	0.100
4B	0.107	0.006	(4.05,4.5)	8.900	-2.570	-4.570	2.294	0.030
4C	0.060	0.005	(4.05,4.5)	8.900	-3.087	-4.053	2.364	0.040
4D	0.034	0.003	(4.05,4.5)	8.900	-3.675	-3.465	3.780	0.017
4E	0.025	0.003	(4.05,4.5)	8.900	-4.383	-2.757	4.370	0.030
4F	0.031	0.003	(4.05,4.5)	8.900	-5.031	-2.109	3.693	0.028
4G	0.047	0.003	(4.05,4.5)	8.900	-5.477	-1.663	5.254	0.026
4H	0.063	0.004	(4.05,4.5)	8.900	-5.924	-1.216	11.000	0.060
5A	0.0680	0.0057	(5.1,5.6)	10.916	-2.612	-6.545	1.400	0.020
5B	0.0295	0.0039	(5.1,5.6)	10.916	-3.183	-5.974	0.900	0.020
5C	0.0152	0.0025	(5.1,5.6)	10.916	-3.730	-5.427	1.254	0.010
5D	0.0092	0.0010	(5.1,5.6)	10.916	-4.413	-4.743	0.770	0.010
5E	0.0069	0.0007	(5.1,5.6)	10.916	-5.027	-4.130	0.700	0.010
5F	0.0057	0.0009	(5.1,5.6)	10.916	-5.441	-3.716	0.720	0.010
5G	0.0045	0.0006	(5.1,5.6)	10.916	-5.933	-3.223	0.890	0.009
5H	0.0055	0.0007	(5.1,5.6)	10.916	-6.460	-2.697	1.150	0.007

Table 6.3: Final results of Real Compton Scattering differential cross sections, corrected for VCS contributions (as presented in Table 6.2).

Run ID	E_{beam} [GeV]	Calo D	Calo θ_γ/E_γ	HRS θ/p **off endpoint**	HRS θ/p **endpoint**
2a	2.341	12.0	46. / 1.260	35.6783 / 1.556	33.97/1.711
2b	2.341	7.1	56. / 1.066	29.824 / 1.779	28.28/1.951
2c	2.341	5.2	79. / 0.751	20.285 / 2.129	19.14/2.322
3a	3.478	14.4	31. / 2.161	39.08 / 1.768	37.44/1.928
3b	3.478	10.	39. / 1.824	32.46 / 2.142	30.95/2.332
3c	3.478	7.9	45. / 1.604	28.54 / 2.38	27.14/2.586
3d	3.478	6.2	57. / 1.255	22.53 / 2.752	21.36/2.981
3e	3.480	5.7	65. / 1.079	19.47 / 2.939	18.43/3.176
3f	3.478	5.3	75. / 0.906	16.36 / 3.118	15.47/3.362
4a	4.615	18.	22. / 3.228	42.58 / 1.789	40.97/1.943
4b	4.615	16.4	26. / 2.940	37.73 / 2.109	36.17/2.290
4c	4.615	13.1	30. / 2.665	33.691 / 2.407	32.21/2.611
4d	4.615	10.1	35. / 2.351	29.53 / 2.741	28.16/2.970
4e	4.615	7.9	42. / 1.974	24.951 / 3.137	23.74/3.391
4f	4.615	6.9	50. / 1.628	20.96 / 3.496	19.90/3.769
4g	4.615	6.2	57. / 1.390	18.21 / 3.742	17.27/4.025
4h	4.615	5.6	66. / 1.152	15.379 / 3.987	14.57/4.278
5a	5.754	18.0	20. / 4.005	40.0083 / 2.133	38.47/2.311
5b	5.754	18.0	23. / 3.700	36.0285 / 2.462	35.78/2.550
5c	5.754	14.5	26. / 3.409	32.664 / 2.772	31.25/3.002
5d	5.754	11.4	30. / 3.044	28.91 / 3.154	27.60/3.410
5e	5.754	9.5	34. / 2.717	25.83 / 3.494	24.62/3.772
5f	5.754	8.8	37. / 2.497	23.858 / 3.722	22.72/4.013
5g	5.754	8.1	41. / 2.234	21.59 / 3.992	2.54/4.298
5h	5.754	7.	46. / 1.953	19.221 / 4.28	N/A

Table 6.4: Kinematic values of the calorimeter and spectrometer settings

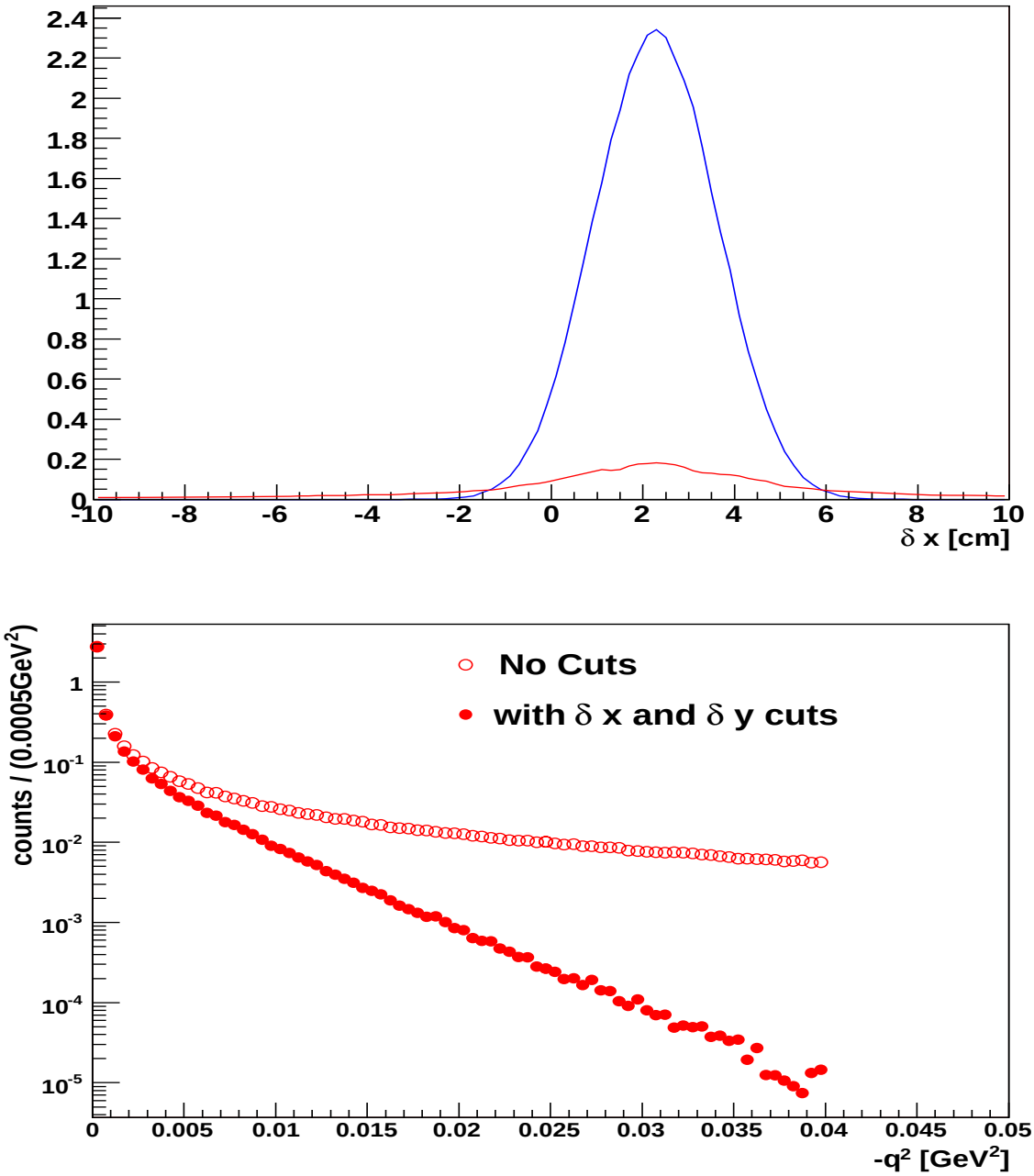

Figure 6.13: Top: δx distributions for RCS (blue) and VCS(red) events. Bottom: Q^2 distribution for virtual photons. The full circles correspond to data with cuts on δx and δy. The open circles are for the data with no cuts.

Chapter 7

Physics Analysis and Discussion of Results

7.1 Final Results of RCS Cross Section and Systematic Uncertainties

The previous chapters gave a detailed description of the two methods of data analysis which have been used to extract cross sections:

a) **Preliminary Analysis:** stringent cuts on acceptances, and polynomial fitting of pion and bremsstrahlung backgrounds (See Chapter. 4.4.2).

b) **Monte Carlo Analysis:** wide cuts on acceptance, use of Monte Carlo simulations to account for the acceptance effects, to subtract the background and to fit the signal.

The two methods employ very different and mostly unrelated approaches to the problem. The deficiencies of the preliminary analysis have been discussed at length in Chapter 4.4.3. It however can be argued that if the procedure is performed with great attention to detail, then the result can serve as a good measure of the order of magnitude of the actual cross section. It has been agreed that the mean of (a) and (b) will be used as the final result of the experiment, and that half of the difference between the two results will be used as a measure of the systematic error.

The table in Tab. 7.1 lists final results determined through this method, with a listing of the kinematic variables and statistic and systematic uncertainties.

7.2 Systematic Uncertainties

The systematic uncertainties are a description of an experimentalist's knowledge of his experimental apparatus and of the structure of the data which is subject to analysis. Experiments which measure cross sections are especially vulnerable to effects due to unknown acceptances and to complicated backgrounds, as discussed in detail in Chapters 5 and 6. In the case of current analysis, the problem of the acceptances and backgrounds has been addressed through a complex Monte Carlo simulation. The measure of the systematic uncertainties can be estimated by comparing the results achieved through Monte Carlo simulations (*i.e.* the analysis described in previous two chapters) with results achieved through polynomial fits, as described in detail in Chapter 4. If the data structure and the experimental setup is understood to perfection, then the two results, within statistic uncertainties, should not differ. In our case, however, a comparisons of the two results shows rather significant differ-

Kin. point	E_γ	s	t	u	θ_{cm}	$d\sigma/dt$	errors	
							statistic	systematic, lower lmt.
2A	2.100	4.819	-1.649	-1.411	1.556	5.7476	0.1910	0.6236
2B	2.100	4.819	-2.010	-1.050	104.38	4.3067	0.1382	0.2849
2C	2.100	4.819	-2.600	-0.460	127.94	2.0597	0.0616	0.1223
3A	3.150	6.789	-1.961	-3.069	76.26	0.8106	0.0351	0.0125
3B	3.150	6.789	-2.537	-2.493	89.23	0.2427	0.0263	0.0043
3C	3.150	6.789	-3.039	-1.990	100.48	0.2192	0.0175	0.0037
3D	3.150	6.789	-3.695	-1.335	115.89	0.2737	0.0103	0.0086
3E	3.150	6.789	-4.028	-1.002	124.49	0.2809	0.0088	0.0099
3F	3.150	6.789	-4.349	-0.681	133.71	0.2932	0.0170	0.0106
4A	4.275	8.900	-2.030	-5.110	64.01	0.3905	0.0173	0.0048
4B	4.275	8.900	-2.570	-4.570	73.22	0.1154	0.0082	0.0084
4C	4.275	8.900	-3.087	-4.053	81.62	0.0640	0.0052	0.0036
4D	4.275	8.900	-3.675	-3.465	90.98	0.0343	0.0026	0.0006
4E	4.275	8.900	-4.383	-2.757	102.29	0.0252	0.0026	0.0003
4F	4.275	8.900	-5.031	-2.109	113.10	0.0311	0.0034	0.0004
4G	4.275	8.900	-5.477	-1.663	121.06	0.0468	0.0029	0.0000
4H	4.275	8.900	-5.924	-1.216	129.75	0.0593	0.0039	0.0033
5A	5.350	10.916	-2.612	-6.545	64.28	0.0670	0.0060	0.0009
5B	5.350	10.916	-3.183	-5.974	71.93	0.0288	0.0039	0.0007
5C	5.350	10.916	-3.730	-5.427	78.96	0.0150	0.0025	0.0001
5D	5.350	10.916	-4.413	-4.743	87.51	0.0092	0.0010	0.0000
5E	5.350	10.916	-5.027	-4.130	95.14	0.0072	0.0007	0.0002
5F	5.350	10.916	-5.441	-3.716	100.33	0.0058	0.0009	0.0000
5G	5.350	10.916	-5.933	-3.223	106.62	0.0042	0.0007	0.0003
5H	5.350	10.916	-6.460	-2.697	113.59	0.0053	0.0007	0.0002

Table 7.1: Table of final cross section results.

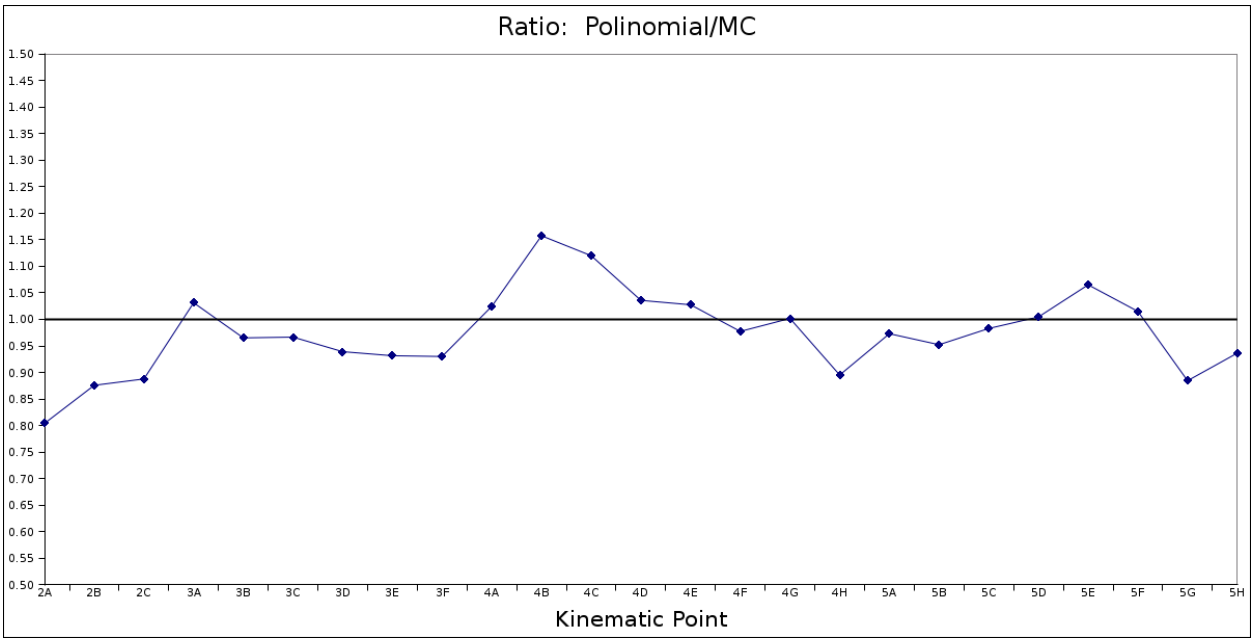

Figure 7.1: The ratio of the results as determined by Polynomial Fitting method and Monte Carlo method.

ences. Excluding the data points of $2A$, $2B$ and $2C$ kinematic settings (which in any case do not participate in the physics analysis, due to their extremely low values of $-t$ and $-u$) the results differ from as little as 1% to as much as 15%. It then can be said that this difference is a reflection of the overall combined systematic uncertainties in the experiment and data analysis. The plot in Fig. 7.1 is a distribution of the ratio $d\sigma_{polynom}/d\sigma_{MC}$, where the first cross section is determined through the polynomial fitting, while the second is the results of the Monte Carlo method.

The plot indicates to a rather random distribution of the ratio, which suggests that the systematic error (as determined through this method) is of a random nature and that the total error should the determined by adding the systematic and statistic errors in quadratures. The final value of cross section is determined by taking the mean of the two results. The total statistical error is determined to be the largest of the two statistic errors.

It has to be added here that these estimates of systematic uncertainties, determined through this method, are not by themselves a full measure of systematic error of the experiment, and if no further information were provided they would have been rather a lower limit on the error. However, the previously performed tests of the Monte Carlo simulations, where elastic electron scattering events were used to check the accuracy of the numerical model, can be used here to provide an estimate of the order of magnitude of the systematic errors due to the Monte Carlo analysis itself. Some of the few results of the systematic checks for Monte Carlo are summarized as follows:

a) Acceptance scans. As described in detail in Chapter 5, these were performed with elastic electron scattering data. The Monte Carlo fits of the accumulated data were performed in order to extract elastic electron scattering cross sections. These were then compared to recent results, from other experiments at Jefferson Laboratory [68]. A list of the comparisons is shown in Table 5.1. It was found that the data reproduced existing cross sections to within $(1 \pm 0.5)\%$, and that the variation of the calculated cross section amounted to only $(2 \pm 1.2)\%$.

b) Uncertainties due to the fits of $ep\gamma$ bremsstrahlung background. In Sec. 6.1.1 we studied the nature of radiative background underneath the Compton peak in δx distribution. It was found that the background is larger than expected. Hence a second method of fitting was tried, where a simple linearly dropping distribution function was used to model the $ep\gamma$ background, as a worst case scenario. For kin. $3C$ this fit resulted in a value of cross section which was 7% below the one provided by the usual MC fit. The average of the two results was taken as the final result, and a 3.5% uncertainty was

assumed for that point. However, it should also be added that kin. $3C$ was specifically chosen as the worst limiting case: a combination of low calorimeter energy resolution and large $ep\gamma$ background resulted in a maximum effect on the final result. Similar analysis for other kinematic points with better calorimeter resolution resulted in much smaller (such as only $1-2\%$) disagreements.

c) Dependence of cross section on calorimeter acceptance cuts. It was shown in Sec. 6.1.1 that the variation of the cross section was within the statistical uncertainty for the different data cuts.

It is then useful to compile a list of the most important possible sources of experimental uncertainties, and discuss how the above discussed checks provide for an upper limit on those uncertainties:

- Acceptance effects. As found above, this is limited to no more than 2%. There is a minor caveat however: the acceptance scans which were performed using elastic electron scattering data covered the full momentum acceptance, however the angular coverage is much less – 40 $mRad$ out of total 60 $mRad$. This can result in uncertainties due to the edges of the angular acceptance. Here however we can use the information from point (c) above. As we place cuts on the calorimeter acceptance, the two-body nature of the reaction conversely places similar constraints on the spectrometer acceptance. The good stability of the cross section results which we observed under different cuts on calorimeter acceptance then imply that uncertainties due to the edges of spectrometer's angular acceptance are much smaller than the statistic uncertainty.

- Cuts on target vertex. Spectrometer's optic aberrations can result in inaccurate cuts on the target vertex, which will cause errors in the known values of total luminosity. This however is entirely limited by the check in (a): since the acceptance scan measurements also included cuts on target vertex, therefore any possible effects should be limited by the 2% as found above.

- Effects due to inaccurate values of electronic and computational dead times. The acceptance scans were performed in coincidence mode, and the data was collected under the same trigger type as the production data. This implies that any problems with electronics and computation would have had affected the results in (a) as well. A minor caveat exists here as well: in the case if the production data involved much larger trigger rates than those for acceptance scan, then this statement would not be valid, since larger computational dead times could have caused larger uncertainties. This however can be checked. The rates for the coincidence trigger for the acceptance scans were varying between $210 - 390\ Hz$ and the dead times were varying between $8\% - 9\%$. For production data taking the trigger rates for coincidence where the largest at the most forward angles, where high cross sections for elastic electron scattering contributed to a very large data flux. The trigger rates and dead times for the kinematic points $3A$ were 240 Hz and 95%, and for $4A$ were 72 Hz and 96%. For most of the other kinematic points the typical even rates constituted about $20 - 50\ Hz$ and live times were about 99%. It then can be said that the systematic uncertainties due to dead times for production data were same as or less than those for acceptance scans.

- Inaccuracies in the accumulated beam charges as reported by the Beam Charge Monitors. Since the evaluations of the elastic cross sections in (a) utilized this information, therefore any uncertainties related to this effect should be contained within the 2% overall limit.

- Inaccuracies due to cuts on calorimeter acceptance and/or calorimeter performance. It is possible, that, due to limited coordinate resolutions, the real area affected by the cuts was different from the one assumed in analysis. However, similar cuts were also employed in the acceptance scans analysis, as described in (a). Furthermore, a similar effect would have been felt in the checks of (c). Again, this places an upper limit of 2% on this effect.

- Radiator thickness and correctness of the integration of Eq. 5.10 as performed in Ref. [59]. This is by far the largest uncertainty affecting our results. The results of this integration have been compared to GEANT simulations, demonstrating an agreement of 1% [43]. It is however impossible to entirely rule out the possibility that both calculations were in fact incorrect. A number of dedicated experiments are being planned in JLab's Halls A and B [69], with the sole purpose of measuring the bremsstrahlung photon flux and compare the results to the calculations of Ref. [59].

7.2.1 Differential cross section comparisons

Once the final cross section results have been agreed upon, comparisons with the theoretical predictions can be performed. The theoretical values of cross section have been provided by

calculations performed by M. Diehl and P. Kroll. These included calculations of vector and axial form factors $R_V(t)$ and $R_A(t)$ and of Next to Leading Order (NLO) expressions for cross section [11] [12], which are by no means small. Comparisons between the final cross section results and theoretical calculations based on Soft Overlap Handbag Mechanism can be seen in Fig. 7.2. The plot also shows data from a previous experiment (see Ref. [6]) in form of open points. In order to adjust the cross sections of Ref. [6] to the kinematic settings of the experiment, we have used the following approach: for every point which has a value of s_0 which differs from our settings of s, we have applied a multiplicative correction of $(s_0/s)^n$, where the value of the exponent has been found to be approximately $n = 8$, as found in the next sections.

The raw comparison points to a considerable disagreement between data and theory. It is however important to keep in mind that the calculations have been performed for $-t, -u, s \gg m_p^2$, where m_p is proton's mass. It has been suggested (see Ref. [11]) that $-u, -t > 2.5\ GeV^2$ is a good estimate to satisfy this condition. The plot in Fig. 7.3 is plotted with this condition in mind, showing a rather clear improvement over the previous comparison.

The main contributions to theoretical errors arise from uncertainties over target mass corrections. This is due to the ambiguity of relating the internal Mandelstam variables $\hat{s}, \hat{u}, \hat{t}$ (which define the perturbative upper part of the Handbag diagram, Fig. 7.9) to external experimentally measurable ones, s, u, t. Depending on kinematic setting and on the values of Mandelstam variables, this uncertainty can be rather large, and has been estimated through extensive calculations, as detailed in Ref. [70]. The upper and lower limits, and the central

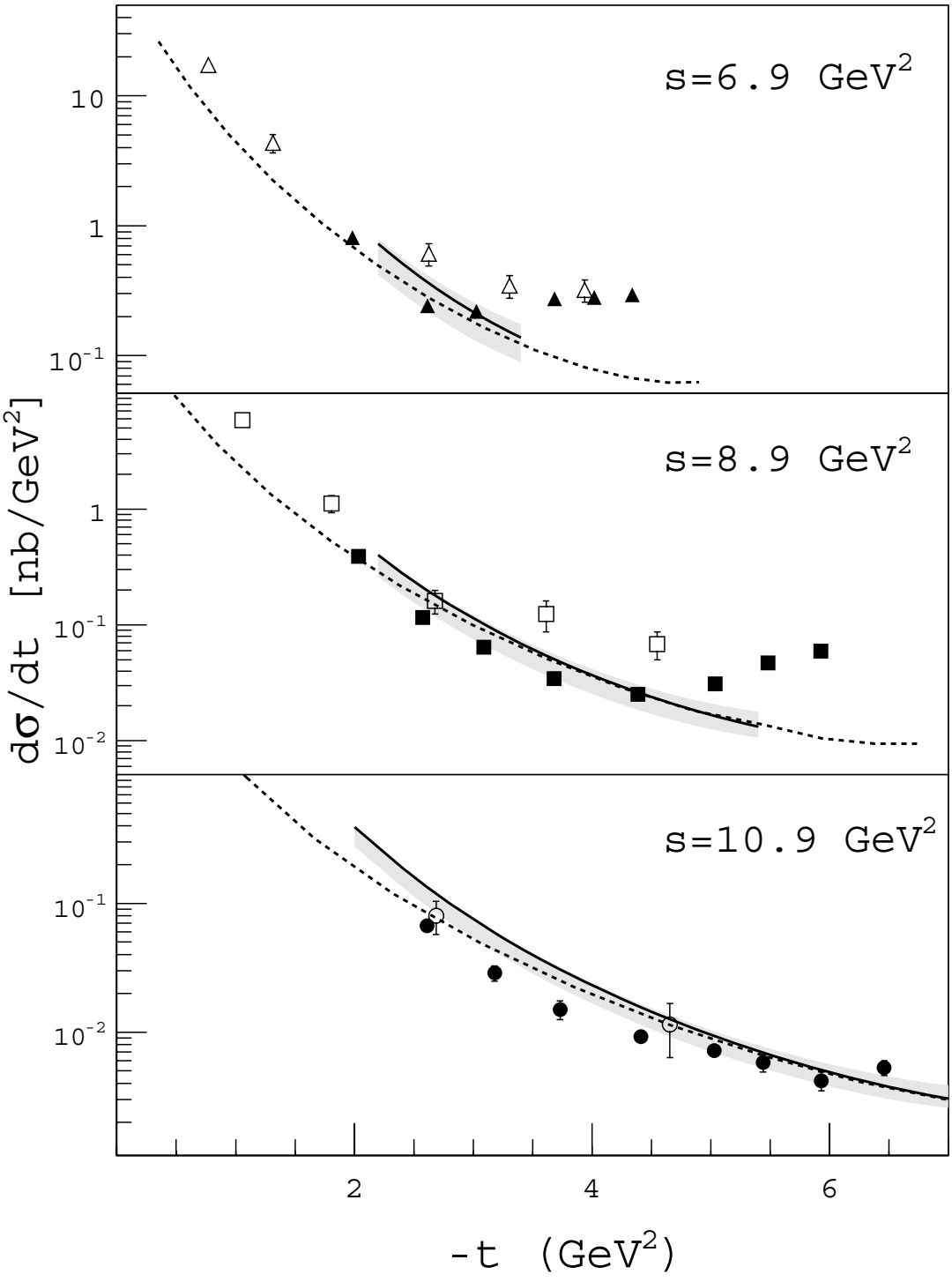

Figure 7.2: RCS cross section $d\sigma/dt$ in units of nB/GeV^2. Solid points represent data from this experiment (E99-114), while open points marks correspond to previous data [6]. The lines with error bands correspond to calculations of RCS form factors using GPD formalism, see Ref. [11] [12]

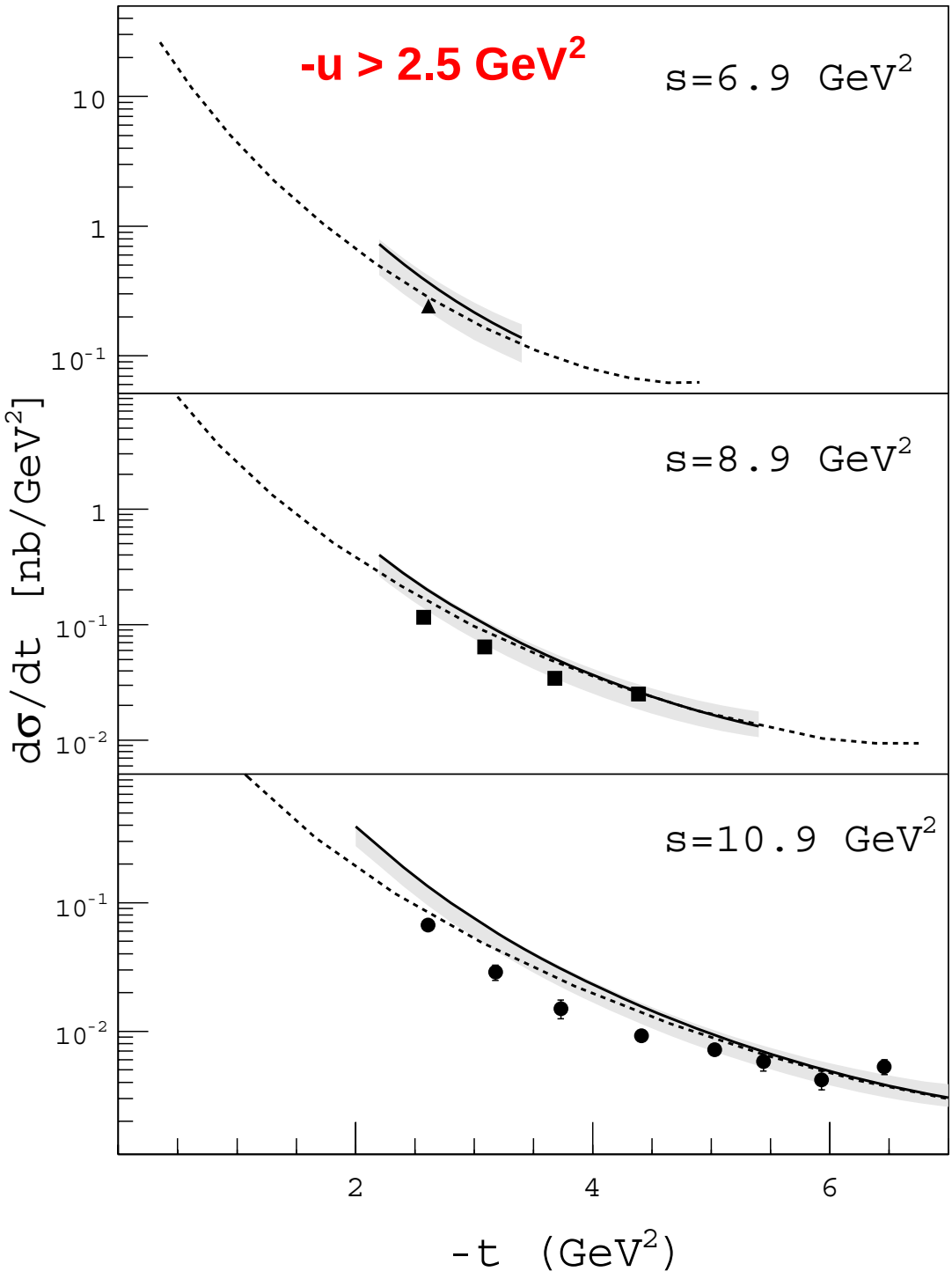

Figure 7.3: Same results as in Fig. 7.2, however with the condition of $-u > 2.5 GeV^2$

curve of the theoretical bands in Fig. 7.3 are determined by the following three approaches:

Scenario 1	Scenario 2	Scenario 3
$\hat{s} = s$	$\hat{s} = s - m_p^2$	$\hat{s} = s - m_p^2$
$\hat{t} = t,\ \hat{u} = u$	$\hat{t} = t,\ \hat{u} = u - m_p^2$	$\hat{t} = -\hat{s}(1 - \cos\theta)/2,\ \hat{u} = -\hat{s} - \hat{t}$

The comparisons in Fig. 7.3 and later on in Fig. 7.4 allow as to say that while the Handbag model would definitely benefit from some refinement(as will be shown later), it does to a larger degree describe the RCS data.

7.2.2 s-dependence of $d\sigma/d\sigma_{KN}$ ratio, and vector form factor R_V

From the previous section it is possible to conclude that there is, at least within experimental and theoretical uncertainties, an encouraging agreement between the experimental results and the theoretical predictions which are based on Soft Overlap Mechanism. It is then possible to use the cross section results to determine the values of vector form factor $R_V(t)$. As already mentioned previously in Chapter 2, it is possible to approximate

$$\frac{d\sigma/dt}{d\sigma_{KN}/dt} \approx R_V^2(t)$$

where σ_{KN} is the Klein-Nishina cross section for Compton scattering on a structureless and massless point particle. This is however an approximation which is largely based on the assumption that $f_V \approx 1$ (see Eq. 2.13). In our experimental setting this factor varies between $f_V = 0.82$ and $f_V = 0.98$, a circumstance which has to be taken into account. The approach here is to use the following transformation:

$$\frac{d\sigma}{d\sigma_{KN}} = R_V^2(t)\left[f_V + (1 - f_V)\cdot\left(\frac{R_A(t)}{R_V(t)}\right)^2\right] \tag{7.1}$$

The small value of $1 - f_V$ factor make the cross section data largely insensitive to the axial form factor $R_A(t)$. We however can and do extract this ratio from the polarized Compton data, which has been analyzed and presented by E99-114 collaboration in Ref. [13]. The theory predicted that the asymmetry of polarization transfer from a polarized photon to an unpolarized proton can be expressed as (see, e.g. Ref. [20] [34])

$$K_{LL} \approx K_{LL}^{KN} \cdot \frac{R_A(t)}{R_V(t)} \tag{7.2}$$

where K_{LL}^{KN} is the asymmetry for Compton scattering on massless, structureless proton, and can be determined through QED calculations. It was found that

$$\alpha \equiv \frac{R_A(t)}{R_V(t)} = 0.81 \pm 0.15 \quad \text{for} \quad -t = 4.03\ GeV^2$$

It is also assumed that the t-dependence of this ratio is small enough as not to considerably affect our calculation. Armed with this information we finally can express the vector form factor through cross section values:

$$R_V(t) = \left(\frac{d\sigma}{d\sigma_{KN}}\right)^{1/2} \quad [f_V + \alpha(1 - f_V)]^{-1/2} \tag{7.3}$$

Form factor R_V to Next to Leading Order (NLO)

The above discussion described the calculations which have been performed to leading order. Next to leading order (NLO) effects are however considerable, and have been computed in detail by Markus Diehl and Peter Kroll [4]. Neglecting the contributions arising from the gluonic subprocess, the generic expression for the cross sections' ratio can be written as

$$d\sigma/d\sigma_{kn} = f_V R_V^2(\hat{t}) + g_V R_A^2(\hat{t}) \tag{7.4}$$

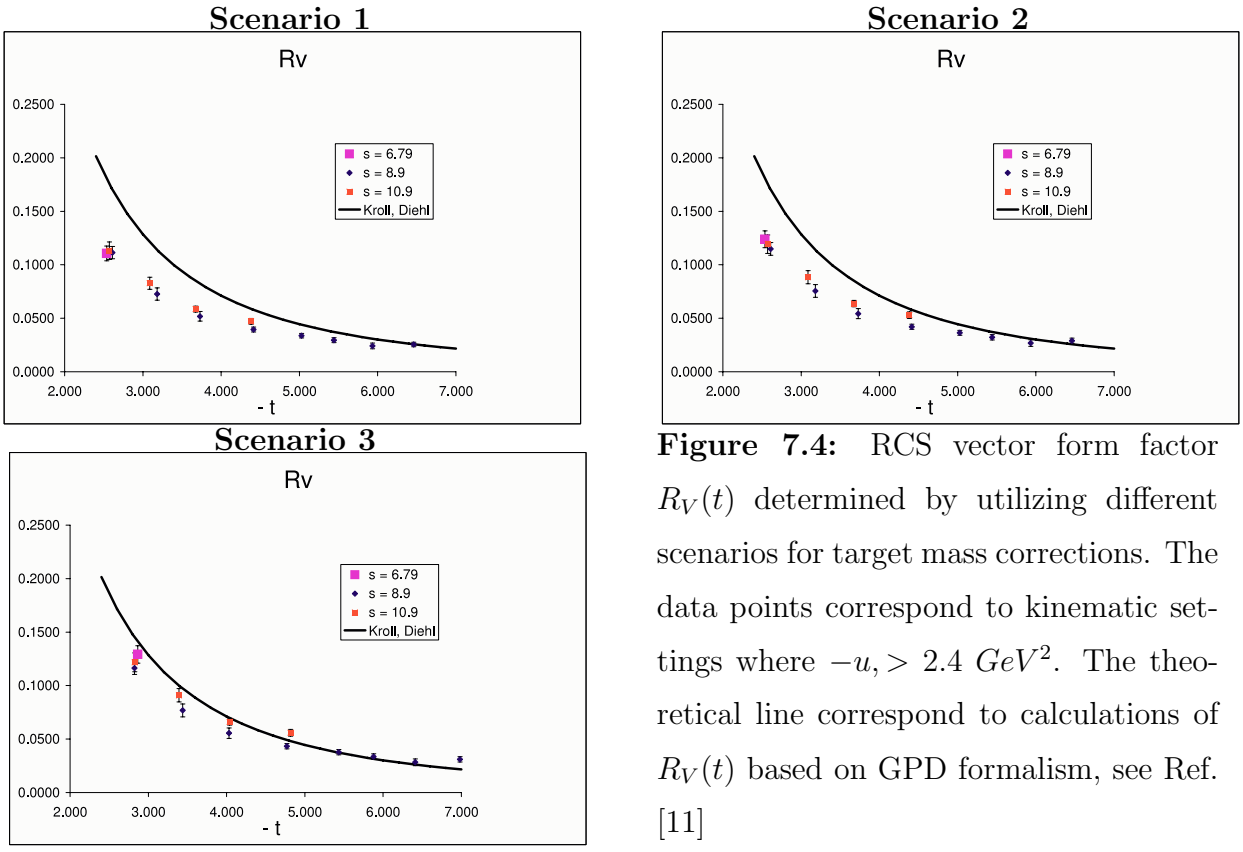

Figure 7.4: RCS vector form factor $R_V(t)$ determined by utilizing different scenarios for target mass corrections. The data points correspond to kinematic settings where $-u, > 2.4\ GeV^2$. The theoretical line correspond to calculations of $R_V(t)$ based on GPD formalism, see Ref. [11]

where the kinematic functions f_V and g_V are

$$f_V = \frac{1}{2}\frac{(\hat{s}-\hat{u})^2}{\hat{s}^2+\hat{u}^2}\left[1+\frac{\alpha(s)}{2\pi}C_F\frac{a\hat{s}-b\hat{u}}{\hat{s}-\hat{u}}\right]$$
$$g_V = \frac{1}{2}\frac{(\hat{s}+\hat{u})^2}{\hat{s}^2+\hat{u}^2}\left[1+\frac{\alpha(s)}{2\pi}C_F\frac{a\hat{s}+b\hat{u}}{\hat{s}+\hat{u}}\right]$$

where the color factor is $C_F = 4/3$ and the NLO functions are

$$a = 1+\frac{2\hat{t}-\hat{s}}{\hat{s}}\ln(\hat{t}/\hat{u})+(\ln(-\hat{t}/\hat{s}))^2+\hat{t}^2/\hat{s}^2(\ln(\hat{t}/\hat{u}))^2+\pi^2$$
$$b = 1+\frac{2\hat{t}-\hat{u}}{\hat{u}}\ln(-\hat{t}/\hat{s})+(\ln(\hat{t}/\hat{u}))^2+\hat{t}^2/\hat{u}^2(\ln(-\hat{t}/\hat{s}))^2+\pi^2$$

The strong coupling is determined from

$$\alpha(\hat{s}) = \frac{12\pi}{27\ln(\hat{s}/(\Lambda_{QCD})^2)}$$

where $\Lambda_{QCD} = 230MeV$ [4].

The final results of the extracted form factors is presented in Table 7.2.

Data to theory comparisons can be seen in Fig. 7.4, with the constraint of $-t, -u > 2.4\ GeV^2$. The vertical error bars are a combination of systematic and statistic uncertainties summed in quadratures. The horizontal error bars correspond to the difference in $-\hat{t}$ as calculated through Scenario 1. This difference should in principle be applied to the form factor curve. However, since the value of $|\Delta t|$ is different for different values of s, it was decided to apply the error bar on the data points instead. Two important conclusions can be drawn here:

- The data points are in a moderate agreement with the Soft Overlap Mechanism's calculation for the vector form factor.
- Apart from the pair of data points at $-t = 4.5\ GeV^2$, there seems to be very little dependence on Mandelstam variable s.

The second point is of a particular importance. The strongest model-independent feature of the Soft Overlap Mechanism says that if the mechanism is overall correct, i.e. if it is in fact possible to describe the Compton scattering through form factors, then those form factors should exhibit dependence only on one variable – t.

In his initial paper, A.V. Radyushkin presented a simple parameterization for the GPD's, which was based on the soft overlap of proton's initial and final state wavefunctions, and

s	t	u	$R_V(t), sc.\ 1$	err.	$R_V(t), sc.\ 2$	err.	$R_V(t), sc.\ 3$	err.
4.819	-1.649	-1.411	0.3242	0.0230	0.3925	0.0278	0.4131	0.0293
4.819	-2.010	-1.050	0.2549	0.0125	0.3317	0.0163	0.3575	0.0176
4.819	-2.600	-0.460	0.1264	0.0056	0.2105	0.0094	0.2418	0.0108
6.789	-1.961	-3.069	0.2112	0.0062	0.2289	0.0067	0.2352	0.0069
6.789	-2.537	-2.493	0.1106	0.0070	0.1239	0.0078	0.1292	0.0081
6.789	-3.039	-1.990	0.0987	0.0048	0.1148	0.0056	0.1218	0.0059
6.789	-3.695	-1.335	0.0960	0.0033	0.1210	0.0042	0.1328	0.0046
6.789	-4.028	-1.002	0.0868	0.0029	0.1170	0.0039	0.1316	0.0044
6.789	-4.349	-0.681	0.0750	0.0035	0.1124	0.0053	0.1306	0.0061
8.900	-2.030	-5.110	0.2103	0.0059	0.2187	0.0062	0.2221	0.0063
8.900	-2.570	-4.570	0.1133	0.0082	0.1193	0.0086	0.1218	0.0088
8.900	-3.087	-4.053	0.0828	0.0057	0.0884	0.0061	0.0909	0.0062
8.900	-3.675	-3.465	0.0586	0.0027	0.0638	0.0030	0.0662	0.0031
8.900	-4.383	-2.757	0.0472	0.0027	0.0530	0.0031	0.0559	0.0032
8.900	-5.031	-2.109	0.0480	0.0029	0.0561	0.0034	0.0605	0.0037
8.900	-5.477	-1.663	0.0538	0.0017	0.0657	0.0020	0.0722	0.0022
8.900	-5.924	-1.216	0.0533	0.0032	0.0693	0.0042	0.0783	0.0047
10.916	-2.612	-6.545	0.1114	0.0058	0.1149	0.0059	0.1164	0.0060
10.916	-3.183	-5.974	0.0726	0.0057	0.0755	0.0060	0.0768	0.0061
10.916	-3.730	-5.427	0.0518	0.0045	0.0543	0.0047	0.0556	0.0049
10.916	-4.413	-4.743	0.0395	0.0023	0.0420	0.0024	0.0433	0.0025
10.916	-5.027	-4.130	0.0337	0.0022	0.0364	0.0023	0.0378	0.0024
10.916	-5.441	-3.716	0.0295	0.0023	0.0322	0.0025	0.0336	0.0027
10.916	-5.933	-3.223	0.0242	0.0027	0.0269	0.0030	0.0284	0.0032
10.916	-6.460	-2.697	0.0256	0.0021	0.0290	0.0024	0.0310	0.0025

Table 7.2: Final results for vector form factor $R_V(t)$, determined using Scenarios one, two and three for target mass corrections. Number two has been considered to be the preferred scenario.

showed that by using a combination of x-dependence (derived from GRV parameterizations [71]) and a simple Gaussian dependence of transverse momentum of the quark, it is possible to achieve a reasonably good fit of the elastic form factor data (See Ref. [3, pp.3-4, Fig.3]). It should be noted, however, that the Leading Order model presented by Radyushkin has since been perfected by a number of Next to Leading Order (NLO) calculations [11; 34], which included higher order terms and resulted in the current rather encouraging data-theory agreement (compare, *e.g.*, Fig. 7.4 here to Fig. 3 in Ref. [3]). The conclusion that one reaches is that the GPD parameterizations and models used to describe Real Compton Scattering are not yet perfect, and have been and will be developed further. It is however important to note that, while a particular model or mechanism from the framework of GPD's may or may not reproduce the $R_V(t)$ data, it has to provide for an expression of the form factor (*e.g.* that of Eq. 7.3) which will make it first of all s-independent when derived from the data. This, we believe, is one of the most basic tests of validity of GPD formalism, when applied to Real Compton scattering. The results for $R_V(t)$, as presented in Fig. 7.4, demonstrate that this is already clearly the case for most of the data.

7.2.3 $s^{-n(\theta_{cm})}$ scaling in $d\sigma_{rcs}/dt$

As already discussed in Chapter 2, the most rigorous prediction of Leading Twist Mechanism is the Constituent Quark Counting Rule for exclusive interactions [16], which predicts the following dependence of cross section on Mandelstam variable s:

$$\frac{d\sigma}{dt} = \frac{f(\theta_{CM})}{s^n} \tag{7.5}$$

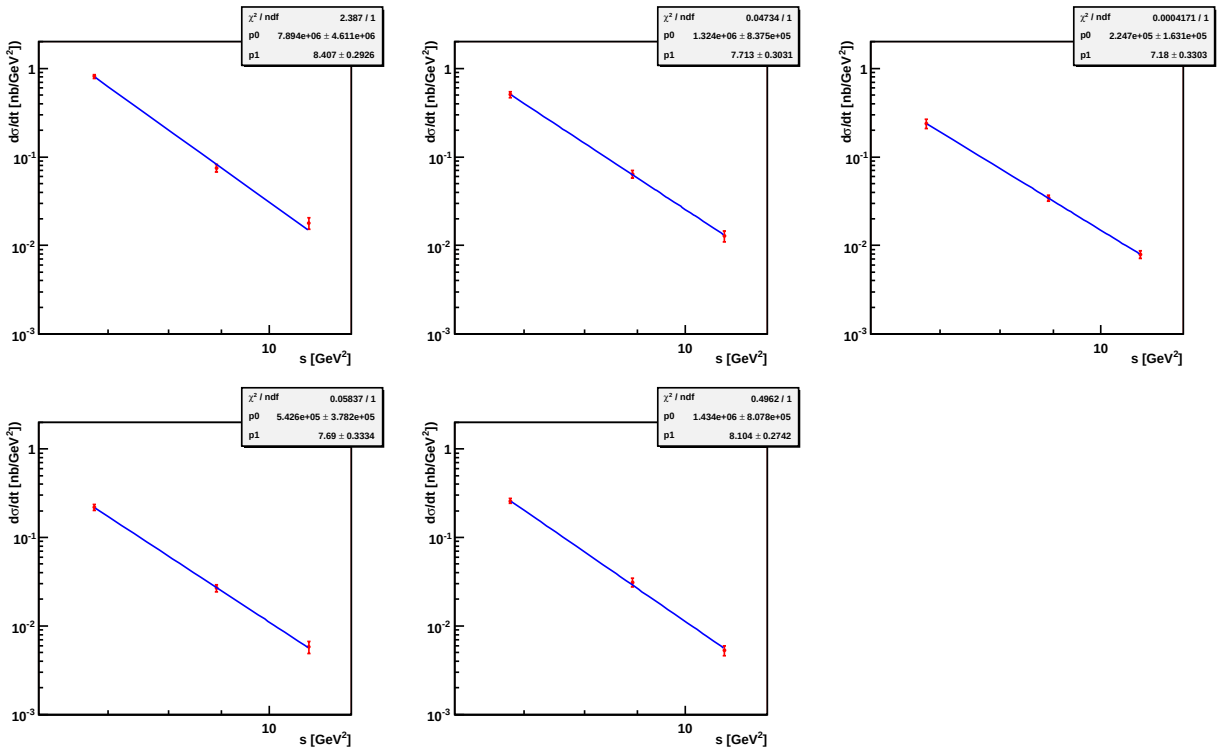

Figure 7.5: Fits to the cross section for given values of θ_{cm}. On log-log scale the fitting function reduces to a simple linear fit of the following form: $\log(d\sigma/dt) = c + n \cdot \log s$

where for Real Compton scattering $n = 6$. The kinematic settings for data taking have been planed in such a manner as to allow for kinematic points to be grouped in constant(or almost constant) θ_{CM}. This then allows one to fit the points in a particular group with a power law function of the form $n(\theta_{cm}) = a \cdot s^n$ and hence to determine the value of n for different values of θ_{cm}.

The plots on Fig. 7.6 show the predictions of the two mechanisms for $n(\theta_{CM})$. The blue points correspond to previously available data [6], while the red points are calculated based on cross section results from this experiment. The full red points correspond to values of n which were extracted based on a fit of three kinematic points. The data with the lowest values of scattering angle, at $\theta = 76^o$ and $\theta = 81^o$ were calculated based on only two

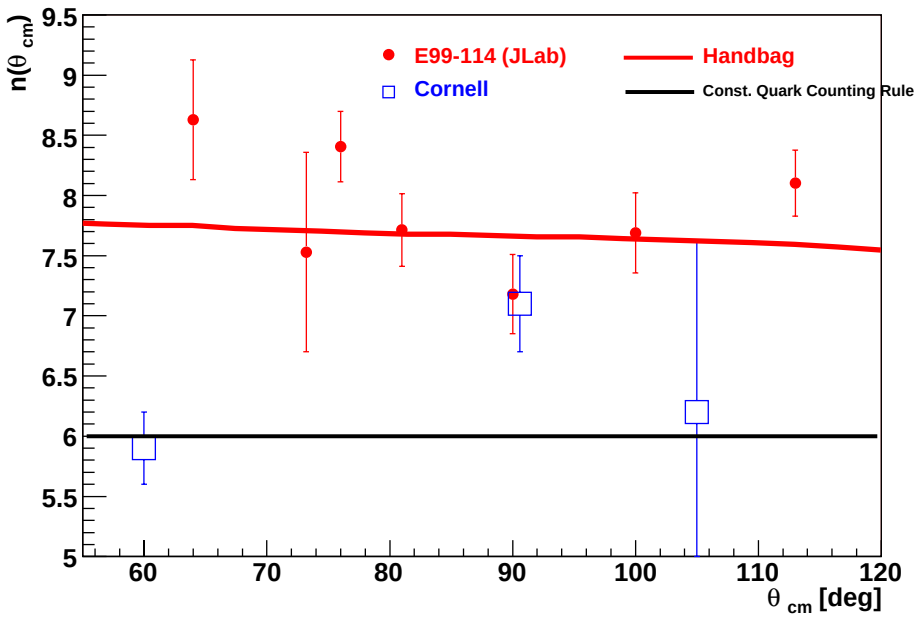

Figure 7.6: Extraction of exponent n from the data for the Constituent Quark Counting Rule prediction of $d\sigma/dt = f(\theta_{CM})/s^n$. Red data points correspond to this experiment(E99-114), blue squares correspond to previously available data [6]. The red curve is determined based on Soft Overlap Handbag Mechanism.

kinematic points (in which case the fit reduces to a simple interpolation). The rest of the data however involved three different values of cross section. To account for slightly different values of angle for the kinematic points inside a given group, we used simple second order interpolation between the nearby values of cross section to correct the cross section for the difference in angles. The plot in Fig. 7.5 demonstrates the five different power law fits over the cross sections which provided the values of n in Fig. 7.6.

There are a number of conclusions that can be reached based on this interpretation of the results:

- The $\propto s^{-6}$ dependence in cross section is the single most rigorous and model independent feature of the Leading Twist Mechanism, hence the disagreement of the data with this prediction gives a definite basis to the conclusion that the Leading Twist Mechanism is clearly sub-dominant for Compton scattering at the energy scale corresponding to our experiment. It should be added that this is only a confirmation of the conclusion about the sub-dominance of Leading Twist Factorization which was reached based on the results of polarized data of the E99-114 experiment (see Ref. [13]).

- The consistency of the Soft Overlap with the experimental result is less obvious, however. Data seems to indicate to a much steeper dependence on s than what the GPD prediction predicts. Furthermore, the symmetric distribution of $n(\theta_{CM})$ around the central angle of $\theta = 90^o$ is particularly in disagreement with the Soft Overlap's prediction of a steadily decreasing n.

The conclusion that one can come to, based on the above observations, that this results

confirms beyond doubt what was already seen in the RCS polarized results [13], namely, that Leading Twist Mechanism is clearly sub-dominant at the energies and reactions specific to our experiment.

7.3 Conclusions

The initial purpose behind the E99-114 experiment was to identify the dominant mechanism for Real Compton Scattering at medium energies. Two types of measurements were conducted: polarization transfer experiment, where the cross section asymmetry due to incoming photon helicity was measured, with results described in Ref. [13]; differential cross section measurements, which had the purpose of providing values of cross sections for different kinematic conditions. This thesis reflects the effort behind the later aspect of the experiment. The results described earlier in this chapter have now allowed for a thorough discussion.

7.3.1 Leading Twist Mechanism

The Leading Twist Mechanism, described in detail in Chapter 2 is based on the assumption that the momentum transfered from the photons is distributed uniformly between the valence quarks through the exchange of hard perturbative gluons. The large number of hard vertexes in the Feynman diagram(see Fig. 2.1) contribute to a particularly low cross section for the scenario which utilizes asymptotic DA's to model the momentum distribution between the valence quarks. It furthermore treats the gluonic exchanges and quark propagators within the perturbative framework of pQCD. Comparisons with existing data have shown this particular

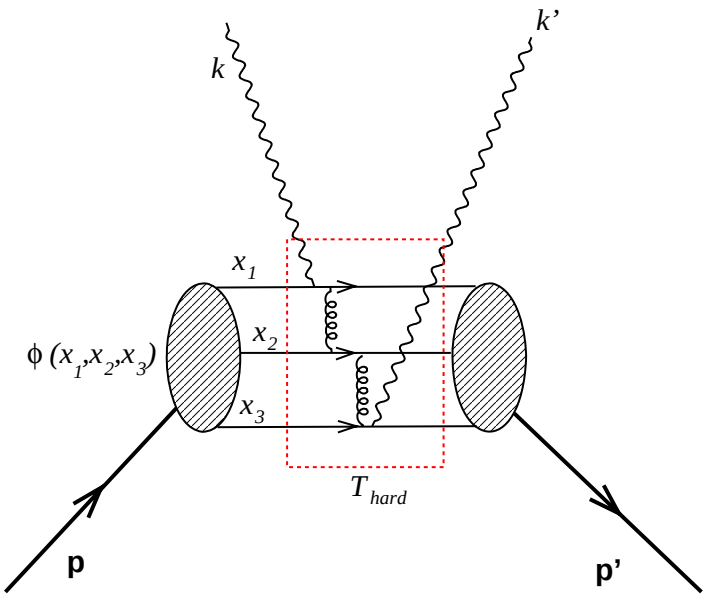

Figure 7.7: Leading Feynman Diagram for Leading Twist Mechanism. x_i stand for the fractional momentum of the quarks. The diagram enclosed by the doted box corresponds to T_{hard} from Eq. 2.4, and its amplitude can be determined using calculations based on pQCD.

scenario to underestimate the experimental results by about two orders of magnitude (see Fig. 2.2 and Ref. [6]). However, alternative models for the Leading Twist Mechanism have proposed so called humpy DA's, which assume that one of the valence quarks carries most of proton's longitudinal momentum. For a number of reasons this assumption produces very large enhancements to the cross sections, and results in somewhat better agreement with cross section data. The later methodology however has attracted considerable criticism [17] due to its intrinsic self-contradictions (see Ref. [3, pp.5-6] for a good discussion, also Chapter 2.3.1).

With the final analysis of E99-114 data complete, it is now possible to summarize the list of interpretations and conclusions that one can draw from the previous and present results.

Differential Cross Section

As mentioned above, the simplest and the most rigorous approach to the determination of reaction amplitudes in the perturbative framework is the one which is based on the assumption of asymptotic freedom. In this context, as the energy scale reaches a particular (unknown, as far as fundamental theory is concerned) level, the interaction between the quarks occurs at very short distances, where the color force and the interaction between the valence quarks becomes negligible. That allows the quarks in the initial state to be treated as free particles, and the logical implication is that each quark carries almost exactly third of the longitudinal momentum. In other words, the Distribution Amplitudes of the diagram in Fig. 7.7 becomes $\phi(x_1, x_2, x_3) = \phi(x_1 = x_2 = x_3 = 1/3)$. It can also be shown that the perturbative hard component of the total amplitude, T_{hard} (the doted box in Fig. 7.7) varies as

$$T_{hard} \sim \frac{1}{x_1 \cdot x_2 \cdot x_3} \tag{7.6}$$

Since $x_1 + x_2 + x_3 \equiv 1$ it can be shown that the product $x_1 \cdot x_2 \cdot x_3$ reaches its maximum value precisely when $x_1 = x_2 = x_3$, and, correspondingly, this situation corresponds to the lowest possible value for T_{hard}.

It can be inferred from above discourse that *any* deviations from the principle of asymptotic freedom will certainly result in the amplification of the total scattering amplitude. After the major disagreement between the Leading Twist Mechanism observables (when calculated using asymptotic DA's) and data were discovered, it was subsequently proposed to attempt to explain the experimental results through non symmetric DA's, where $x_1 \sim 1$ and $x_2 = x_3 \sim 0$. As can be seen in Fig. 2.2, these $1/x_2 \sim 1/0$ factors have contributed

to major improvements in data-theory comparisons. There, however, are a number of self-inconsistencies in this approach: the expression of $1/x$ for a propagator, which is used in these calculations, can only be used in perturbative framework. However, it has been argued that it it simply wrong to assume that at such small momentums as $x \sim 0$ the perturbative approach is at all valid.

Here we would like to avoid any further comparisons of absolute cross section results with the Leading Twist Mechanism, due to the discussed uncertainties over the applicability of the particular phenomenological models involved, and refer to a much more rigorous and model-independent observable of this mechanism: the proposed s^{-6} scaling of the cross sections.

s^{-6} scaling

The constituent quark counting rule, involving $d\sigma/dt = f(\theta)/s^6$ expression for exclusive processes is based on the assumption of applicability of perturbative QCD (pQCD) and was first derived based on dimensional analysis and on the assumption that in perturbative framework the valence quarks exhibit a dimensional behavior similar to that of a collection of free particles. It was later explicitly derived by G.P. LePage and S.J. Brodsky [29]. Since this rule doesn't involve any specific conjectures involving models for Distribution Amplitudes, it is a very rigorous prediction of the Leading Twist picture, and has previously been extensively used when testing the applicability of pQCD to particular reactions.

In fact, the original Cornell results were understood to support the validity of pQCD specifically because they seemed to point to the much searched for s^{-6} feature in cross section

dependences. However, as the comparison in Fig. 7.6 show, the Leading Twist Mechanism is not the only model which – within experimental uncertainties of the original experimental results – provides such scaling behavior. The results from E99-114 experiments have both lower statistic and systematic uncertainties, and at this point it can be clearly stated that they strongly disagree with the $n = 6$ condition.

Polarization Transfer Asymmetry results

One of the earlier results of E99-114 data analysis involved the measurements of cross section asymmetries due to incoming photon beam polarization flips. The measurement was performed at kinematic point $3E$, at $s = 6.8\ GeV^2$ and $-t = 4.03\ GeV^2$. The measured longitudinal polarization asymmetry is expressed as

$$K_{LL} = \frac{d\sigma(+,\uparrow) - d\sigma(-,\uparrow)}{d\sigma(+,\uparrow) + d\sigma(-,\uparrow)} \tag{7.7}$$

where the first entry in the cross section refers to the photon beam helicity, and the second entry refers to the *recoiled* proton polarization. This ratio measures the transfer of polarization from a polarized photon to an unpolarized proton. It has to be stated that the polarization observable K_{LL} is probably one of the best means to achieve the goals of the experiment, because of the spectacular contrast between the pQCD Leading Twist and Handbag Mechanism predictions. The plots of the theoretical calculations can be seen in Fig. 7.8, indicating to an impressive agreement of the experimental result with the Soft Overlap Handbag prediction. The upper curve, marked as CZ corresponds to the Leading Twist calculation which employed strongly asymmetric DA's. It should be noted that even with model-dependent uncertainties the Leading Twist clearly fails to provide a result which

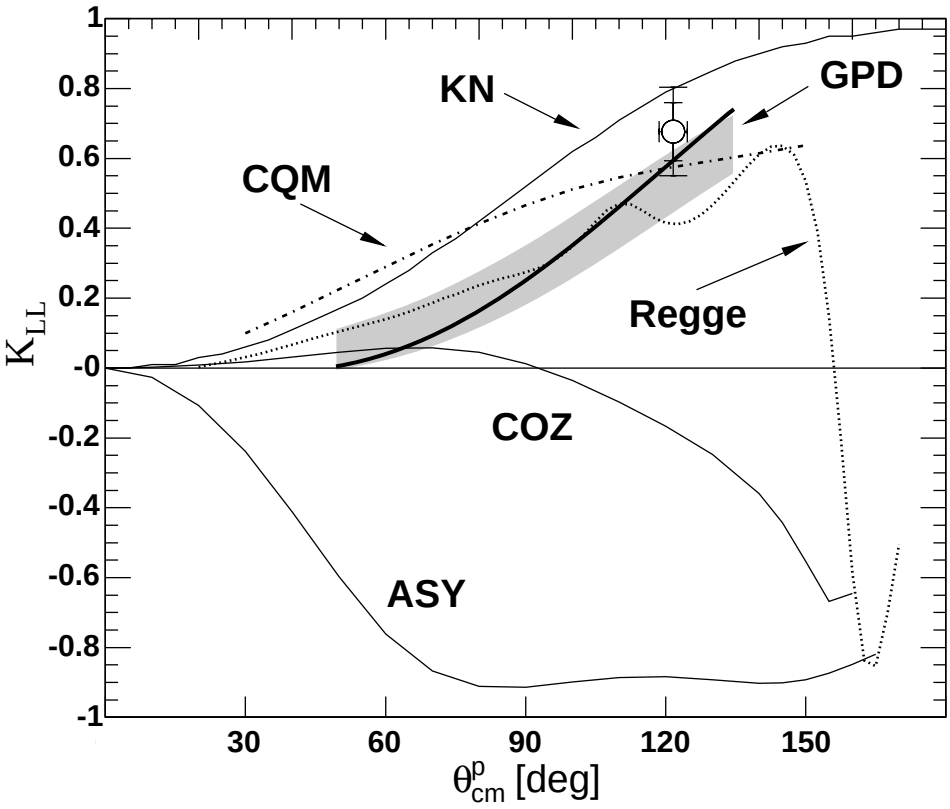

Figure 7.8: Polarization Transfer Asymmetry results for Real Compton Scattering on proton, revealing close agreement of the experimental results (from E99-114 col.) with the Soft Overlap "Handbag" prediction (marked as "GDP"). The experimental result is from Ref. [13]. The curves marked as "COZ" and "ASY" correspond to Leading Twist calculations, based on humped and non-humped DA's, respectively. The curve marked as "KN" corresponds to Compton scattering on a structureless and massless proton.

is comparable with the experimental outcome. This decisive evidence only further confirms what has already been seen both in cross section and asymptotic scaling results: that Leading Twist Mechanism is clearly subdominant for Compton scattering at the momentum and energy transfers characteristic to our experiment.

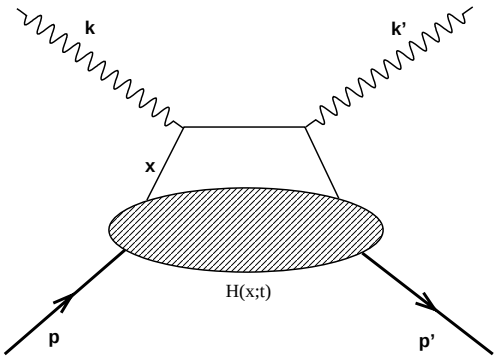

Figure 7.9: Leading order Feynman diagrams for Real Compton Scattering in the framework of Soft Overlap "Handbag" Mechanism.

7.3.2 Soft Overlap Handbag Mechanism

Once the Leading Twist picture has been ruled out, the next task of our analysis is to understand whether the Handbag Mechanism can be considered to be the dominant one at the energy ranges concerned. We would like to start the discussion from the polarized results, since those can be used also to further shed light on the results derived from cross section values.

It is however important to first review the meaning and significance of the Soft Overlap Handbag Mechanism. The primary paradigm of the mechanism involves a single participant quark, with the rest of the proton as a spectator (see Fig. 7.9). Unlike in Leading Twist factorization, the transverse momentum of the quarks is not ignored. Moreover, it plays a major role in the manner in which the initial and final state proton wavefunctions are defined and how the momentum transfered by the photon is absorbed into the transverse momentum distribution of the active quark.

One of the most scientifically curious aspects of the Handbag mechanism is that it is formalized in the framework of Generalized Parton Distributions – hybrid structures which combine in themselves the features of parton distribution functions (PDF) and form factors.

Thus, at $t = 0$ forward direction the GPD's reduce simply into the PDF's, while their first moments in x results in the elastic form factors. A GPD can be seen as a PDF which has been generalized for wide angle exclusive scattering process. The general structure of a GPD is solidified in the following manner:

- Its x-dependence at $t = 0$ is simply modeled based on GRV parameterizations [71], which themselves are based on structure functions derived from DIS data.

- The t-dependence is modeled by assigning the initial and final soft wavefunctions a Gaussian dependence on active quark's transverse momentum (which then can be related to the total four-momentum transfer t), in the following rather intuitive form: $\Psi(x, k_\perp) = \Phi(x)\ exp\{-k_\perp^2/2x(1-x)\lambda^2\}$ where λ is specifically left as a free parameter, and represents our ignorance of the transverse size of the proton in momentum space. This parameter is then varied to produce a best chi-square fit to proton elastic form factor data, to give $\lambda^2 = 0.7\ GeV^2$.

The scientific power of the GPD's is hidden in their process independent feature: given a GPD, one can independently determine a) the DIS structure functions, b) Dirac form factors and of course c) Real and Virtual Compton scattering form factors, as well as the observables for most of other inclusive and exclusive process. To emphasize, since they have been fitted to DIS and elastic data, the GPD's work as some kind of a "triple-bridge" between DIS, elastic electron and Real Compton data. The ultimate question to ask is the following: given a GPD which has been adjusted to DIS PDF's(for its x-dependence) and elastic Dirac form factors (for its t-dependence), will that GPD independently and without *any further*

adjustments reproduce the RCS form factor data, at least to within an order of magnitude? If so, then it is indeed a valid formalism for considering the above mentioned processes and interactions, whether inclusive or exclusive in their description. The results described earlier in Fig. 7.4 and Fig. 7.3 show that this is overall the case and that the Handbag Mechanism does to a larger degree describe the experimental result.

Polarization Transfer Asymmetry, and $R_A(t)/R_V(t)$ ratio

Since the very early stages of the preliminary analysis it was rather clear that the asymmetry, as defined in Eq. 7.7, exhibited a clearly large and positive value. In Fig. 7.8 one can see the comparison between the asymmetry result and the theoretical predictions. A number of conclusions can be drawn:

- The longitudinal asymmetry K_{LL} is large and positive. Within the combination of theoretical, systematic and statistic uncertainties it is clearly favoring the Handbag mechanism. $K_{LL} = 0.677 \pm 0.083 \pm 0.044$.

- The above conclusion allows us to treat the results in the framework of Handbag factorization. According to the Handbag calculations, the polarization transfer asymmetry can be expressed as

$$K_{LL} = K_{LL}^{KN} \cdot \frac{R_A(t)}{R_V(t)}$$

  where K_{LL}^{KN} is the asymmetry for a massless and structureless proton, and can be determined through QED calculations to be $K_{LL}^{KN} = (s^2 - u^2)/(s^2 + u^2)$. R_A and R_V are the axial and vector form factors of Real Compton scattering. This is the only measurement where it is possible to combine polarized and cross section results to

independently determine both $R_A(t)$ and $R_V(t)$. Furthermore, we can use the value of the ratio of the two form factors to derive the vector form factor $R_V(t)$ from other cross section data.

- The proximity of the experimental result to the point particle curve (labeled as KN, for Klein-Nishina, on Fig. 7.8) implies that the two form factors are very close in value: $R_A/R_V = 0.81 \pm 0.15$. It should be understood that the K_{LL}^{KN} curve is the measure of the polarization transfer from the photon to the active quark. On the other hand, K_{LL} is the polarization transfer to the proton *overall*. The process of polarization transfer proceeds in the following simplified succession: the polarization of the incoming photon aligns the quark spin, which then interacts with the proton in the final state and transfers its polarization to the proton. Hence, the ratio of K_{LL}/K_{LL}^{KN} is a measure of correlation between active quark spin and total proton spin. The result shows that the correlation is large: $K_{LL}/K_{LL}^{KN} = 0.81 \pm 0.15$. This implies that the struck quark is very likely to have its spin parallel and in the same direction as the *recoiled* (i.e. final state) proton.

Cross Section and vector form factor $R_V(t)$ Results

The Real Compton scattering differential cross section results have been discussed earlier in this chapter. We would like to only add that the rather good agreement of experimental data with the predictions of Handbag factorization are very encouraging, and the data is arguably favoring Soft Overlap Handbag Mechanism as the dominant one. The next major conclusion is that this validates the earlier conjecture that GPD's, which have been adjusted

to agree to DIS and elastic electron scattering data, can successfully reproduce RCS data without any further modifications.

Another very interesting conclusion which we have been able to reach is that the RCS vector form factor $R_V(t)$, as derived from cross section through the Handbag prescription

$$R_V(t) = \left(\frac{d\sigma}{d\sigma_{KN}}\right)^{1/2} \; [f_V + \alpha(1 - f_V)]^{-1/2}$$

(where $\alpha \equiv R_A/R_V = K_{LL}/K_{LL}^{KN}$ as determined from polarized data at $t = -4.03\ GeV^2$) has shown distinct s-independence, and rather a close agreement with the GPD model.

7.3.3 Overall Conclusions

In the above analysis we come to the following general conclusions:

- Leading Twist Mechanism is clearly subdominant at the energies and momentum transfers of the experiment E99-114, namely: $1.6\ GeV^2 \leq -t \leq 6.5\ GeV^2$ and $4.8\ GeV^2 \leq s \leq 10.9\ GeV^2$.

- There is a large amount of solid scientific evidence which favors the Soft Overlap "Handbag" Factorization as the dominant mechanism. However, it needs to be added that most of the conclusions were reached for points where the Mandelstam variables were constrained to the requirement of being much larger than proton mass squared: $-t, -u > 2.4\ GeV^2$. Furthermore, the data points at largest values of $s = 10.9\ GeV^2$ seem to indicate that the theory is over-predicting the values of cross sections. Also, it should be added that for one group of kinematic points, at $-t = 4.5 GeV^2$ the s-independence of R_V is not observed.

7.4 Future Plans

This thesis has been dedicated to the study of Real Compton Scattering on proton at the energy and momentum transfer range of 1.6 $GeV^2 \leq -t \leq 6.5\ GeV^2$ and 4.8 $GeV^2 \leq s \leq 10.9\ GeV^2$, with the general purpose of understanding the mechanism of proton's interaction with external electromagnetic probes and with the hope of validating(or abolishing) a unified framework for treating a wide variety of electromagnetic processes involving the nucleon. We believe that the experimental work and experimental results described and detailed in this thesis will illuminate further paths towards greater understanding of the nucleonic structure, both in its exclusive and inclusive descriptions, and will lead towards new insights both in experimental and theoretical physics in the search of methodologies to achieve this interesting goal.

We would like to list a number of possible theoretical and experimental efforts which will contribute further towards understanding the complex nature of the nucleon.

7.4.1 Theoretical Improvements for Soft Overlap Mechanism

As already mentioned, the constraint of $-u, -t > 2.4GeV^2$ is needed in most of data-theory comparisons. This, however, severely limits our ability to fully exploit the available experimental data: out of as many as 25 kinematic points only 13 satisfied this requirement and were thus used in the physics analysis. Furthermore, the polarized data, which were used to determine K_{LL} were taken at $-u = 1.\ GeV^2$ which is a very low value, given the above theoretical constraints on the Mandelstam variables. We believe it is of utmost importance

to perform a complete calculations which do not involve any approximations and are not limited by such constraints.

7.4.2 12 GeV upgrade at Jefferson Laboratory

On the experimental front, a 12 GeV upgrade of the Continuous Electron Beam Accelerator Facility (CEBAF) at Jefferson Laboratory has been approved. This may allow for future measurements of Real Compton Scattering on proton at even higher values of $s, -t$ and $-u$. Measurements at higher energy and momentum transfers will contribute to two important circumstances: larger values of $-t$ and $-u$ will permit for an even more rigorous comparisons of data with theory; it will be possible to search for the possible onset of the pQCD scaling behavior and for possible dominance of Leading Twist Factorization at larger values of s and $-t$. If such a transition is indeed observed, then it will be a major and maybe final milestone in the search of the elusive threshold of pQCD's applicability.

7.4.3 RCS-II

Finally, while even one measurement of K_{LL} polarization transfer asymmetry can be and has been very elucidating, the plot of Fig. 7.8 indicate that there are a number of phenomenological models which compete with the Handbag Mechanisms: such as Regge mechanism (where the incoming photon couples to a ρ^0) and Constituent Quark Model [12], which is calculated in the formalism of Light Front Cloudy Bag Model. A new experiment,E03-003 [72] has already been proposed and approved at Jefferson Laboratory, with the purpose of measuring K_{LL} for scattering angles of $\theta_{cm} = 60^o, 100^o, 140^o$ and 160^o. We believe that

these measurements will further strengthen our understanding of Real Compton Scattering and nucleon structure at the medium energies.

Appendix A

Mandelstam variables

The Mandelstam variables are three Lorentz invariant kinematic quantities which can distinctly define the kinematic settings of the reaction. For any two body process, such as the one described in the diagram of Fig. A.1 the Mandelstam variables are defined as

$$s = (p + k)^2 \quad , \quad t = (p' - p)^2 \quad , \quad u = (p' - k)^2 \tag{A.1}$$

where p,k,p' and k' are the four-momentum vectors of the incoming and outgoing particles. The physical significance of s and t is rather clear: s is analogous to the total energy in the system, while t corresponds to the total amount four-momentum which the incoming particle exchanged with its counterpart. It can also be shown that

$$s + t + u = \sum_{i=1}^{i=n} m_i^2 \tag{A.2}$$

where m_i is the rest mass of the reaction participants.

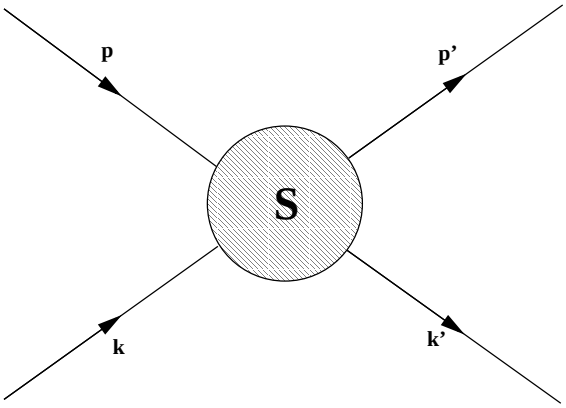

Figure A.1: Scattering diagram, with incoming and outcoming particle four-momentums p,k,p' and k'

References

[1] S. Eidelman et al., Phys. Lett. **B592**, 1 (2004).

[2] G. Miller et al., Physical Review **D5**, 528 (1972).

[3] A.V. Radyushkin, Phys. Rev. **D 58**, 114008 (1998), (hep-ph/9803316).

[4] M. Diehl, Phys. Rept. **388**, 41 (2003), (hep-ph/0307382).

[5] M. Burkardt, Physical Review D **66**, 114005 (2002).

[6] M.A. Shupe *et al*, Phys. Rev. **D 19**, 1921 (1979).

[7] V.L. Chernyak and I.R. Zhitnitsky, Phys. Rept. **112**, 173 (1984).

[8] I.D. King and C.T. Sachrajda, Nucl. Phys. **B 279**, 785 (1987).

[9] V.L. Chernyak, A.A. Ogloblin and I.R. Zhitnitsky, Z. Phys. **C 42**, 569 (1989).

[10] Vahe Mamyan, *Energy Calibration and Reconstruction Algorithms of the RCS Electromagnetic Calorimeter*, Tech. Rep., Thomas Jefferson National Accelerator Facility (2004).

[11] M. Diehl, Th. Feldmann,R. Jakob, and P. Kroll, The European Physical Journal **C39**, 1 (2005), (hep-ph/0408173).

[12] G.A. Miller, Phys. Rev. **C 69**, 052201 (2004), (nucl-th/0402092).

[13] D.J. Hamilton *et. al.*, Physical Review Letters **94** (2005), (nucl-ex/0410001).

[14] M. N. Rosenbluth , Phys. Rev. **79**, 615 (1950).

[15] J. I. Friedman, *Deep Inelastic Scattering: Comparisons with the Quark Model, Nobel Lectures, Physics 1981-1999* (World Scientific Publishing Co., 1993).

[16] S.J. Brodsky and G.R. Farrar, Phys. Rev. **D 11**, 1309 (1975).

[17] N. Isgur and C.H. Llewellyn Smith, Nucl. Phys. **B 317**, 526 (1989).

[18] X. Ji, Phys. Rev. Lett. **78**, 610 (1997), (hep-ph/9604329).

[19] M. Diehl, T. Feldmann, R. Jakob and P. Kroll, Phys. Lett. **B 460**, 204 (1999), (hep-ph/9903268).

[20] M. Diehl, T. Feldmann, R. Jakob and P. Kroll, Eur. Phys. J. **C 8**, 409 (1999), (hep-ph/9811253).

[21] O. Gayou, K. Wijesooriya *et al.*, Physical Review C **64**, 038202 (2001).

[22] O. Gayou *et al*, Phys. Rev. Lett. **88**, 092301 (2002), (nucl-ex/0111010).

[23] O. Gayou *et al*, Phys. Rev. **C 64**, 038202 (2001).

[24] Francis Halzen and Alan D. Martin, *Quarks and Leptons: An Introductory Course in Modern Particle Physics* (John Wiley & Sons, Co., 1984).

[25] K. Goeke, M.V. Polyakov and M. Vanderhaeghen, Prog. Part. Nucl. Phys. **47**, 401 (2001), (hep-ph/0106012).

[26] O. Klein and Y. Nishina, Z. Phys. **52**, 853 (1929).

[27] Michael E. Peskin and Daniel V. Schroeder, *An Introduction to Quantum Field Theory* (Westview Press, 1995), pp. 158-164.

[28] D. Babusci, G. Giordano, A. I. L'vov, G. Matone, and A. M. Nathan, Physical Review C **58**, 1013 (1998), hep-ph/9803347.

[29] G.P. LePage and S.J. Brodsky, Phys. Rev. **D 22**, 2157 (1980).

[30] M. Vanderhaeghen, P.A.M Guichon and J. Van de Wiele, Nucl. Phys. **A 622**, 144c (1997).

[31] V.M. Belyaev and B.L. Ioffe, Sov. Phys. JETP **56**, 493 (1982).

[32] G. Martinelli and C.T. Sachrajda, Physical Letters B **217**, 319 (1989).

[33] J.Bolz and P. Kroll, Z. Phys. A **356**, 327 (1996).

[34] H.W. Huang, P. Kroll and T. Morii, Eur. Phys. J. **C 23**, 301 (2002), (hep-ph/0110208).

[35] R.P. Feynman, *Photon-Hadron Interactions* (Benjamin Reading, 1972).

[36] S.J. Brodsky, T. Huang, and G.P. Lepage, *Proceedings of the Banff Summer Institute, 1981* (1983).

[37] C. Hyde-Wright, A.M. Nathan and B. Wojtsekhowski, JLab Proposal **E99-114**.

[38] C.W Leemann, D.R. Doughlas and G.A. Krafft, Ann.Rev. Nucl. Part. Sci. **51**, 413 (2001).

[39] J. Alcorn *et al.*, Nucl. Instrum. Meth. **A 522**, 294 (2004).

[40] *The Hall A Cryotarget System Website*, URL - http://hallaweb.jlab.org/equipment/targets/cryotargets/HallA_tgt.html.

[41] J. Matthews and R. O. Owens, Nuclear Instruments and Methods **111**, 157 (1973).

[42] K.G. Fissum *et al.*, Nuclear Instruments & Methods **A 474**, 108 (2001).

[43] Vahe Mamyan (Yerevan Physics Institute), *Private communications*.

[44] M. Roedelbronn, *Determination of $B \cdot dl$ dependence for RCS deflection magnet*, Tech. Rep., University of Illinois (2004).

[45] L. Bimbot *et al.*, Nucl. Instrum. Meth. (in preparation) **available at**, http://hallaweb.jlab.org/equipment/detectors.fpp.html.

[46] B.D. Milbrath *et al*, Phys. Rev. Lett. **80**, 452 (1998), (nucl-ex/9712006).

[47] T. Pospischil *et al*, Nucl. Instrum. Meth. **A 483**, 726 (2002).

[48] T.N. Taddeucci *et al*, Nucl. Instrum. Meth. **A 241**, 448 (1985).

[49] E. Brash, M.K. Jones, C.F. Perdrisat and V. Punjabi, JLab Proposal **E99-007**.

[50] G. Heyes *et al.* (1994), Computing in High-Energy Physics (CHEP 94), San Francisco, CA.

[51] E. Offermann, *ESPACE Users Guide*, Tech. Rep., Jefferson Laboratory (1997).

[52] *ABSOFT fortran user guide*, http://www.absoft.com/literature/inteluserguide.pdf.

[53] *Cern program library*, http://wwwasd.web.cern.ch/wwwasd/cernlib/.

[54] N. Liyanage, *Optics Calibration for the Hall A High Resolution Spectrometers using the new optimizer*, Tech. Rep., Jefferson Laboratory (2002).

[55] A. Ketikyan *et al.*, *E99-114 Study of Hall A Photon Spectrometer*, Tech. Rep., Thomas Jefferson National Accelerator Facility (1999).

[56] F. James, Computer Physics Communications **79**, 111 (1994).

[57] O. Blunk and S. Leisegang, Z. Physik **128**, 500 (1950).

[58] C. M. Bender and S. Orszag, *Advanced Mathematical Methods for Scientists and Engineers* (Mc Graw Hill, 1978).

[59] D. Meekins, *Bremsstrahlung codes*, Tech. Rep., Jefferson Laboratory (2000).

[60] R. Ent *et al.*, Physical Review C **64**, 054610 (2001).

[61] N. Makins, Ph.D. thesis, Massachusetts Institute of Technology (1994).

[62] K. Makino and M. Berz, Nuclear Instruments and Methods **A 427**, 338 (1999).

[63] L. Pentchev and J. LeRose, *Quadrupole alignment studies in the HRSe*, Tech. Rep. TN 01-052, Jefferson Laboratory.

[64] L. Pentchev, *Spin transport in the HRSe*, Tech. Rep. TN 04-012, Jefferson Laboratory.

[65] J. Arrington, *A-B-SIMC*, Tech. Rep., Jefferson Laboratory (2001).

[66] M. J. M. Jones, *Private communications*.

[67] V.M. Budneev *et al.*, Physics Reports **15C**, 181 (1975).

[68] M.K. Jones *et al*, Phys. Rev. Lett. **84**, 1398 (2000), (nucl-ex/9910005).

[69] B. Wojtsekhowski, *Private communications*.

[70] M. Diehl, T. Feldmann, H.W. Huang and P. Kroll, Phys. Rev. **D 67**, 037502 (2003), (hep-ph/0212138).

[71] M. Gluck, E.Reya, and A. Vogt, Z. Phys. C **67**, 433 (1995).

[72] A.M. Nathan and B. Wojtsekhowski, JLab Proposal **E03-003**.

Author's Biography

Areg Danagoulian was born in the capital of Republic of Armenia (Armenia), Yerevan, on January 25 of 1977. As part of his secondary education he attended the Physics-Mathematics High School, which was a branch of Yerevan State University. After having completed his primary studies in 1993, he immigrated to the USA with his family, where he completed his undergraduate studies at Massachusetts Institute of Technology in 1999, with a major in Physics and a minor in French. As a part of his undergraduate thesis he worked on the BLAST experiment at MIT-Bates Linear Accelerator, under the guidance of Prof. Richard Milner.

In 1999, he began his doctoral studies in the Department of Physics at the University of Illinois at Urbana-Champaign. He performed his thesis work under the advisory of Prof. Alan Nathan, on the Real Compton Scattering experiment at Hall A of Thomas Jefferson National Accelerator Facility. His studies and research were supported by the following NSF grants:NSF PHY 93-10873, NSF PHY 00-72044 and NSF PHY 02-44889.